Passive Elastography : Tomography and Mechanical Characterization of Biological Tissue

Ali Zorgani

N°d'ordre NNT : 205

THESE de DOCTORAT DE L'UNIVERSITE DE LYON

L'Université Claude Bernard Lyon 1

Ecole Doctorale Interdisciplinaire Science-Santé

(EDISS)

Spécialité de doctorat : Physique Appliquée

Discipline : Ingénierie Biologique et Médicale

Passive Elastography:

Tomography and Mechanical Characterization of Biological Tissue

---

Thèse dirigée par : **Stefan Catheline**

Codirigée par : **Rémi Souchon**

Soutenue Publiquement le 25 octobre 2016, par :

Ali Zorgani

Devant le jury composé de :

Mm. Aline	**Bel-Brunon**	***Maitre de conférences***, *INSA de Lyon, LaMCoS – PC - GMC*	***Examinatrice***
Mm. Sabine	**Bensamoun**	***Chargé de Recherche***, *Université de Technologie Compiègne, UMR-7338*	***Examinatrice***
M. Stefan	**Catheline**	***Directeur de Recherche INSERM***, *Université de Lyon 1, LabTAU-U1032*	***Examinateur***
M. Julien	**De-Rosny**	***Directeur de Recherche CNRS,*** *Université de Paris 7, Institut Langevin*	***Rapporteur***
M. Mathias	**Fink**	***Professeur,*** *ESPCI Paris Tech, Institut Langevin*	***Président du Jury***
M. Hervé	**Liebgott**	***Professeur des Universités,*** *Université Claude Bernard, Lyon 1, CREATIS*	***Examinateur***
M. Frédéric	**Patat**	***Professeur des Université – Praticien Hospitalier,*** *Université de Tours – Biophysique et Médecin Nucléaire*	***Examinateur***
M. Philippe	**Roux**	***Directeur de Recherche CNRS,*** *Université de Grenoble – Alpes, ISTerre*	***Rapporteur***
M. Jérémy	**Bercoff**	***PhD,* Vice-Président, Product Management** *Supersonic Imagin, S.A.*	***Membre Invité***

Introduction

The imaging modality developed in this manuscript relies on two major concepts. First, multiple wave imaging allows taking advantage of the presence of two types of waves for one imaging system. In the case of elastography, slow waves (i.e. shear waves) are imaged by the fast waves (i.e. ultrasonic waves or pressure waves). The resolution of ultrasound and the sensitivity for elastic heterogeneities of the shear wave are combined to conduct an elasticity map. The second idea uses the physiological noise naturally present in the human body to avoid the use of active and controlled shear wave source. Thus, this approach is called *passive elastography*, in the sense that no controlled shear wave source is needed. Passive tomography is widely developed in the field of seismology and geophysics where the implementation of controlled source is very difficult. Therefore, passive elastography was first introduced by Thomas Gallot during his thesis at *Institut des Science de la Terre (ISTerre) at Grenoble*. His objective was to use noise correlation methods developed in seismology in order to conduct elasticity measurement in the human body.

A novel inverse problem based on the physics of time reversal and noise correlation technic is presented in the second chapter. This algorithm combines correlation of the field, its gradient, and its time derivative. It is very fast less than one second with Matlab® 2013 on a standard computer. For sake of clarity the mathematical basics of this inverse problem will be tested on a finite difference numerical simulation of the 2-D elastic wave equation.

The feasibility of passive elastography approach using a low frame rate scanner is presented in the third chapter. Three applications have been investigated in the pancreas, the brain and the cornea, using respectively a conventional ultrasound scanner, magnetic resonance imaging (MRI) and optical coherence tomography. Due to the lack of temporal information in the case of low frame rate imaging system, quantitative shear wavelength maps only can be retrieved. But, the local shear wavelength is proportional to the local elasticity. We will show that it measurement allows the detection of elastic heterogeneities in soft tissue.

However, with an ultrafast scanner the temporal information is available in the recorded data. Thus, quantitative measurement of the shear wave speed can be performed. This configuration will be presented in the fourth chapter. First, quantitative shear wave speed map will be

constructed on a calibrated tissue mimicking phantom using a high frame rate ultrasound scanner. Second, passive shear wave tomography will be performed in the liver of a healthy volunteer, using naturally induced shear waves. Last, optical ultrafast camera will be used in tissue mimicking phantom for a proof of concept for surface wave elastography.

Finally, the resolution of passive elastography is presented in the fifth chapter trough an experimental study. The objective of this experiment is the measurement of the resolution of the passive elastography reconstruction compared to the resolution of echography (b-mode) images. Thus, three different ultrasonic frequencies (5 MHz, 9.5 MHz and 10 MHz) have been used to images the same diffuse shear wave field with a frequency content ranging between 50 and 500 Hz. The objective behind this experiment was to find an answer to the question about the resolution limit of elastography techniques: is it limited by the shear wavelength or the ultrasonic wavelength?

Table of Contents

1 Elastography: Toward a Quantitative Palpation 11

1.1 Mechanical Properties of Soft Tissue 12

1.2 Overview of elasticity measurement methods 13

1.2.1 Observation of natural motion of human organs (1982-1983) 14

1.2.2 Sono-Elastography (1987) 15

1.2.3 Strain Imaging Elastography (Static Elastography) (1991) 15

1.2.4 Acoustic Impulse Elastography (Transient Elastography) (1994) . 17

1.2.5 Magnetic Resonance Elastography (MRE) (1995) 19

1.2.6 Transient elastography with radiation pressure (1998 - 2001) 21

1.3 Natural Shear Waves Imaging (Passive Elastography) 23

1.3.1 Cardiac motion and pulse wave imaging (1996 – 2002) 23

1.3.2 Naturally induced shear waves imaging (Physiological noise correlation method) (2007 – 2013) 24

1.4 Conclusion 25

2 Time Reversal and Noise Correlation in Soft Solid: the inverse problem in passive elastography 28

2.1 Time reversal shear wave in soft solids 29

2.2 Noise correlation methods 30

2.3 Passive shear wave elastography: simulation results on a chaotic cavity 31

3 Passive Elastography Using Low Frame Rate Scanners 39

3.1 Magnetic Resonance Imagin: Brain Palpation from Physiological Vibrations Using 40

3.1.1 Abstract 40

3.1.2 Introduction 40

3.1.3 Phantom experiments *41*
3.1.4 Theory *42*
3.1.5 Brain experiments *45*
3.1.6 Discussions *47*
3.1.7 Materials and Methods *48*
3.1.8 Supplement materials *49*
3.2 Optical Coherence Tomography: towards passive elastography on the cornea of anesthetized rat 52
3.2.1 Abstract *52*
3.2.2 Introduction *52*
3.2.3 Shear wave imaging using Spectral-domain Optical Coherence Tomography *53*
3.2.4 Low-frame rate shear wave imaging *55*
3.2.5 Ultrafast active shear wave imaging *55*
3.2.6 Ex-vivo experiments on a tissue-mimicking phantom *56*
3.2.7 In vivo experiments on the eye of an anesthetized rat *57*
3.2.8 Results *57*
3.2.9 Shear wavelength tomography using low-frame rate shear wave imaging *59*
3.2.10 In-vivo experiments on the eye of an anesthetized rat *62*
3.2.11 Discussion *65*
3.2.12 Conclusion *66*
3.3 Conventional Ultrasound Scanner: HIFU Treatment Monitoring With on Porcine Pancreas with Passive Shear Wave Elastography 68
3.4 Abstract 68
3.5 Thermal lesion visualization: sate of the art 68
3.6 Tissue mimicking phantom experiments 69
3.7 HIFU experimental setup 72

3.8 Results and Discussion 75
4 Passive Elastography Using High Frame Rate Scanners 78
4.1 Passive Shear Wave Speed Tomography with an Ultrafast Ultrasound Scanner 79
4.1.1 Tissue Mimicking Phantom Experiment 79
4.1.2 In-vivo Experiment on the Liver of a Healthy Volunteer 83
4.1.3 Discussion 85
4.2 Toward Elastography of Surface Waves with an Optical Ultrafast Camera 88
Surface wave imaging using a single camera: experimental setup 88
4.2.1 Wave speed measurement on a isotropic phantom: feasibility study 90
4.2.2 Wave speed measurement on a transversally isotropic phantom ... 91
4.2.3 Surface wave imaging using a stereo-vision system on a curved surface 92
4.2.4 Discussion 94
5 Beyond the Diffraction Limit: The Super Resolution in Passive Elastography 97
5.1 Introduction 98
5.2 Experimental Setup 99
5.2.1 Tissue-mimicking Phantom 99
5.2.2 Shear Wave Field Generation 100
5.2.3 Ultrafast Imaging of Diffuse Shear Wave Field 100
5.3 Results 102
5.3.1 Shear Wave Speed Map 102
5.3.2 The Resolving Power 103
5.3.3 Resolution Measurement: in optic vs in elastography 104
5.3.4 Quantification of the B-mode images and shear wave speed maps resolution 106
5.4 Discussion 109

5.5 Conclusion 110
6 Résumé Détaillé en Français 114
7 Bibliographic references 118

1 Elastography: Toward a Quantitative Palpation

The elasticity of biological living tissue is an important medical parameter for diagnosis. For example, abnormal hardening of the liver is a sign of cirrhosis, as well as the presence of a nodule in the breast or in the prostate is an indication of an eventual cancer. The palpation is one of the most common practices in tradition medicine. It reveals information about the shear elasticity. Nevertheless, this method remains very qualitative, and it is highly dependent of the physician's knowledge. However, the modern medicine requires a more quantitative and accurate measurement of the elasticity. From a mechanical point of view, the elasticity can be measured through the shear modulus, which is the ratio between tensile stress and the resulting tensile strain. In the case of palpation, the constraint is the strength applied by the fingers, and the strain is the touch feeling. Thus, to help a better medical diagnosis several techniques were developed during the last twenty years. These set of techniques were grouped under an analogic name "Elastography". A journey through time is proposed in this chapter, with a panoramic vision of the methods developed to assist the physicians in their diagnosis. All of them have the same challenges. First, the detection of small nodules to provide the earliest care for cancer treatment, this consists on the improvement of the resolution. Second, identify benign or malignant tumor, by adding a new parameters such as nonlinearity and anisotropy of the tissue. Last, being noninvasive or minimally invasive and provide the most quantitative amusement of the viscoelastic properties.

1.1 Mechanical Properties of Soft Tissue

The soft tissue can be characterized by Lamé constants: λ usually referred as bulk modulus or compressional modulus, and characterizes the fluid response to compression and μ the shear modulus that quantifies the response to shear stresses. In the case of soft tissue $\lambda \gg \mu$ ($\lambda/\mu \approx 10^6$), this is due to the fact that soft tissue are easy to shear but almost incompressible. From the theory of static elasticity, in a homogeneous, isotropic elastic solid, Young's modulus E depends on Lamé constants (Equation (1.1))

$$E = \mu \frac{3\lambda + 2\mu}{\lambda + \mu} = \mu \frac{3 + 2\mu/\lambda}{1 + \mu/\lambda} \cong 3\mu \tag{1.1}$$

Equation (1.1) means that under the previous hypothesis, the measurement of the shear modulus informs on the Young's modulus and so on the elasticity of the biological tissue. Furthermore, in the human body, the values of the shear modulus are highly variable from one organ to another (Emelianov et al., 2004). Thus, the shear modulus becomes very sensitive parameter for shear elasticity quantification.

The question to ask is: how can we measure quantitatively the shear modulus? The answer is in wave physics. Several waves can propagate in the human body, each of theme convey specific information about the propagation medium. From the wave equation solution, two types of mechanical wave can be described. First, the compressional wave mainly used in echography at the ultrasound frequencies in order to obtain an image of the interior structures. The second one are the shear waves, it propagate at much lower frequencies, typically around 10 – 500 Hz. In the case of isotropic elastic medium characterized by Lamé constants and with a given density ρ. The speed of compressional waves C_p and the speed of the shear waves C_s can be expressed as follow:

$$C_p = \sqrt{(\lambda + 2\mu)/\rho} \tag{1.2}$$

$$C_s = \sqrt{\mu/\rho} \tag{1.3}$$

As mentioned before, the Young's modulus is directly linked to the shear modulus by (Eq. 1.1). Thus, by combining the (Eq. 1.1) and (Eq. 1. 3) the Young's modulus E is related to the shear wave speed by the following equation (1.4):

$$E \cong 3\rho C_s^2 \tag{1.4}$$

The majority of the human body is made of water (~ 70 %) and the variation of the density is limited to 5%. If we consider the density as constant, the Young's modulus is exclusively linked to the shear wave speed. Thus, the local stiffness of the tissue can be locally retrieved by locally tracking the shear wave speed. This is the fundamental principal of dynamic elastography.

Note that, the terminology of "Young's modulus" is widely used in the literature. This is due to the fact that the elasticity was always presented by the mechanic community as the Young's modulus. This is only true in the case of bar under a static stress.). Also, by measuring the shear wave speed, only the shear modulus can be estimated. As well, this is true under the hypothesis of: homogeneous, isotropic and linear elastic solid. However, the most accurate and accessible measurement is the shear wave speed and the shear wavelength. Thus, in our studies only the shear wave speed maps and shear wavelength maps will be presented.

1.2 Overview of elasticity measurement methods

Echography has been developed in the 70's as an efficient ultrasound based diagnosis tool. It provides images of human organs in real time, with a frame rate of 25 to 50 frames / seconds. The resulting images are coded in gray scale, and because of the impedance rupture the contour of different organs can be visualized. Thus, echography becomes a major tool for the diagnosis of several pathologies. But, these observations are not always sufficient to distinguish more complex structures as a breast nodule. That is why, in the early 80s radiologist started to extract new information conveyed by ultrasound such as motion of organs.

1.2.1 Observation of natural motion of human organs (1982-1983)

The idea to quantify the amplitude of the natural motion of the organs with was introduced by *R. Julian Dickinson* in 1982. The principal is based on the analysis of ultrasonic signals in order to quantify the amplitude and the frequency of the natural motions of living tissue (Dickinson and Hill, 1982). He suggests that the amplitude of the motion of organs is directly linked to their elasticity. In the same idea but with a different approach, *A. Eisensher* proposed to use controlled monochromatic vibrations instead of natural motion (Eisensher et al., 1983). His method named "Echoseismography" consists of combining the standard echography and an external shaker. He shows that it is possible to qualitatively distinguish soft form stiff tissue (Fig 1.1).

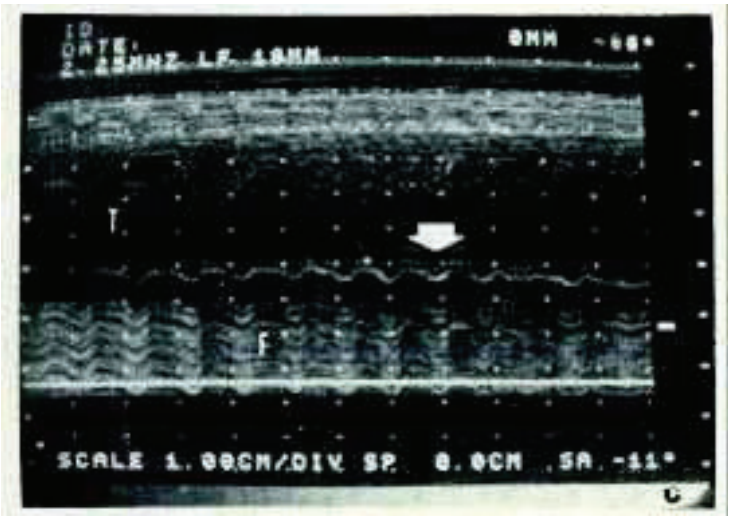

Figure .1.1 Breast Echoseismographe. The white arrow shows the presence of a cancerous nodule . In this single snapshot, the induced vibration can be visible as small fluctuations on the ultrasonic signal. The amplitude of this fluctuation (small for stiff tissue and higher for soft tissue) informs on the elasticity of the visualized organ.(Eisensher et al., 1983)

Figure 1.1 shows the first Echoseismographe in the breast. The induced vibrations are visible on a classical B-mode image, and the white arrow shows a cancerous nodule. Thereby, *A. Eisensher* shows for the very first time that mechanically induced vibrations can be used in order to qualitatively visualize tumors from healthy tissue. Thus, he becomes a pioneer in the dynamic elastography domain that will be presented later.

1.2.2 Sono-Elastography (1987)

Other techniques based on shear wave propagation have been developed in in order to quantify the elasticity of soft tissue. In 1987 *T.A. Krouskop* realized the first elasticity measurement *in-vivo* on an amputee's residual limbs (Krouskop et al., 1987). The displacements induced by the propagation of the shear wave are measured by a Doppler effect with an ultrasonic transducer. Thus, it becomes the first in-vivo experiment of what have been named later by *R. Lerner and K. Parker* as Sono-Elastography (Huang et al., 1992; Lerner et al., 1988; Parker and Lerner, 1992). This approach ignores the propagative aspect of this induced wave (e.g. the speed of the shear waves).

At the same time, *T. Sato's* team start studying the way to measure the speed of monochromatic shear wave (Yamakoshi et al., 1990; Levinson et al., 1995). However, in their simplified approach they ignored the effect of diffraction, dissipation and the stationary waves. Thus, it prevents an accurate measurement of the shear wave speed. As consequence, this simplified model cannot measure quantitatively the shear elasticity of biological tissue. Almost in parallel, the scientific effort was focused on "Strain Imaging Elastography". Unlike the two methods described before, we will see that the strain elastography is based on static stress.

1.2.3 Strain Imaging Elastography (Static Elastography) (1991)

In the early 90s, *J. Ophir* introduced a strain imaging based technique (Ophir et al., 1991). Based on the simplified Hooke's low (Eq. 1.4).

$$\boldsymbol{E = \sigma/\varepsilon} \tag{1.5}$$

Where E is the Young's modulus, σ is the stresses applied by the ultrasonic probe on the tissue and ε is the resulting strain. The strain is measured by a standard speckle tracking technique presented below (cf. section 1.2.3.1). A strain map is retrieved by the comparison of Pre and Post stresses ultrasonic images (Fig. 1.2).

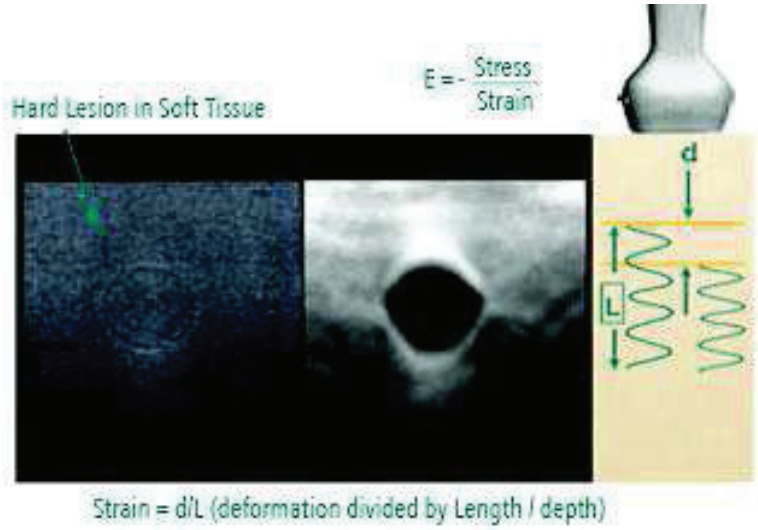

Figure .1.2 Comparison between sonograms (left) and a strain map (right) in a tissue mimicking phantom. Source: medical.siemens.com

The provided indications is only qualitative, on the scale Soft / Stiff. The soft tissue underwent a strong deformation compared to a stiffer tissue. Despite this qualitative aspect, static elastography had a huge success. Two commercial ultrasound scanners incorporate a static elastography mode into their systems. Hitachi® introduced the "eMode" and Siemens® the "eSie" mode. The weakness of this technique was on the quantitative measurement of the applied stresses. As consequence, it was not capable to provide a quantitative measurement of the shear elasticity. It was not until the arrival of transient elastography to provide quantitative measurement of the shear wave speed.

1.2.3.1 Speckle Tracking Algorithm

An ultrasonic impulse propagates in soft solid and meets different heterogeneities. The speckle is formed from the back scattered signal due to the interference of echo. For example, the propagation of a shear wave in an elastic medium induces a displacement of this scatters. The induced displacements are measured by temporal comparison of ultrasonic signal. This method is called, speckle tracking algorithm. It is based on the cross-correlation of the radio frequency (RF) signal for time shift estimation (Ophir et al., 1991). To briefly explain the speckle tracking algorithm an example will be presented here.

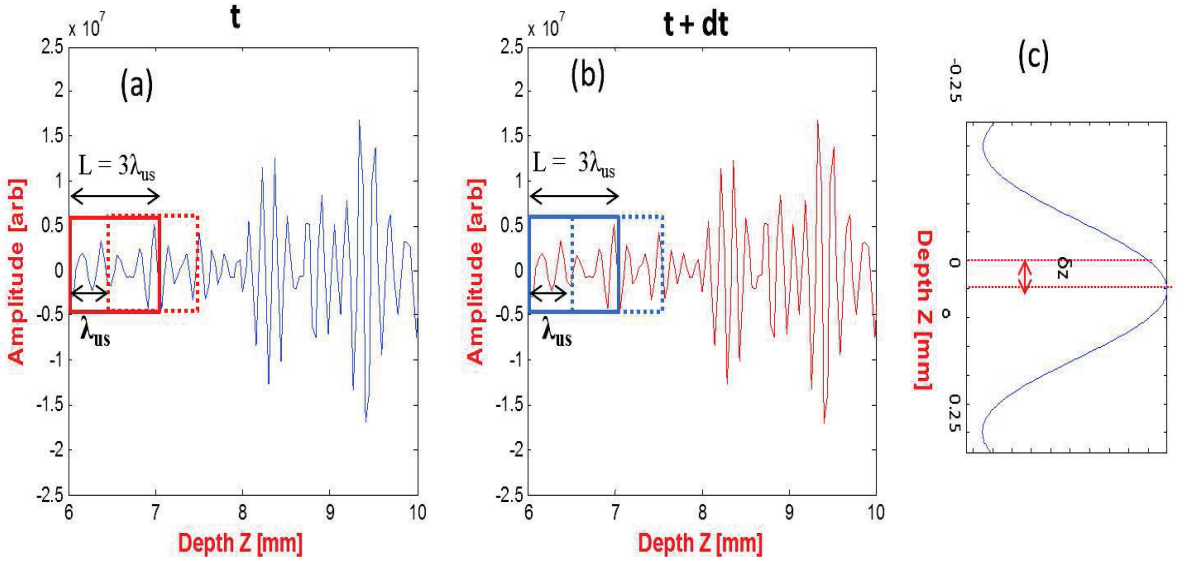

Figure 1.3 An ultrasonic impulse propagates in soft solid and met different heterogeneities. The speckle is formed from the back scattered signal due to the interference of echo. The signal recorded by a single element of the probe is presented at time t0 and t0 +dt (respectively (a) and (b)). The propagation of the shear waves induces a displacement of the speckles. The speckle tracking algorithm consists in dividing the signal in windows equal to three times the ultrasonic wavelength. Then, the position of the maximum of the cross-correlation function between successive signals informs on the induced displacement in this window (c).

The "RF" signal recorded by this single element at time t and t + dt is represented in depth (Fig. 5.4 a and b). The speckle tracking algorithm consists in dividing the RF signal in correlation windows with a typical length of three to four times the ultrasonic wavelength. The maximum of the cross correlation function between the red window in (Fig. 5.4 a) and the blue window in (Fig. 5.4 b) is computed. This maximum (Fig. 5.4 c) represent the displacement δz of the volume associated to the window. The axial displacement along the entire RF signal is computed by shifting the initial window by the size of one ultrasonic wavelength (red and blue dashed windows).

1.2.4 Acoustic Impulse Elastography (Transient Elastography) (1994)

During his PhD thesis started in 1994 under the supervision of *Mathias Fink*, *Stefan Catheline* introduced one dimensional transient elastography (Catheline, 1998). The idea is fundamentally different compered to static or sono-elastography elastography. Henceforth, the shear waves are generated by an impulse with an external mechanical vibrator. The experimental setup used in his study is presented in (Fig. 1.4 a). The mechanical vibrator hits the surface of the phantom and

creates a 5 µs low frequency (100 Hz) transient elastic wave. A focused transduced (3 MHz) is placed in front of the vibrator to record the back scattered signal at a sampling rate of 1300 Hz. Thanks to an ultrafast sampling rate, the shear waves are measured in real time along the ultrasonic beam.

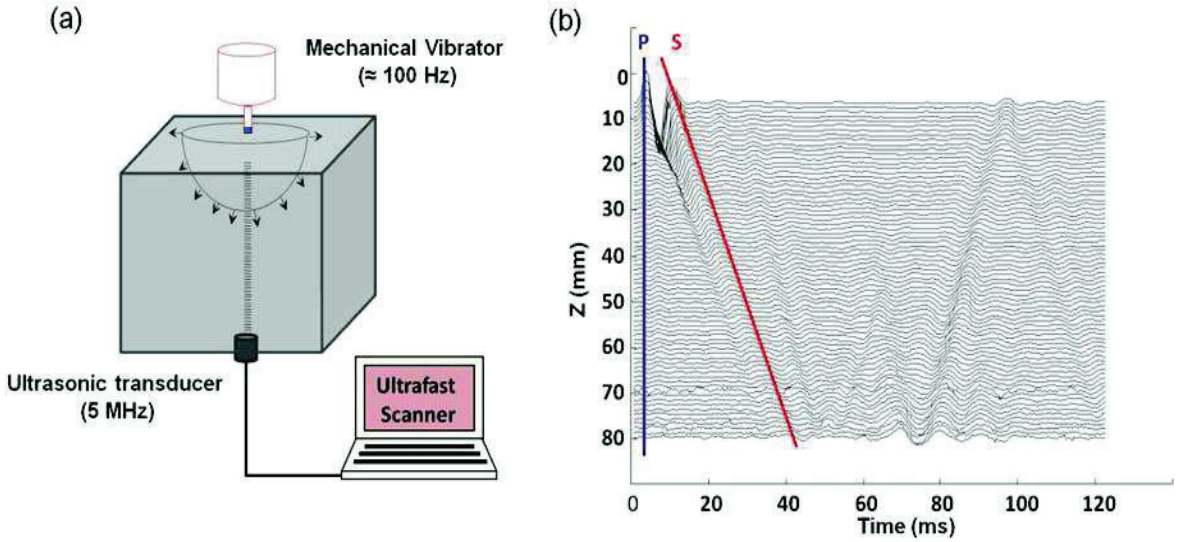

Figure 1.4. (a) Experimental setup used in 1D transient elastography. In an agar-gelatin phantom, an external mechanical vibrator creates a shear wave at a frequency of 100 Hz. The propagation is imaged by a single transducer at a rate of 1300 Hz. (b) a seismogram showing the z component of the displacement field. Two types of waves can be observed: P for pressure wave that propagate almost instantaneously. S is the shear wave where the speed can be measured from the red slope (Catheline, 1998).

The induced displacement field is computed by a speckle tracking technical (Catheline, 1998). Transient elastography allows the separation of the compressional wave form the shear wave (Fig. 1.4 b), without being influenced by the boundaries conditions. This work opens a new way to perform reliable quantitative elastography measurements.

The setup has been slightly modified. The pulsed low frequency mechanical vibration is now given by the ultrasonic transducer (Sandrin et al., 2002). This work found a clinical application through a new ultrasound tool named Fibroscan® developed by the company Echosens®. The Fibroscan® provides 1D elasticity measurement along the ultrasonic beam. The mean application of this scanner is the classification of the fibrotic stages of the liver.

The development of transient elastography shows a strong need to an ultrafast imaging system. Indeed, a high frame rate imaging systems is needed to sample properly wave's propagation in time. Motivated by this need, the first ultrafast ultrasound scanner was developed (Sandrin et al., 1999).

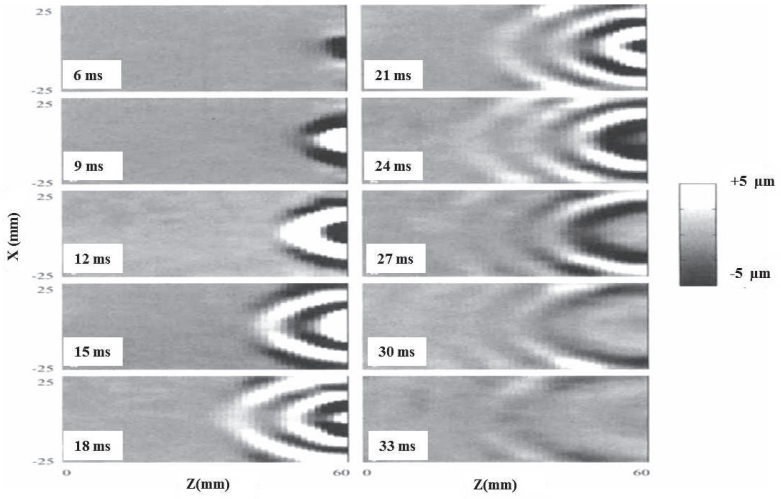

Figure 1.5. Snapshot of a displacement movie showing a wave front propagate from a point-like source sampled at a sampling rate of 1000 frames/second.

In figure 10, the axial displacements induced in the homogeneous phantoms after an low frequency excitation of central frequency 200 Hz and duration 3 periods has been sent to the vibrator are shown. These displacements images are represented every 3 ms. The speed of the 200 Hz transient shear wave is estimated of about 2 *m/s.* The displacement amplitude attenuates as the wave goes deeper and deeper. The wavelength λ = c/f, and the shear modulus are respectively about 1 cm and 4,000 Pa. This imaging system offers the opportunity from the development of the transient elastography, and 2D mapping of the shear wave speed in soft tissue (cf. section 1.2.6).

1.2.5 Magnetic Resonance Elastography (MRE) (1995)

Magnetic Resonance Elastography have been introduced by *J. Greenleaf's* team. The principal is the same as in sono-elastography, which is the measurement of the speed of a monochromatic shear wave from successive snapshots (Muthupillai et al., 1995). The monochromatic shear waves are induced by an external vibrator (Fig .1.6.a). The resulting displacements (Fig .1.6.b)

are measured from the phase variation the MRI signal. Then, a local shear modulus is estimated from the measurement of the shear wavelength (Fig .1.6.c).

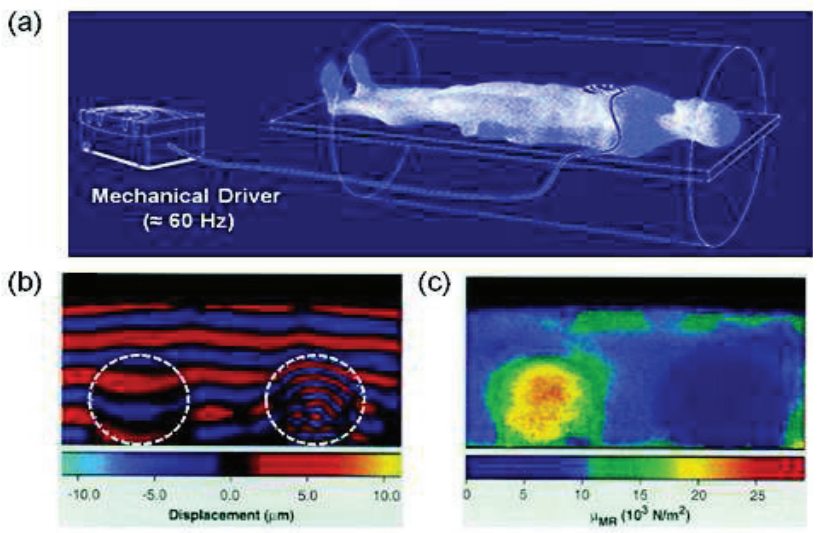

Figure .1.6 (a) MRE experimental setup. Monochromatic shear wave are mechanically generated by an external source with a frequency ranging from 50 to 1000Hz. (b) The measured displacement inside a phantom with a soft and a stiff inclusion. (c) Quantitative shear modulus computed from the locale shear wavelength of the displacement images (Muthupillai et al., 1995).

This method faced two major obstacles. First, the frame rate is very low, about one frame / second, that makes the acquisition very long, about ten minute. But the displacement still can be measured with a stroboscopic MRE sequence, where the scanner is synchronized with the external vibrator. Second, the cost of MRI scanner is very high and not affordable by much of laboratory, which slows down its development compared to ultrasound based methods.

However, the advantage of MRE is its ability to measure the tree components of the displacement field, where the ultrasonic method measure only the displacement on the direction of the ultrasonic. Thus, MRE gives possibilities to measure the anisotropy and the viscosity of biological tissue (Sinkus et al., 2005). In addition to that, with MRI scanner we are capable to image the interior of the brain, which is not the case with ultrasound scanner, because of the attenuation of the ultrasonic beam. This is a non-negligible advantage of MRE.

1.2.6 Transient elastography with radiation pressure (1998 - 2001)

Radiation pressure was used for the first time for elastography applications by *T. Sugimoto* in 1990 (Sugimoto et al., 1990). In his experiment, a localized deformation of the tissue is induced by the radiation force of a focused ultrasonic beam. His technique was based on the qualitative observation of the amplitude of the induced deformation: High amplitude in soft tissue and low amplitude in stiff tissue. Similar to strain imaging technique, it was not possible to provide a qualitative measurement of the local elasticity. But, the idea to use the radiation pressure was quite innovative.

In 1998, *A. P Sarvazyan* used the radiation pressure in order to generate a transient shear wave **(Sarvazyan et al., 1998a)**. The induced shear waves were imaged by an. Figure 1.7 shows the distribution of the shear displacement in the longitudinal plane of the phantom at two different times. These images are displayed over an area 220 mm x 220 mm with the phantom positioned in the center, and the arrows indicate the location of the shear wave front. In these gray-scale images, full black represents no displacement, and full white represents the maximum motion along the ultrasound beam direction, i.e., shear displacement. Clearly, in the first image (Fig. 1.7 a), the shear displacement is localized in the center of the phantom. The shear displacement distribution at a later time (4 ms compared to the image in Fig. 1.7 a) is shown in Fig.1.7 b. In this image, the shear wave already has propagated some distance away from the focal zone and appears as two symmetric bands on either side of the focal zone. Unfortunately, this technique did not get a success in clinical application because of the complexity of the experimental.

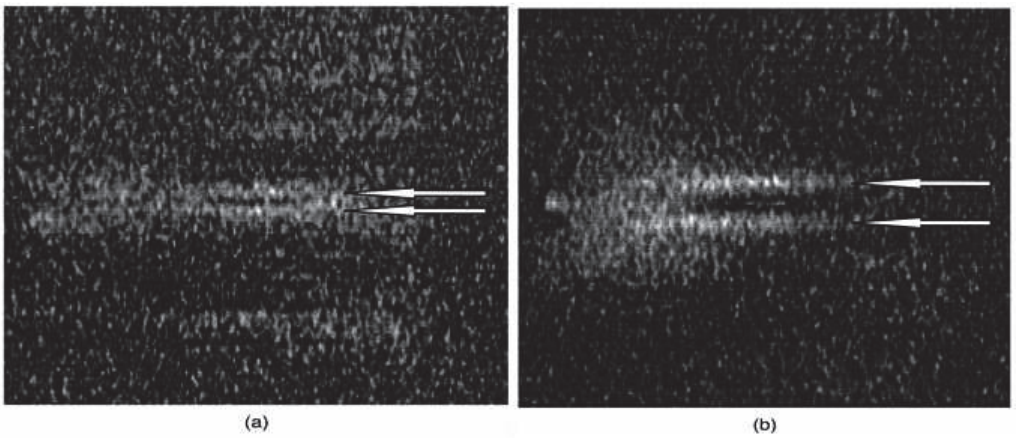

Figure 1.7. Spatial distribution of the axial shear displacement obtained at different instances: (a) 4.4 ms and (b) 8.4 ms. Arrows indicate the position of the shear wave front (Sarvazyan et al., 1998a).

Quite similar to Sugimoto's experiment, another application of the radiation pressure was proposed by in 2001 by *K. Nightingale*. Called Acoustic Radiation Force Impulse (ARFI), this approach was based on the measurement of the tissue response to the radiation force. In this method, focused ultrasound is used to apply localized radiation force to small volumes of tissue (2 mm^3) for short durations (less than 1 msec) and the resulting tissue displacements are mapped using ultrasonic correlation based methods. The tissue displacements are inversely proportional to the stiffness of the tissue, and thus a stiffer region of tissue exhibits smaller displacements than a more compliant region. Due to the short duration of the force application, this method provides information about the mechanical impulse response of the tissue, which reflects variations in tissue viscoelastic characteristics (Nightingale et al., 2002a). A qualitative elasticity map is retrieved by steering the focal spot to cover the entire medium. This method does not provide a qualitative measurement of the shear modulus. Therefore, it remains only a qualitative technique to estimate the tissue elasticity.

The most successful clinical application of radiation pressure was developed by *J. Bercoff* in 2004 at Institut Langevin (Bercoff et al., 2004a). Super Shear Imaging (SSI) technique uses an ultrasonic array to genet the shear waves by radiation pressure. Thanks to an ultrafast scanner, the propagation of the shear waves is tracked while propagating away from the source, in the direction perpendicular to the ultrasonic beam. The main problem is the rapid attenuation with distance of a single radiation shear wave. Thus, in order to increase the area to be crossed by the shear waves, a cylindrical shear wave is generated by focusing the ultrasonic beam at different focal depths. This is achieved by changing the electronic delays between the transmitted signals of each transducer element. The procedure is illustrated in Figure 1.8(a). If the shear wave source moves faster than the radiated shear waves, constructive interference along a Mach cone will result in a high-displacement cylindrical shear wave that propagates over relatively long distances. The shear wave speed is relative to the local shear elasticity. Thus, by measuring the time of flight of the induced shear wave, a quantitative 2D elasticity map can be retrieved in real time. Figure 1.8 b shows a stiff inclusion in a soft agar-gelatin phantom. This method gives birth to a scanner called "Aixplorer®" from the company Supersoni Imagin. Inc. Since 2009 it is the first scanner that provides 2D elasticity map in real time.

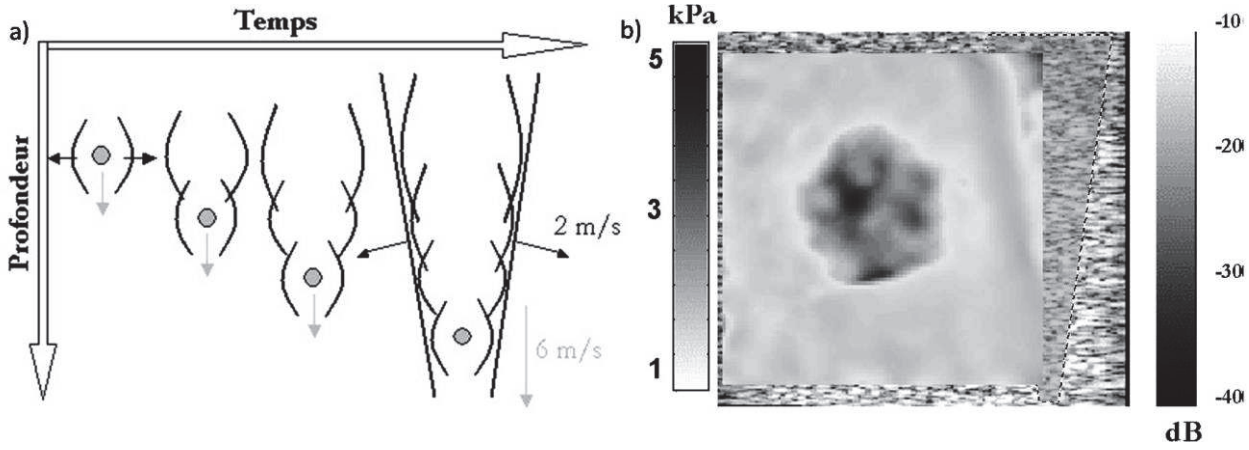

Figure 1.8. (a) Generation of a Mach cone by focusing the ultrasonic beam at different depth. (b) Quantitative elasticity map on an agar-gelatin phantom contain a stiff inclusion. (Bercoff et al., 2004a).

All the techniques introduced until now are called "active" in the sense that a controlled shear wave source is need. However, there is another way to perform dynamic elastography without the need to control the source. Indeed, shear waves are naturally present in the human body. The heart beating, the muscles activities and the blood pulsatile flow are all uncontrolled shear wave sources, that we commonly call "Physiological Noise". This new category of elastography techniques are grouped under the term of "Passive Elastography".

1.3 Natural Shear Waves Imaging (Passive Elastography)

1.3.1 Cardiac motion and pulse wave imaging (1996 – 2002)

After *R. Julian Dickinson*, one of the pioneering works in this approach was done by *H. Kanai* in 1996. The method consists in measuring the natural vibration of the heart wall. In his experiment, the imaging system (i.e. a standard ultrasound scanner) was synchronized with the cardiac cycle. The measured amplitude was less than 100 μm with a frequency up to 100 Hz. The thickness of the heart wall was directly related to the amplitude of vibration (Kanai et al., 1996). The obtained thickness change was related to contractility of the myocardium and helps to diagnostic the ischemia and infraction. This method was not capable to retrieve the shear modulus, but opens a new way to use the natural vibration in order to diagnosis heart disease.

E. Konofagou used in 2002 the myocardial motion as a passive stress in order to measure the local deformation of the heart wall (Konofagou et al., 2002). Only a strain map was given in this study. As we have shown before, this static method is only qualitative.

1.3.2 **Naturally induced shear waves imaging** (Physiological noise correlation method) (2007 – 2013)

The pioneering work in this field was done by *Sabra et al.* in 2007 (Sabra et al., 2007). In his work he measured *in vivo* the global visco-elastic properties of skeletal muscle by using the noise naturally present in such tissue. For the experiment, sixteen miniature accelerometers were skin mounted along the vastus lateralis muscle providing the surface displacement field (Fig. 1.9 top). By applying correlation techniques to the recorded displacement field, the shear wave dispersion curve was extracted (Fig 1.9 bottom). Finally by fitting a Voigt model the tissue's global viscosity and elasticity were retrieved.

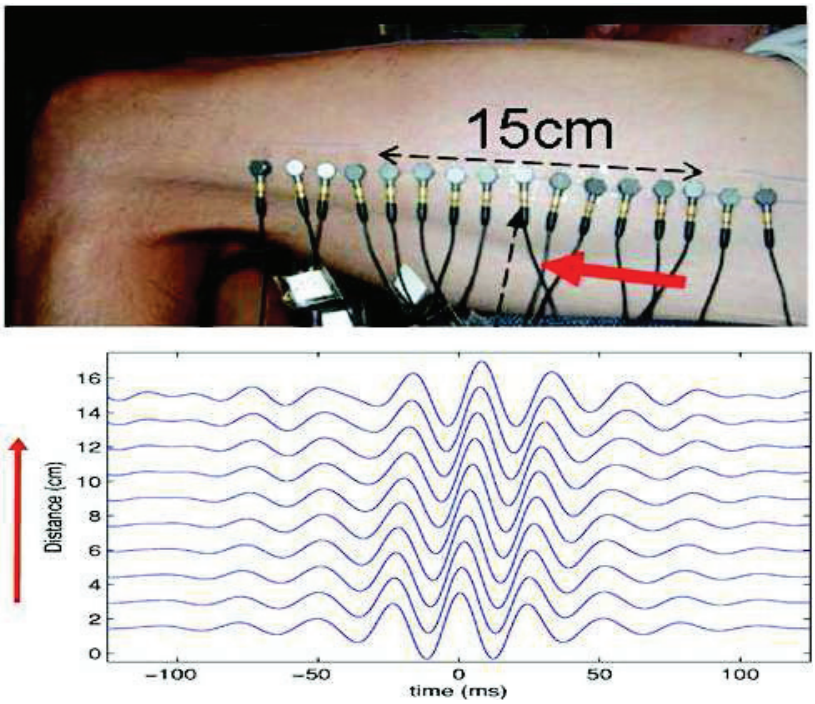

Figure 1.9. (Top) Experimental setup, sixteen accelerometers skin mounted along a healthy volunteer's leg. (bottom) Coherent propagating shear wave profile extracted from stacked cross correlations of muscle noise (Sabra et al., 2007).

Inspired by seismic noise correlation methods, *T. Gallot* shows during his thesis in 2011 the possibility to construct shear wave speed maps from naturally induced shear waves in the human body. In his experiment, he used an ultrafast ultrasound scanner to measure the natural

displacement inside a liver of healthy volunteer (Gallot et al., 2011). The inverse problem is based on the Green's function retrieval from the cross-correlation of a broad band noise-like shear wave field. In the sonogram data (Fig. 10 a), two zones were visible. Above z = 12 mm, the bright region corresponded to the abdominal muscles; the dark region was the liver. Good correspondence was seen with the shear-wave-speed tomography (Fig. 10 b), where the interface between these two regions was seen around z = 12 mm. whereas other elastography techniques suffer from the physiological noise in the human body, this method takes advantage of the permanent elastic field.

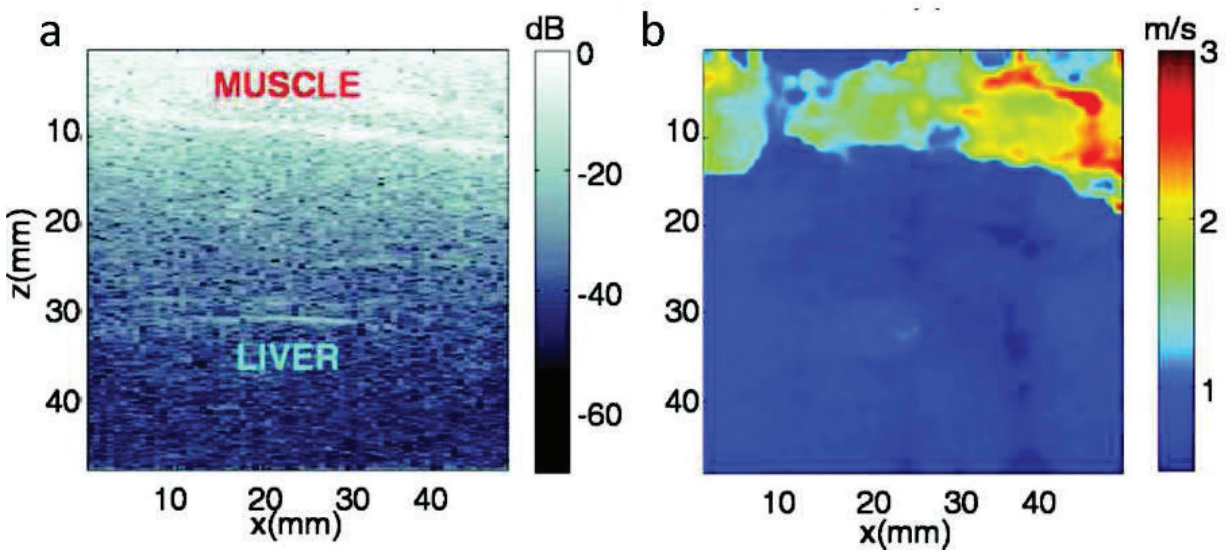

Figure 1.10. (d) B-mode image of the liver region. (e) Passive shear wave speed tomography from the correlation of physiological noise (Gallot et al., 2011).

1.4 Conclusion

This non exhaustive review shows that Elastography is in a continuous development. First, in static elastography a strain image is obtained. However due to the lack of information about the applied stress and boundaries conditions, this technique provides only qualitative elasticity estimation. To overcome this limitation, different technique based on the measurement of the speed of monochromatic shear waves were developed such as sono-elastography and magnetic resonance elastography (MRE). But, it still suffers from a bias in the measurement of the shear wave speed due to the stationary waves and the boundaries conditions.

Then, Transient Elastography made its apparition. Henceforth, the shear waves are generated by an external pulse (external vibrator or radiation pressure). This techniques are instantaneous, not effected by the boundaries conditions and allows the real time measurement of shear wave propagation thanks to ultrafast imaging scanners. This opens a wide range of clinical applications.

Finally, Passive Elastography shows its capability to retrieve elastic parameters for uncontrolled shear wave field. This offers solutions to different problems faced by the others methods. This thesis is in the continuity of the work realized by *Thomas Gallot* during his thesis. We propose a novel algorithm based on the physics of time reversal. Its feasibility was tasted in different applications. First, shear wave speed tomography using an ultrafast ultrasound scanner, in a calibrated phantom and in-vivo has been realized. Second, the feasibility to monitor High Intensity Focused Ultrasound (HIFU) treatment with a commercially available scanner was tested. In the case of a low frame rate imaging system, only a shear wavelength tomography can be retrieved. Third, a new approach to perfume Magnetic Resonance Elastography (MRE) without the need to the wave source to the scanner is presented in both a calibrated phantom and a brain of healthy volunteer. Finally, for ophthalmic application, an Optical Coherence Elastography (OCE) based on the measurement natural motion of the cornea is tested. The last part will be dedicated to the evaluation of the resolution. We will show that the resolution of passive elastography is not limited by the shear wavelength, but it is on the same order of magnitude as the ultrasonic wavelength.

2 Time Reversal and Noise Correlation in Soft Solid: the inverse problem in passive elastography

Time reversal is a technique that focuses waves onto a source location by emitting a time-reversed version of the recorded wave field. The focusing property is due to the reciprocity in space and the reversibility in time for the wave field. To perform such experiment a time reversal mirror with several emitters/receivers channels is need. However, in a chaotic cavity, the reverberation allows to retrieve the same focusing properties with one channel. The interest of reverberation is identical for a passive configuration of noise correlation experiment. Thus, in this chapter is dedicated to demonstrate the close link between time reversal technique and noise correlation through a numerical simulation.

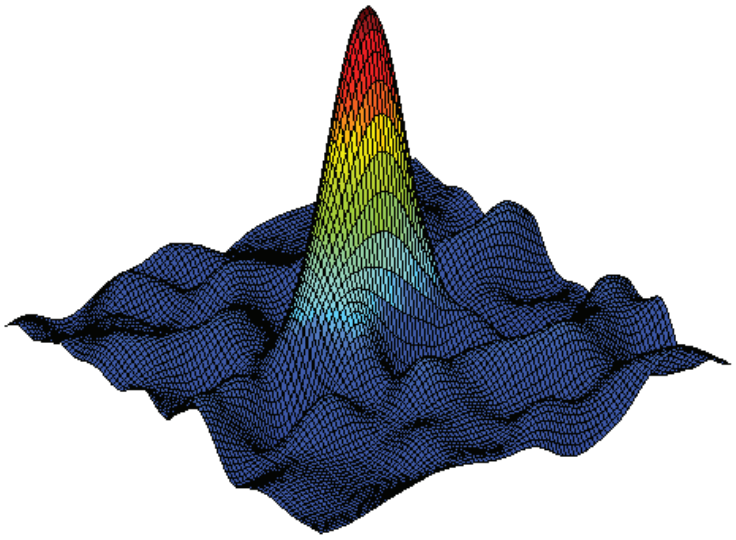

2.1 Time reversal shear wave in soft solids

Time reversal is a well known adaptive focusing technique for the correction of aberrations induced in heterogeneous and complex media (Fink, 1997). This method is based on two steps. Firstly, a point source ”a” is embedded in the medium and transmits a short ultrasound pulse that propagates through the aberrating medium to a set of transducers S_i (Fig 1.2 left). The signal received by the transducers is digitized and stored in memory. Secondly, the received signals are time reversed and sent back from the transducers to the medium (Fig 1.2 right). Due to the time-reversal invariance of the wave equation, the wave generated by the transducers propagates in the medium as if time was going backwards. As a consequence, the ultrasonic wave refocuses at the initial source location inside the medium. This method has been extensively investigated in various application areas such as, as medical imaging and therapeutic applications (Thomas et al., 1996), telecommunication (Kuperman et al., 1998; Lerosey et al., 2007), nondestructive testing (Ulrich et al., 2007) and interactivity (Ing et al., 2005). This is an elegant and robust adaptive focusing method, but it requires a point source to be placed inside the medium. Based on the same principle, it is also possible to use backscattered echoes from a strong scatterer inside the medium as an ultrasound source. This approach shows potential for kidney stone tracking and destruction in lithotripsy (Thomas et al., 1996).

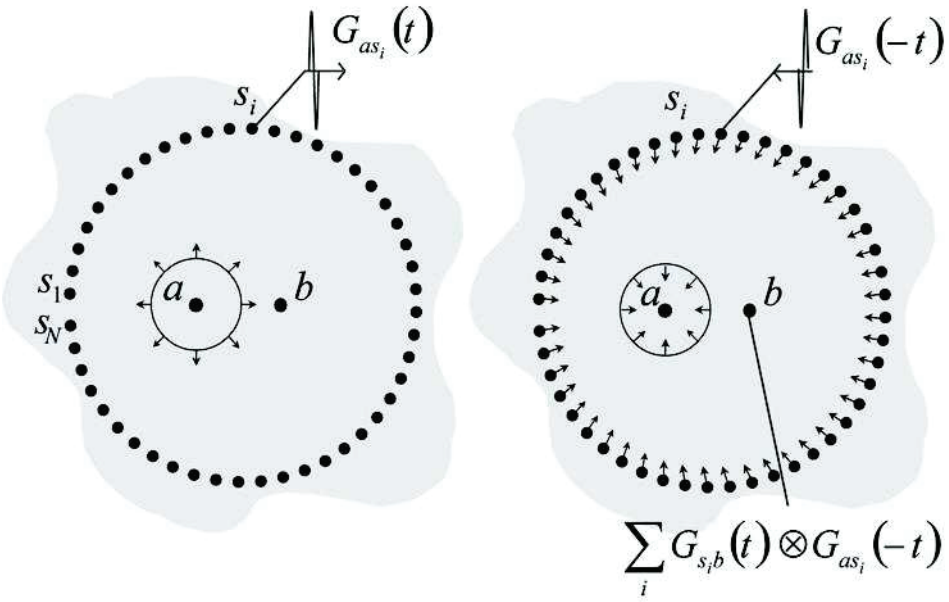

Figure 2.1. A perfect time reversal cavity, formed by a set of transmitters / receivers surrounding an impulse source. The recorded signal, is time reversed and re-emitted will refocus at the source position. Source (Gallot, 2010).

In practical situation it is difficult to include a source inside a medium. This problem is known in the medical field as the “ultrasonic artificial stars” (Pernot et al., 2006) in reference to analogous laser guided artificial stars used for optics adaptive focusing in astronomy (Thompson and Gardner, 1987). Different techniques using backscattered random noise have been developed to correct the aberrations (Nock et al., 1989). However, the statistical estimation of the time delays compensation is noisy and often not good enough to achieve aberration corrections.

Nevertheless, this perfect time reversal mirror can be replaced by a reverberant solid (reflecting boundary conditions). Thus the waves are not recorded at the boundaries of the cavity but reflected in the media to continue the propagation. If the cavity is chaotic, then the wave fronts will travel across all the media. In this case only one transmitter / receiver is needed to acquire all the record the reverberated wave field. It is the so-called one channel time reversal mirror (Draeger and Fink, 1997).

The first one channel time reversal experiment on a soft solid has been realized by Catheline et al. (Catheline et al., 2008). The great advantage of such configuration is that a perfect time-reversal cavity can be approached experimentally using a point source mounted on a vibrator: it is the so-called one channel time reversal mirror. The elastic field in volume was measured noninvasively from the solid surface using a single transducer and ultrasonic techniques developed in the field of transient elastography (Catheline et al., 1999). In this medical field, propagation media are soft solids such as soft tissues, muscles, organs, or mimicking tissue phantoms. The low frequency shear waves (a few hundred hertz) propagate at a speed of a few meters per second, which results in centimeter size wavelength. Consequently, the original aspects of these time-reversal elastography experiments are (1) no ‘‘artificial stars’’ are needed, (2) the time-reversal collapse is directly observed inside a solid, and (3) for centimeter wavelength, near field-like effects are clearly apparent.

2.2 Noise correlation methods

When the backpropagation step is not possible (e.g. seismology), the time reversal experiment cannot be realized. Instead, noise correlation based methods relieves the whole approach. Thus, the chaotic cavity is replaced by a multiple scattering media (Derode et al., 2003a; Paul et al., 2005). Under some conditions (i.e. wide frequency band and diffuse wave field) the correlation of signals recorded at point “a” and “b” converge to the Green’s functions between “a” and “b” (Gouédard et al., 2008; Larose et al., 2006). The noise correlation technique is used in order to

extract information from a complex wave field without any active source. This method is called passive in the sense that only a diffuse wave field observation is needed.

Passive imaging techniques based on noise correlation have been developed in several fields such as helioseismology (Duvall Jr et al., 1993; Giles et al., 1997), oceanography (Buckingham et al., 1992; Roux et al., 2004) and ultrasonics (Weaver and Lobkis, 2002). Geophysics and mantle crust tomography remain the most important applications of noise correlation (Campillo and Paul, 2003; Shapiro et al., 2005). The correlation of noise-like signal allows the extraction of information from a broad band and multiply scattered signal. This consists in retrieving a wave velocity maps from permanent ambient seismic noise. Similar to seismic ambient noise, the heart beating and the muscular activities create a permanent physiological noise in the human body. Through correlation, the physiological noise can be used to extract mechanical proprieties of biological tissue. The ability of noise correlation technique to passively retrieve the elastic parameter in-vivo have been shown (Sabra et al., 2007; Gallot et al., 2011).

With our approach that combines correlation of the field, its gradient, and its time derivative, a tomography reconstruction is obtained even though measurements are well below the Shannon-Nyquist limit (Catheline et al., 2013). From a wave physics point of view, we explored configurations for which each realization of time and space field measurement is independent. In other words the spatio-temporal coherence of the field is a delta function. Practically speaking, tomography reconstruction in this situation allows using slow imaging devices working at rate independent to any characteristic time period of the noise field. This general approach valid for any wave nature is demonstrated in the specific field of shear wave imaging or elastography. The present technique thus offers the advantage to be compatible both with recent ultrafast ultrasonic scanners and slower conventional ultrasonic scanners commercially available.

For sake of clarity the mathematical basics of our inverse problem will be tested on a finite difference numerical simulation of the 2-D elastic wave equation. Two cases are studied, first the over sampled (below Shannon's sampling frequency) wave field, where a passive shear wave velocity can be conducted. Second, the under sampled (under Shannon's sampling frequency) wave field, in this case only wavelength tomography can be conducted.

2.3 Passive shear wave elastography: simulation results on a chaotic cavity

We consider a 400 by 400 grid meshes solid cavity (80 by 80 cm), where one segment cut-off is surrounded by a vacuum. The shear wave speed in the solid was set at 3 m/s (Fig 2.2 a). In order

to test the algorithm to extract local elasticity information, three circular inclusions were introduced within the solid cavity, whit different shear wave speed: 6 m/s, 5.2 m/s and 4.3 m/s (Fig 2.2 a).

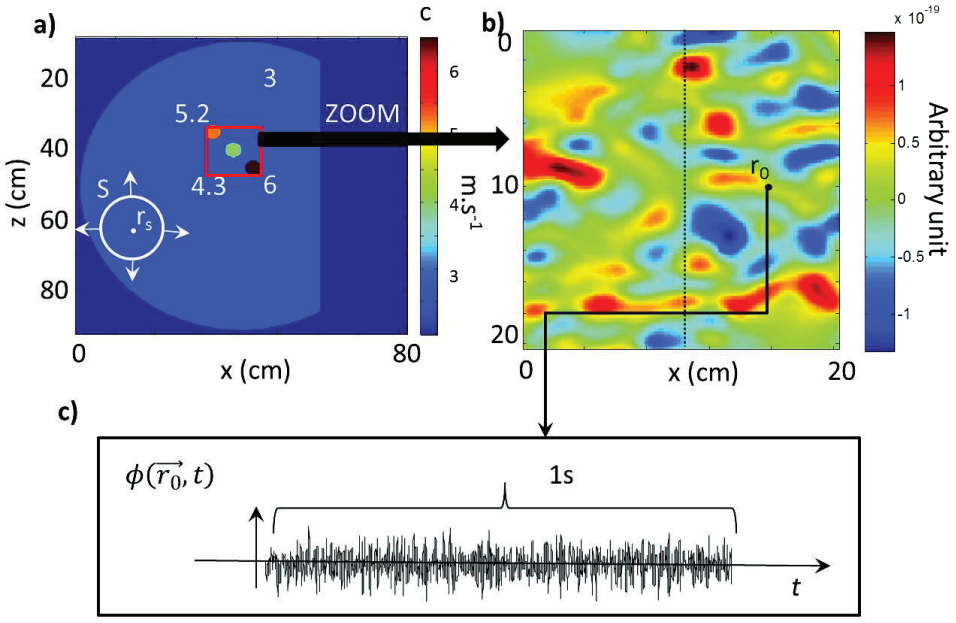

Figure 2.2. Finite difference simulation tests for the passive shear wave imaging. a) A lossless reverberating cavity (a circle with one segment cut-off) contains three inclusions with different shear wave speed. b) Zoom of the fluctuating field $\phi(t)$ in the region of the three inclusions perfectly invisible. c) A typical noise like signal measured on R.

The shear waves are created with a 100 Hz pulses source S, set at position $\overrightarrow{r_s}$ of coordinates x = 20 cm and z = 60 cm. Then, a typical diffuse field (Weaver, 1982) is created from the multiple reverberations of the trapped waves on the boundaries of the cavity (Fig 2.2 b). In a first place this reverberating wave field will be sampled at 1000 Hz and recorded during 3 seconds on each point of the 20 by 20 cm rectangle on the area of the three inclusions.

From a scalar and a linear system point of view, the wave field $\boldsymbol{\phi(\overrightarrow{r_0}, t)}$ (Fig 2.2 c) can be expressed as a time-convolution product of the source function $\boldsymbol{s\,(\overrightarrow{r_s}, t)}$ located at $\overrightarrow{r_s}$ and the impulse response $\boldsymbol{h\,(\overrightarrow{r_0},\ \overrightarrow{r_s},\ t)}$ of the propagation medium between the source location and a receiver located at $\overrightarrow{r_0}$

$$\boldsymbol{\phi(\overrightarrow{r_0},\ t) = s\,(\overrightarrow{r_s},\ t) \overset{\otimes}{_t} h\,(\overrightarrow{r_0},\ \overrightarrow{r_s},\ t)} \qquad \textbf{(2.1)}$$

The time reversed field is simply computed by replacing the excitation function $\boldsymbol{s}\,(\overrightarrow{\boldsymbol{r_s}}, \boldsymbol{t})$ by the time reversal of the impulse response at a given location $\overrightarrow{\boldsymbol{r_0}}$

$$\boldsymbol{\phi^{TR}}(\overrightarrow{\boldsymbol{r}},\ \boldsymbol{t}) = \ \boldsymbol{s}\,(\overrightarrow{\boldsymbol{r_s}}, \boldsymbol{t}) \overset{\otimes}{_{\boldsymbol{t}}}\ \boldsymbol{h}\,(\overrightarrow{\boldsymbol{r_0}},\ \overrightarrow{\boldsymbol{r_s}}, -\boldsymbol{t}) \overset{\otimes}{_{\boldsymbol{t}}}\ \boldsymbol{h}\,(\overrightarrow{\boldsymbol{r}},\ \overrightarrow{\boldsymbol{r_s}},\ \boldsymbol{t}) \qquad \textbf{(2.2)}$$

This approach of time reversal is known as the monopole time reversal (de Rosny and Fink, 2007). It differs from the perfect time reversal in the way that it straightly expresses the impulse responses as correlation. A perfect time reversal would be equivalent to the time derivative of the correlation (Roux et al., 2005). Whatever monopole or perfect, the time reversal approach developed in this section is not impacted by this latter time derivative. This approximation is generally adopted by seismologist.

Equation (2.2) is valid for point, pulsed sources and can be generalized to sources with any spatial dimension and with any time dependence (Derode et al., 2003b). As a consequence, to any field that obeys the wave equation, one can associate the following generalized time reversal field:

$$\boldsymbol{\phi^{TR}}(\overrightarrow{\boldsymbol{r}},\ \boldsymbol{t}) = \ \boldsymbol{\phi}(\overrightarrow{\boldsymbol{r_0}}, -\boldsymbol{t}) \overset{\otimes}{_{\boldsymbol{t}}}\ \boldsymbol{\phi}(\overrightarrow{\boldsymbol{r}},\ \boldsymbol{t}) \qquad \textbf{(2.3)}$$

This expression is the generalized form of the time reversal (TR) field, is known in seismology as coda wave interferometry (Shapiro et al., 2005) and it's happens to be the spatio-temporal correlation from a signal processing point of view. However, the physical interpretation of time reversal is kept in mind. The Green's function is retrieved from the displacement field along the vertical dotted line (Fig 2.2 b) by a correlation between two measurements points of a broad band and diffuse wave field through Equation (2.3). The spatial position of the virtual source is chosen to be at z = 10 cm.

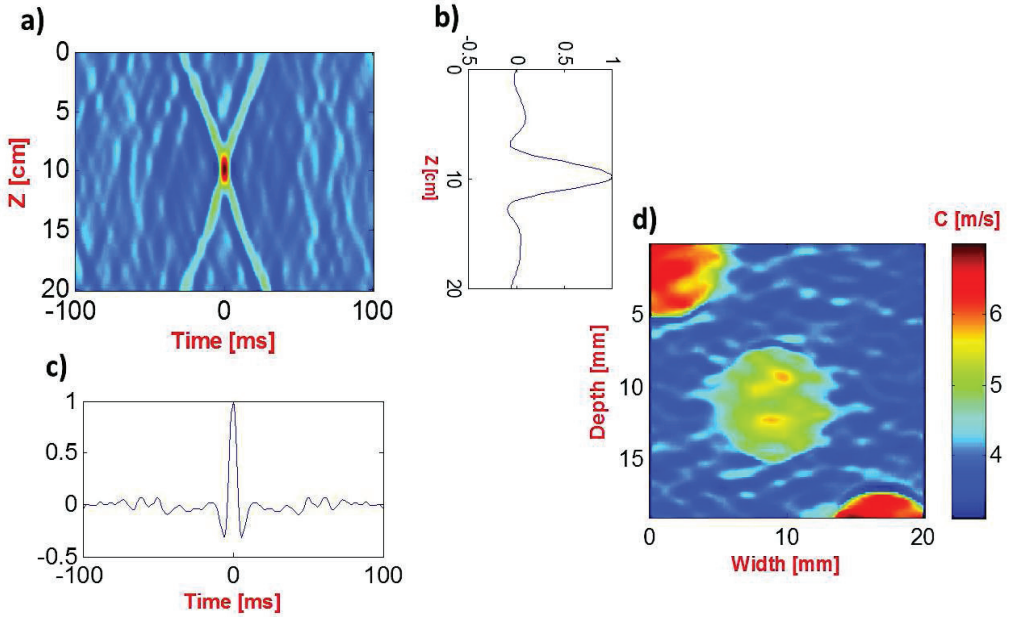

Figure 2.3. a) Spatio-temporal correlation field centered on point r_0 = 10cm, along the dashed line (fig 2.2 b). b) focal spot. c) time recompression profile. d) shear wave speed tomography.

The spatio-temporal representation of the correlation field (Fig 2.3 a), happens to be the Green's functions. The maximum of the correlation corresponds to the autocorrelation a time t = 0. The converging wave are presented before the focalization of the wave in negative time (Fig 2.3 a) and the diverging waves in the positive time. This is equivalent to the second step of a perfect time reversal experiment, the time reversal step. The back propagated wave converge and focuses at the source position then divrege. The time recompression (Fig 2.3 c) and the focal spot (Fig 2.3 b) are also representative of the mean period and wavelength of the diffuse field. Thus, correlation of broad band and diffuse wave field allows to retrieve Green's functions between any pair of measuring points (Gouédard et al., 2008). Two measurements can be extracted from this typical Green function (Gallot et al., 2011): 1) a shear wave speed tomography, computed from the slope of the converging and the diverging waves. 2) The full width at half maximum is equal to the half of the local wavelength.

We propose in this thesis a novel algorithm based on the noise correlation. It combines the correlation of the field, its gradient, and its time derivative.

The Strain field $\xi_z = \frac{\partial \phi}{\partial z}$, which is the spatial derivative of the wave field $\phi(\overrightarrow{r_0}, t)$ in the source direction z, obeys to the wave equation as well and can be expressed under the generalized time reversal form (Equation 2.4).

$$\xi_Z^{TR}(\overrightarrow{r}, t) = \xi_z(\overrightarrow{r_0}, -t) \overset{\otimes}{t} \xi_z(\overrightarrow{r}, t) \tag{2.4}$$

This is also true for the particle velocity $v_z = \frac{\partial \phi}{\partial t}$, i.e. the time derivative of the displacement field $\phi(\overrightarrow{r_0}, t)$.

$$V^{TR}(\overrightarrow{r}, t) = v(\overrightarrow{r_0}, -t) \overset{\otimes}{t} v(\overrightarrow{r}, t) \tag{2.5}$$

ξ_Z^{TR} is the time reversed strain field (dimensionless) whereas the time reversed particle velocity field V^{TR} has the dimension of the square of the particle velocity and the dimension of the time reversed displacement field ϕ^{TR} is the square of the displacement field.

Now we consider the focusing time t = 0 s for the source $\overrightarrow{r_0}$, only, which corresponds to the autocorrelation from a signal processing point of view. In what follow this point will be indicated by a subscript 0, i.e. $\phi^{TR}(\overrightarrow{r}_0, \overrightarrow{r}_0, t = 0) \equiv \phi_0^{TR}$.

In an ideal isotropic diffuse field, the plane wave decomposition of a monochromatic plane wave $\phi = e^{i(kx - wt)}$ at this given frequency allows using the approximation of the real part of the strain as $\xi_z \approx k\phi$ and the real part of the particle velocity as $v \approx -\omega\phi$, with k the wave number and ω the angular frequency. It can be deduced that, the three forms of the time reversed fields (Equation 2.3, 2.4 and 2.5) are linked according to

$$\begin{cases} V_0^{TR} \cong \omega^2 \phi_0^{TR} \\ \xi_0^{TR} \cong k^2 \phi_0^{TR} \end{cases} \tag{2.6}$$

From the coefficients of proportionality i.e. k and ω in (Equation 2.6) the local shear wave speed "c" can be estimated:

$$c \cong \frac{\omega}{k} \cong \sqrt{\frac{V_0^{TR}}{\xi_0^{TR}}} \tag{2.7}$$

By focusing on each point of the domain the particle velocity and the strain fields, a 2D local shear wave speed map can be constructed (Fig 2.3 d). The shear wave speed in the three inclusions are well retrieved (5.8 m/s, 4.9 m/s, 6.2 m/s and 3.6 m/ respectively for top inclusion, center, bottom inclusion and the solid). The small difference between the theoretical value of the shear wave speed and the values retrieved with our algorithm are due to the diffraction of a point-like source in an elastic media (Benech et al., 2013).

These results validate the assumption of plane wave decomposition used to obtain (Equation 2.6). As mentioned before, in this first simulation, the wave field was sampled at 1000 Hz according to Shannon-Nyquist theorem. This means that the temporal and the spatial information are available in the recorded data. This configuration will be tested experimentally (cf. section N°4) using an ultrafast ultrasound scanner on a calibrated phantom and in-vivo.

However, low frame rate imaging systems such as: conventional ultrasonic scanner (typically 25 frames / second), Magnetic Resonance Imaging scanner (typically one frame / second) and Optical Coherence Tomography systems (OCT) are widely used nowadays. Thus a second configuration is tested: a 25Hz frame rate perfectly compatible with most nowadays ultrasonic scanner is used in simulation to sample a 100 Hz central frequency diffuse field. As an inevitable consequence of this slow imaging frame rate, each field measurement can be considered as the result of a random process. This is clearly apparent on the spatio-temporal correlation where the typical cross has disappeared (Fig 2.4 a). The time coherence is now a delta-function which expresses the independence of each realization of the field measurement (Fig 2.4 c). In contrast, the spatial coherence is unchanged(Fig 2.4 b). Thus the loss of time information avoids computing the time-reversal particle velocity V^{TR}, but the survival of space information allows estimating ϕ_0^{TR} and $\xi_0^{TR}$and as a consequence constructing a wavelength tomography from Equation 2.8:

$$\lambda \approx 2\pi \sqrt{\frac{\phi_0^{TR}}{\xi_0^{TR}}} \qquad \textbf{(2.8)}$$

The local shear wavelength tomography is presented in (Fig 2.4 d), the three inclusions are clearly retrieved with the same contrast as in the shear wave speed tomography. The measured shear wavelength are also representative of the local elasticity.

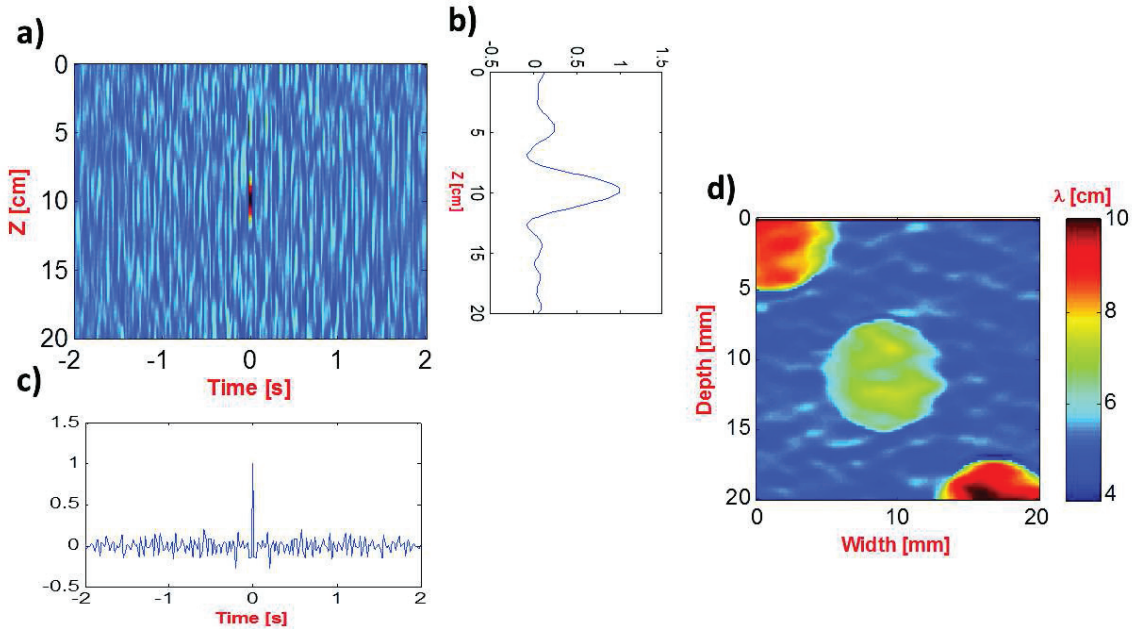

Figure 2.4. a) Spatio-temporal correlation field centered on point r0 along the dashed line (fig 2.2 b). b) focal spot. c) Time recompression profile. d) Shear wavelength tomography.

Once again, this configuration was tested experimentally with three low frame rate imaging systems. First, passive shear wavelength tomography was conducted on a brain of a healthy volunteer. Second, monitoring of High Intensity Focused Ultrasound (HIFU) treatment was tested on porcine pancreas with a conventional ultrasound scanner. Finally, Optical Coherence Tomography (OCT) was conducted in-vivo on the cornea of an anesthetized rat.

3 Passive Elastography Using Low Frame Rate Scanners

Shear Wavelength Tomography in MRI, OCT and Ultrasound

It is commonly supposed that noise obscures but does not contain useful information. However in wave physics and especially in seismology, scientists developed some tools known as "noise correlation" to extract useful information and to construct images from the random vibrations of a medium. Living tissues are full of unexploited vibrations as well. In this manuscript we show that noise correlation techniques can conduct to a tomography related to the stiffness that physicians estimate during a palpation exam. This chapter gathers three papers with low frame rate scanners (i.e. MRI, OCT, ultrasound). They have been slightly modified compared to the published version to avoid redundancy with the state of the art and the theory cf. section N°1 and 2.

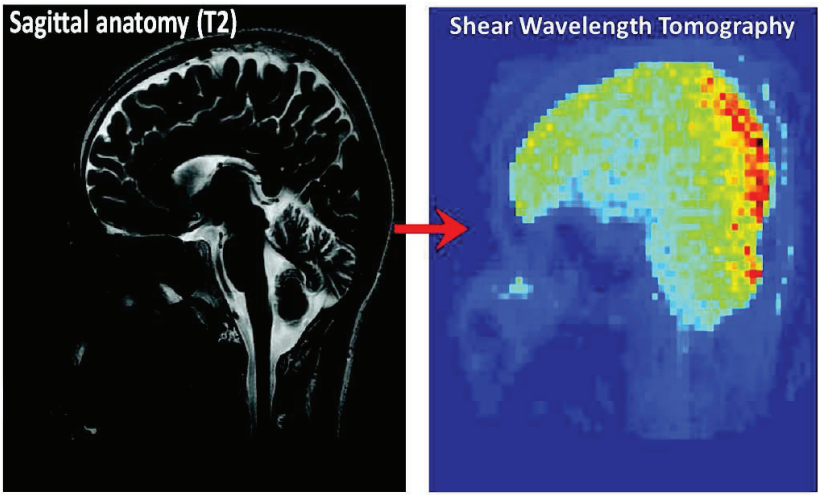

3.1 Magnetic Resonance Imagin: Brain Palpation from Physiological Vibrations Using

Published on PNAS

Zorgani, A., Souchon, R., Dinh, A.-H., Chapelon, J.-Y., Ménager, J.-M., Lounis, S., Rouvière, O., Catheline, S., 2015. Brain palpation from physiological vibrations using MRI. Proc. Natl. Acad. Sci. 112, 12917–12921.

3.1.1 Abstract

We present a magnetic resonance elastography approach for tissue characterization that is inspired by seismic-noise correlation and time reversal. The idea consists of extracting the elasticity from the natural shear waves in living tissues that are due to cardiac motion, blood pulsatility, and any muscle activity. In contrast to other magnetic resonance elastography techniques, this noise-based approach is thus passive and broad-band, and does not need any synchronization with sources. The experimental demonstration is conducted in a calibrated phantom and in-vivo in the brain of two healthy volunteers. Potential applications of this 'brain palpation' approach for characterizing brain anomalies and diseases are foreseen.

3.1.2 Introduction

The complexity of wave fields can sometimes be an advantage for imaging. Such is the case in multiple scattering or reverberating media where wave fields contain information about their sources and about the medium itself. Turning this wave noise into useful measurements through correlation techniques has provided a break-through in a wide variety of domains, which range from seismology (Duvall Jr et al., 1993) to acoustics (Sabra et al., 2007; Weaver and Lobkis, 2001) and electromagnetism (Lerosey et al., 2007). Living tissue is also full of unexploited vibrations. Their detection with ultrafast ultrasound scanners that can reach thousands of frames per second (Sandrin et al., 1999; Nightingale et al., 2002a; Bercoff et al., 2004a) has recently opened up the medical field to correlation techniques, and therefore to passive elastography (Gallot et al., 2011). However, ultrasound is not suitable for brain imaging. Magnetic resonance imaging (MRI) can image the brain, but its relatively low acquisition rate of a few frames per second is an issue. Synchronization with the shear-wave source is thus necessary (Muthupillai et al., 1995; Plewes et al., 1995), which penalizes its potential implementation based upon natural shear waves.

We describe a magnetic resonance elastography (MRE)-based method that is free from the need for synchronization and for any controlled source. This approach extracts information related to the mechanical properties of the soft tissue from hundreds of snapshots of randomly fluctuating shear-wave fields. The key to the decrypting of the complex field is correlation, or similarly, but from a physical point of view, time reversal (Derode et al., 2003c; Fink, 1997). Not only does this wide-band approach maximize the signal-to-noise ratio, as any matched filter would, but it also avoids the Nyquist–Shannon problem that is inherent to slow imaging devices. Indeed, although time information is definitely lost, the spatial information is still present and allows shear-wavelength tomography to be conducted. This wavelength is closely related to the shear elasticity, and thus to the intuitive estimation of the stiffness felt by physicians during palpation examination. To start with, this concept is demonstrated using MRI in a calibrated elastography phantom under randomly sampled vibrations. Arterial pulsation can produce motion in the brain as high as 1 mm (Weaver et al., 2012); the resulting natural shear-wave field is analyzed through correlation algorithms and passive brain palpation reconstructions are presented.

3.1.3 Phantom experiments

As shown in the experimental set-up (Fig. 3.1 A), vibrations are generated synchronously from 12 contact-points of a device mounted on a piezo-electric source and working with a 80.3-s modulated sinusoid excitation. The emitted frequencies range from 20 Hz to 200 Hz. These vibrations propagate mainly as shear waves within a phantom designed for elastography tests (CIRS®; Computerized Imaging Reference Systems, Inc.) that contains four calibrated inclusions. The emitted waves reverberate inside this soft, solid cavity, and the resulting complex field is measured every 1.5 s using a MRI scanner. It is important to point out firstly that the vibrations driving is continuously repeated during the whole acquisition time and secondly that the modulated sinusoid duration of 80.3 s divided by the imaging frame rate of 1.5 s is not an integer in order to avoid any cyclic sampling of the field. Each frame contains 128 × 128 pixels. The acquisition of 320 frames for the out-of-plane component of the displacement field was carried out at ~0.7 Hz on six slices that were equally spaced by 3 mm, with 3 × 3 × 3 mm^3 isotropic voxels, over 8 min. According to the Nyquist–Shannon limit, the maximum shear-wave frequency was thus ~0.35 Hz, which is far below the central frequency of shear waves in the experiment. The first six consecutive snapshots of the displacement field of a total of 320 snapshots are shown in Figure 3.1.B. These clearly show the rectangular phantom surrounded by the random-phase noise. The elastic field shows complex spatial patterns with characteristic dimensions driven by the wavelengths associated with the 20 Hz to 200 Hz frequency content of the sweep-source signal. Small wavelengths are visible at t = 1.5 s, whereas larger wavelengths

dominate at t = 3 s. A correlation coefficient smaller than 5% between consecutive snapshots of wave pattern confirms the random property of the diffuse elastic field. The extraction of the elastic parameters from the 320 snapshots was then carried out using noise correlation.

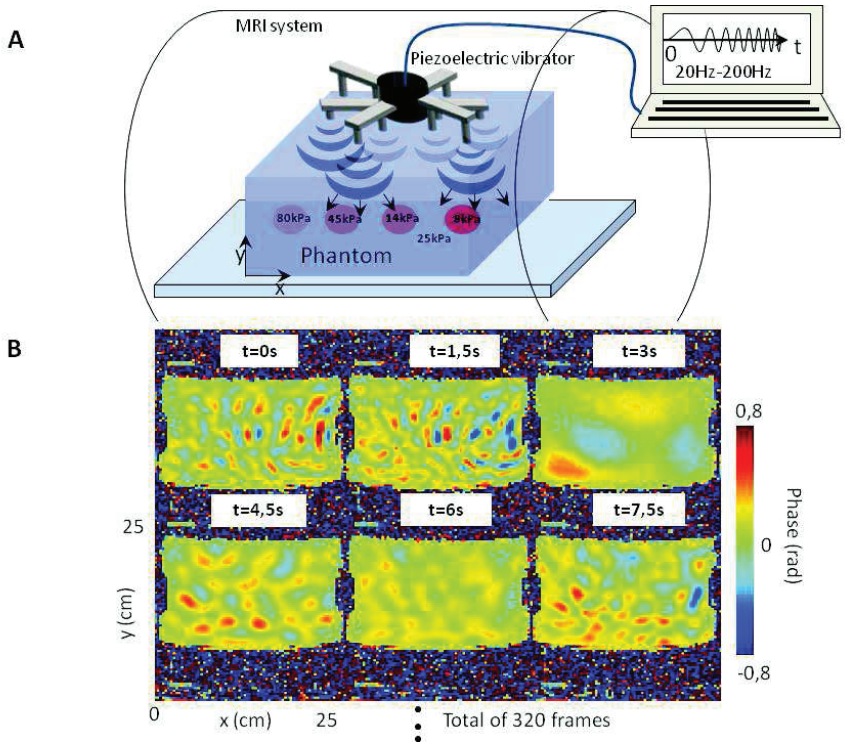

Figure 3.1. (A) Experimental set-up. The complex shear-wave field is generated from 12 point-sources located at the surface and mounted on a MRI-compatible piezo-electric vibrator. The excitation signal is a 80.3 s modulated sinusoid, with the frequency range of 20 Hz to 200 Hz. (B) Phase images that represent the out-of-plane displacement field u_y in the zx-plane of the inclusions. These first six snapshots were extracted from a movie of 320 images that was acquired using a gradient-echo MRE sequence every 1.5 s.

3.1.4 Theory

This part of the paper was slightly modified to avoid repetition with the theory presented in section N° 2.3. Let $\phi_i(\vec{r},t)$ be the experimental observation of the i-component of an elastic wave field, i=1,2,3. Then a time convolution product between $\phi_i(\vec{r},t)$ and the time-reversed field $\phi_i(\vec{r},-t)$ of a virtual point source located at $\overrightarrow{r_0}$ is computed following Equation (2.3). This equation is widely used in seismology (Campillo and Paul, 2003; Snieder et al., 2007) and is known as correlation. Using a first signal analysis interpretation of ϕ_i^{TR}, it is quite straightforward to realize that its maximum, the autocorrelation, is reached on the virtual point-source located on $\vec{r} = \overrightarrow{r_0}$ and for the zero-lag time $t_0 = 0s$. From this point $\overrightarrow{r_0}$, the spatial

coherence slowly decreases, and it has a typical length that is proportional to the mean wavelength. Indeed, snapshots are acquired at a sampling time longer than the mean wave period. Therefore, they show independent wave patterns which prevent the determination of the exact time-course of the wave. Nevertheless, the existence of wave patterns implies that motion in one region is correlated with motion in its vicinity at a distance of a mean wavelength. This spatial extension is the key parameter to estimate the shear wavelength. It is close to what is known as the Spectral AutoCorrelation (SPAC) method in seismology. A second physical time-reversal interpretation of correlation states that ϕ_i^{TR} is the field that would be observed if the sources responsible for the noise waves were able to be controlled and were acting as a time-reversal mirror. The waves would thus back-propagate and reach the location of the virtual point-source $\overrightarrow{r_0}$ at a special spatio-temporal refocusing time t_0. The energy concentration at t_0 defines a region around the virtual source $\overrightarrow{r_0}$, called the focal spot. This offers a simple and robust way to estimate the mean wavelength (Fig. 3.2 A); indeed the time-reversal focal spot reaches the diffraction limit that is known as the Rayleigh criterion (Catheline et al., 2008; de Rosny and Fink, 2002). The sampling rate under the Nyquist–Shannon limit prevents the computation of the time-reversal field as a function of time, but leaves the spatio-temporal refocusing at time t_0 unaltered (Benech et al., 2013; Catheline et al., 2013). The extraction of the shear-wave length, as spatial information, from this latter time-reversal field $\phi_i^{TR}(\vec{r},t)$ does not contradict the Nyquist–Shannon sampling theorem that addresses time information. However, the wave-frequency part of the time information is lost. A complete shear-wave speed estimation using the present approach would thus need an independent measurement of frequency. The local wavelength estimation on the virtual point-source located on $\vec{r}=\vec{r}_0$ is extracted from the focal spot along one axis *j*, according to equation 2.8. The autocorrelation of the field gradient (Equation 2.6) is thus equivalent to a curvature measurement, similar to the Laplacian computation used in MRE reconstruction algorithms. It is now straightforward to deduce Equation 2.6. Although in theory the wavelength can be estimated along three orthogonal directions *j*, it is limited in practice to the two dimensions of slices; a full 3D MRE sequence is still to be tested. Moreover, in isotropic media, one direction only is sufficient. The brain anisotropy is ignored in this manuscript. Finally, Equation (2.6) has been validated through simulations and experiments using ultrasounds (Catheline et al., 2013).

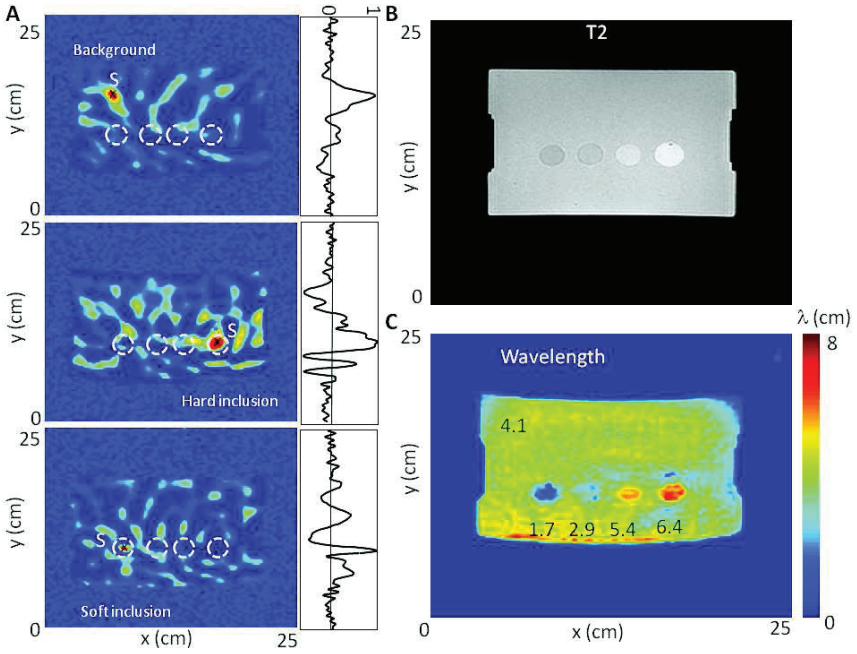

Figure 3.2. Phantom correlation results (A) Time-reversal focal spots for three different virtual-source locations S in the phantom background (25 kPa; top), the hard inclusion (80 kPa; middle) and the soft inclusion (8 kPa; bottom). The virtual source S can be set arbitrarily to any location. (B) T2-weighted image of the phantom. (C) Shear-wavelength tomography. The four inclusions are clearly apparent, and their local wavelength estimations are proportional to the square root of their local elasticity.

The dimensions of the focal spot vary according to the local stiffness of the medium at the location $\vec{r}_0$ chosen for the virtual point-source: a small focal spot in the soft inclusion, a medium one in the background, and a large one in the hard inclusion (Fig. 3.2 A). The same logic holds for the focal spots in the two remaining inclusions (Fig. S1). As a consequence, by sequentially selecting each point of the field as a virtual source location $\vec{r}_0$, tomography of the wavelength is conducted in a processing time of 1 s. Compared with a T2-weighted sequence (Fig. 3.2 B), the wavelength tomography shows good agreement on the location and the size of the four inclusions (Fig. 3.2 C); a slight global distortion probably introduced by the presence of the motion-encoding gradient is also visible. As expected, their growing stiffness is clearly apparent from left to right. When accounting for frequency-dependent motion-encoding gradient sensitivity, the central frequency of the vibrations measured within the phantom is ~80 Hz. At 80 Hz, the estimated shear-wavelengths are 1.7 cm, 2.9 cm, 5.4 cm, 6.4 cm in each inclusion, respectively, and 3.6 cm in the background. Based on the relationship $\lambda = \sqrt{\frac{E}{3\rho f_0^2}}$ and on Young's modulus

E provided by the manufacturer, the expected shear-wavelengths are 2.0 cm, 2.7 cm, 4.8 cm, 6.5 cm in each inclusion, respectively, and 3.6 cm in the background. As mentioned earlier, the correlation approach is efficient for a perfect diffuse field with the properties of equipartition (Roux et al., 2005). From this point of view, the multiple sources used in the experiment have two flaws. First, they are located on the surface, and second, they deliver synchronous vibrations. Although it is more difficult to experimentally implement, independent sources that are randomly distributed in the bulk represents the ideal situation of a perfect diffuse field for noise-correlation techniques. Therefore the imperfect source of this initial set-up appears to be at the origin of the fluctuations in the wavelength tomography (Fig. 3.2 C, Fig. S2). An inverse-filter solution was proposed for seismic data (Gallot et al., 2012). In the present case, a spatial mean of $\Psi_i^{TR}(\vec{r}\,,t_0)$ can be simple and efficient. A typical 8-min MRE sequence only allows the acquisition of 320 frames of the elastic field, which is some 10% to 30% of that acquired in experiments conducted with ultrasounds (Catheline et al., 2013). However, the correlation-based wavelength tomography clearly opens promising perspectives, and these were also tested here with the brains of two healthy adult volunteers.

3.1.5 Brain experiments

The aim of passive elastography is to use natural shear-wave propagation in the human body. In the brain, the natural motion is due to arterial pulsatility and cerebrospinal fluid exchange (Arani et al., 2015; McGarry et al., 2015). The MRE sequence presented in this section is the same as the one described for the phantom except for the three following parameters: the voxel size of the 6 slices is $4 \times 4 \times 4$ mm^3 in order to improve the SNR, the total time of the *in vivo* experiments is 11 minutes and the 3 components of the displacements are acquired. The out-of-plane component only is investigated here. The first six 64×64 pixels snapshots in Figure (3.3 A) show that the MRE sequence described in the materials and methods section can reveal the natural motion in the brain. The amplitudes are relatively small, at only 5 µm, but the signal is clearly apparent. As correlation computation is equivalent to an adaptive filter, the focal spot clearly emerges from the noise (Fig. 3.3 B). The existence of these time reversal focus spots are a convincing clue that natural motions in the brain are transported by shear waves; They are responsible for correlation decreasing down to negative values. The black -6 dB isolevel boundary lines more clearly illustrate the different sizes of the focal spots. With a mean of 10 cm, the wavelength estimations are within the expected range.

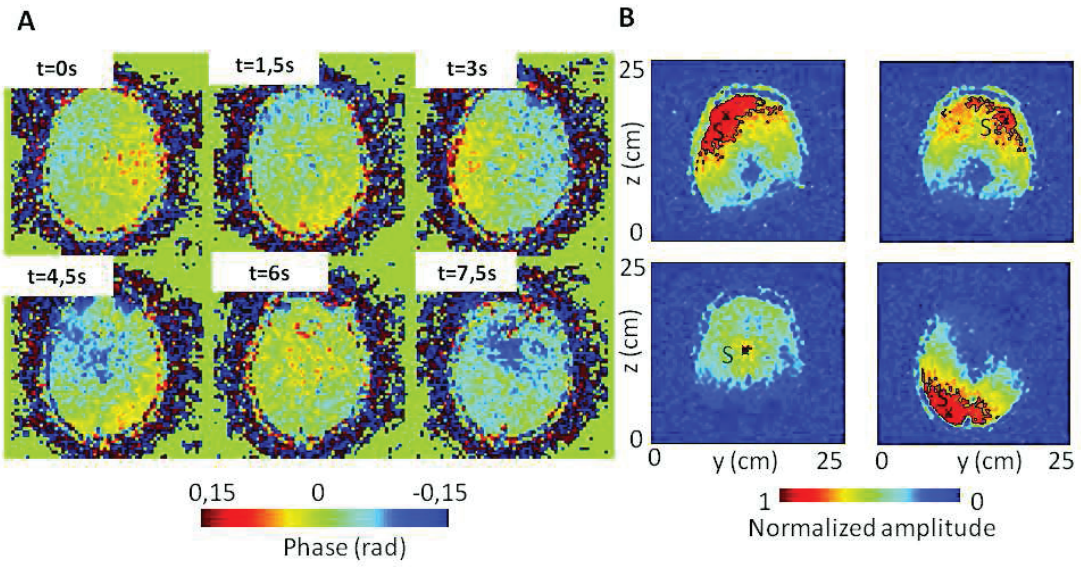

Figure 3.3 In vivo brain results. (A) Phase representation of the displacement field. Six snapshots were extracted from a movie of 144 images. These in-vivo measurements of brain motion were acquired with a gradient-echo MRE sequence every 1.5 s. (B) Time-reversal focal spots in the brain for four different virtual-source locations S. The isolevel black boundary lines stress the shear-wavelength variations.

Indeed assuming that the motion is proportional to the intracranial pressure (Wagshul et al., 2011), and given the frequency-dependent sensitivity of the 50 Hz motion-encoding gradient used in our *in-vivo* experiment, the central frequency of displacement (as encoded in the phase images) is expected to be ~1 Hz (Weaver et al., 2012). 10% of energy is nonetheless present at a frequency of 15Hz. Shear-wave speed estimation in the brain is between 1 m/s and 2 m/s (Kruse et al., 2008; Sack et al., 2008). Therefore, the expected smaller wavelength ranges from 8 cm to 15 cm. In addition, longer wavelengths are observed on the periphery of the frontal and parietal lobes than in the center of the brain (Fig. 3.3 B) which is clearly confirmed by the shear-wavelength tomography reconstructions (Fig. 3.4). The anatomic details of T2 images are apparent on the shear-wavelength tomography, especially along the longitudinal fissure in the axial view (Fig. 3.4 A). Finally, longest wavelengths are visible in the posterior region of the brain (Figs. 3.4 A, 3.4 B).

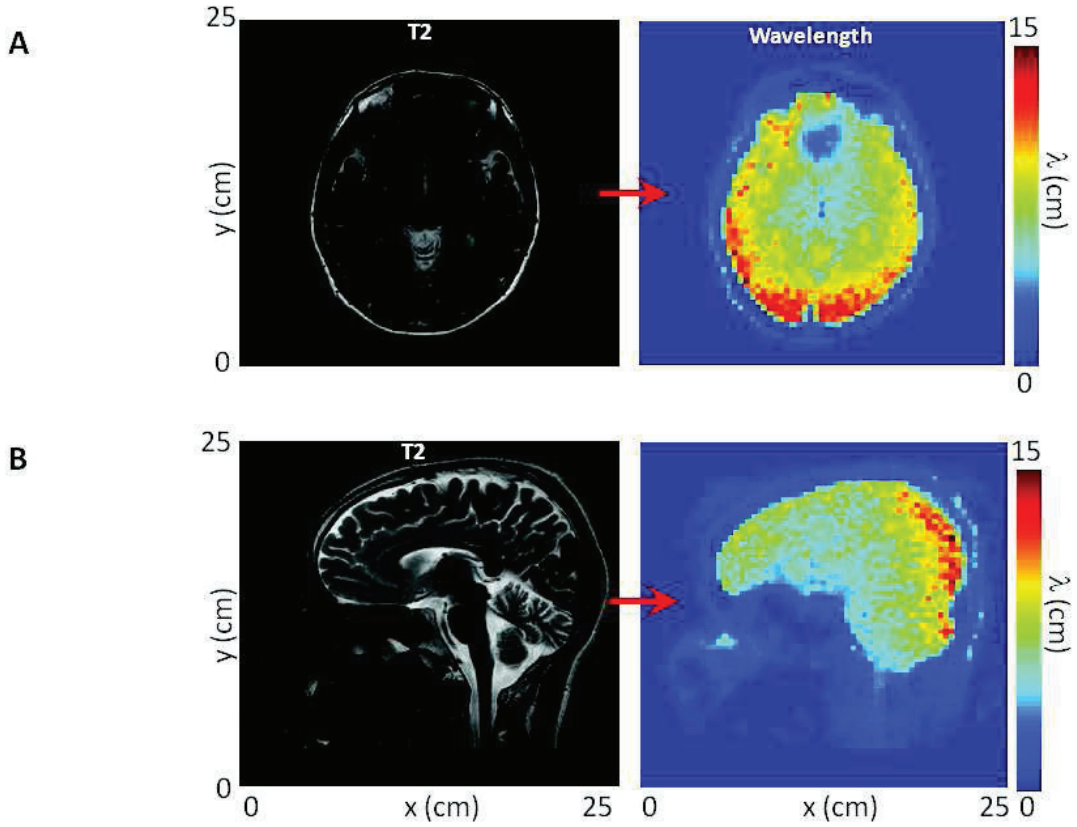

Figure 3.4 In vivo brain passive MRE. (A) Axial view of the T2-weighted image (left) and its corresponding shear-wavelength tomography (right). (B) Sagital view of the T2-weighted image (left) and its corresponding shear-wavelength tomography (right).

3.1.6 Discussions

The general results extracted from the first brain correlation reconstructions were verified on the same volunteer at a 1-month interval, as well as on a second healthy volunteer (Figs. S3, S4). Healthy volunteers were lying on the back. The gravity induced compression might enhance the local wavelength in the posterior brain. Further studies of passive MRE are necessary to claim with confidence that these red posterior regions of the wavelength-tomography reconstructions correspond to stiffer brain tissue (Fig. 3.4, Fig. S4). Similarly, the apparent stiffer periphery region is not confirmed by MRE observations of the literature. Since it has to be a wave property effect, it is conjectured to be either a non-uniform frequency content of the shear wave field or a change in the nature of the elastic wave with internal structure. At last, given that MRE includes three components of the field, that two orthogonal wavelength estimations are possible, and that the acquisition involves six different planes, we therefore end up with 36 possible tomography

reconstructions. It is beyond the scope of the present paper to offer detailed descriptions of each of these, although they are partly considered in the Supplementary Material. A promising possibility resides in the wave vector estimation that should partly reveal the brain anisotropy. In conclusion, the whole set of these experimental data brings us to the following statement: although natural tissue vibrations are often considered as disturbing noise, they nonetheless offer promising opportunities for medical imaging when correlation methods can be applied.

3.1.7 Materials and Methods

Instantaneous MRI snapshots are captured using a gradient-echo single-shot echo planar imaging sequence (Souchon et al., 2008) developed at the Mayo Clinic (Rochester, Minnesota), and installed on a 1.5 T system (General Electric). The displacement is encoded in the phase of the magnetic resonance signal using a 20-mT/m bipolar motion-encoding gradient applied over 10 ms (i.e., +20 mT/m over 5 ms, immediately followed by -20 mT/m over 5 ms). The Repetition Time (TR) and the Echo Time (TE) are 1.5 s and 45 ms respectively. In the phantom experiment the field of view (FOV) is 128 × 128 × 3 mm whereas it is 64 × 64 × 4 mm in the brain experiment. The phantom is designed for elastography experiments by the company CIRS (Computerized Imaging Reference Systems, Inc). The piezoelectric vibrator used in the phantom experiment is a PPA20M Cedrat Technologies.

Acknowledgments. We gratefully acknowledge R. Ehman and K. Glaser from the Mayo Clinic for making the MRE sequences available.

3.1.8 Supplement materials

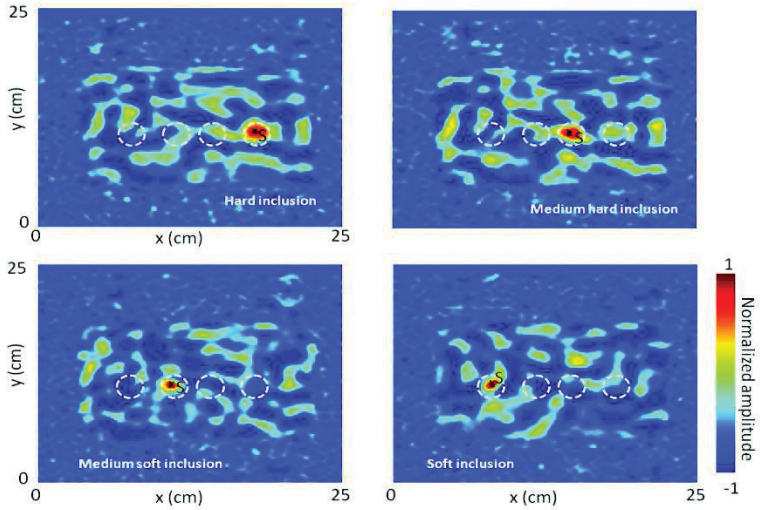

Figure S1. Time-reversal focal spots on three different virtual source locations S in the inclusions presenting different Young Moduli: hard (80 kPa), medium hard (45 kPa), medium soft (14 kPa) and soft (8 kPa). An accurate estimation of the focus spot size resulting from correlation follows its theoretical dependence as the square root of the Young modulus.

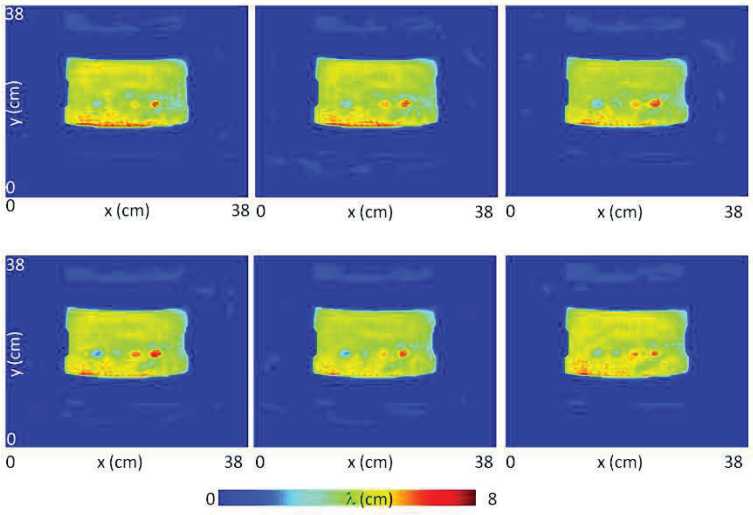

Figure S2. Shear wavelength tomography. The six 2 cm sized inclusions are clearly apparent in the four different slices equally spaced by 3 mm. The bottom left reconstruction is presented in the article (Fig.3.2 C).

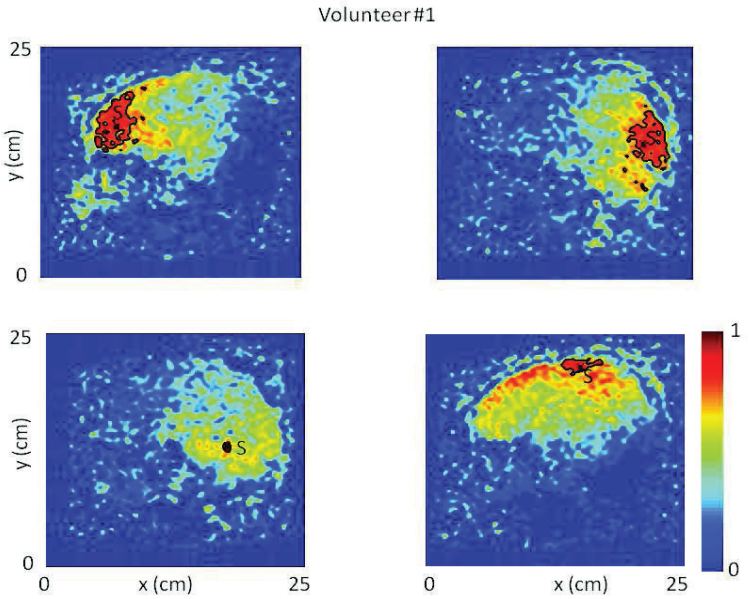

Figure S3. Time-reversal focal spots on four different virtual source locations S. They are measured from a sagittal slice in the brain. Iso-level black curves stress the shear wave-length variations. The corresponding shear wavelength tomography is shown in the article (Fig.3.4 B).

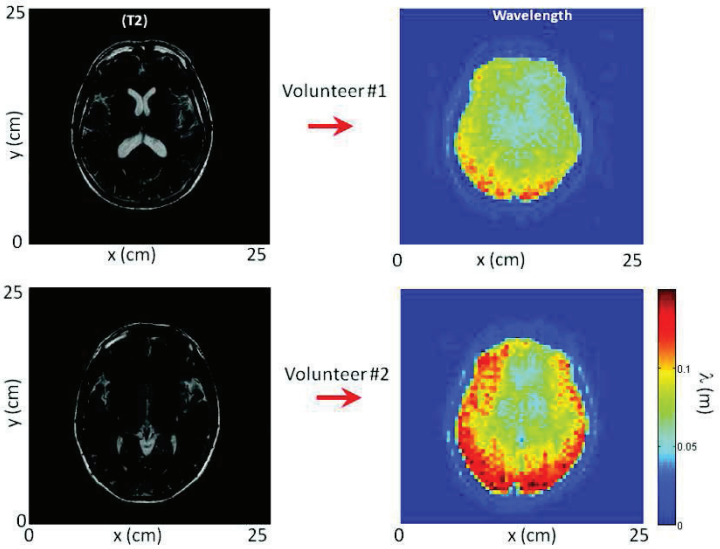

Figure S4. Time-reversal focal spots on four different virtual source locations S. They are measured from a sagittal slice in the brain. Iso-level black curves stress the shear wave-length variations. The corresponding shear wavelength tomography is shown in the article (Fig.3.4 B).

3.2 Optical Coherence Tomography: towards passive elastography on the cornea of anesthetized rat

Submitted to Journal of Biomedical Optics

"Diffuse shear wave imaging: towards passive elastography using low frame rate spectral-domain Optical Coherence Tomography". Thu-Mai Nguyen*, Ali Zorgani*, Maxime Lescanne, Albert Claude Boccara, Mathias Fink, and Stefan Catheline.

* These two authors have equal contributions to the presented work.

3.2.1 Abstract

Optical Coherence Tomography (OCT) can map the stiffness of biological tissue by imaging mechanical perturbations (shear waves) propagating in the tissue. Classic shear wave elastography (SWE) techniques rely on active shear sources to generate controlled displacements that are tracked at ultrafast imaging rates. Here, we propose a noise-correlation approach to retrieve stiffness information from the imaging of diffuse shear waves using low-frame rate spectral-domain OCT. We demonstrated the method on tissue-mimicking phantoms and validated the results by comparison with classic ultrafast SWE. Then, we investigated the *in vivo* feasibility on the eye of an anesthetized rat by applying noise-correlation to naturally-occurring shear waves. The results suggest a great potential for passive elastography based on the detection of natural pulsatile motions using conventional spectral-domain OCT systems. This would facilitate the transfer of OCT-elastography to clinical practice, in particular in ophthalmology or dermatology.

3.2.2 Introduction

Dynamic shear wave elastography (SWE) consists in deducing the viscoelastic properties of soft tissue from the characteristics of mechanical perturbations propagating in the tissue. In soft, incompressible tissue, the elastic behavior is dominated by the shear modulus μ and the stiffness can be characterized by $E = 3\mu = 3\rho c_{shear}^2$, where E is the Young's modulus, ρ is the tissue density and c_{shear} is the speed of a shear wave propagating across the tissue (Royer and Dieulesaint, 2000). One of the most common SWEI technique, introduced by Sarvazyan et al. (Sarvazyan et al., 1998b), consists in actively launching a micron scale shear wave in the tissue

and tracking its propagation to measure its speed. This technique, first implemented using MRI or ultrasound imaging in the late 1990's (Bercoff et al., 2004b; Manduca et al., 2001; Nightingale et al., 2002b), has been recently extended to Optical Coherence Tomography (OCT) for elastography at micron-scale resolution with medical applications in ophthalmology and dermatology. OCT can be used for phase-sensitive speckle-tracking of displacements within tissue (Wang et al., 2006, 2007) and current technological developments enable to reach tens of kilohertz frame rates (Song et al., 2016; Wang and Larin, 2014). The OCT setups are combined with external active shear sources, such as mechanical actuators (Song et al., 2013), air-puff (Wang et al., 2012a), ultrasonic radiation force (Nguyen et al., 2015, 2014a; Razani et al., 2012a) or photoacoustic effect (Li et al., 2014). Although efficient, most of these shear sources have disadvantages limiting their use in clinical practice: mechanical actuators need to be placed in contact with the tissue; ultrasonic radiation force and photoacoustic effects expose the tissue to relatively high ultrasound pressures or high laser fluences; air-puffs have only been effective on superficial tissues so far. In ophthalmology in particular, it can be challenging to generate shear waves not only in the cornea but also in deeper ocular structures such as the crystalline lens or the retina.

Here, we propose to implement a time reversal-based approach for SWE using standard spectral-domain OCT (SD-OCT): SD-OCT is used to image a diffuse shear wave field at low frame rates (typically 200 Hz) and shear wavelengths maps are reconstructed. This method doesn't require any controlled shear source, which offers a potential for *in vivo* passive elastography, and can be realized with conventional commercial SD-OCT systems operating at low frame rates. In this paper, we present experiments performed *ex vivo* on tissue-mimicking phantoms, and compare the results with ultrafast active SWE for validation. We also performed preliminary *in vivo* passive experiments on the eye of an anesthetized rat.

3.2.3 Shear wave imaging using Spectral-domain Optical Coherence Tomography

As introduced in previous works (Song et al., 2013), SD-OCT can be used to track shear waves whether they are induced by an external shear source or by natural *in vivo* motions. Our setup is depicted in Figure 3.5. The external shear source is a piezoelectric actuator (Thorlabs AE0505D18F; Newton, NJ, USA) placed at the sample surface and generating micron-scale vibrations. The light source is a broadband super-luminescent diode (1050-nm central wavelength, 50-nm bandwidth, 25-mW maximal output power; MWTechonologies, Moreira da Maia, Portugal). The detector is a line-scan spectrometer (76-kHz maximal line rate, 2048 pixels,

1000-1100 nm spectral range, 0.2-nm spectral resolution; Wasatch Photonics, Durham, NC, USA). The spatial resolution of the system is 5 µm x 10 µm (axial x lateral). In all following sections, "z", "depth" or "axial" will refer to the direction parallel to the light beam axis in the sample arm, while "x" or "lateral" will refer to the direction perpendicular to the light beam axis. Axial displacements occurring in the sample can be detected by acquiring several A-lines in time: for a given lateral location, the phase difference $\Delta\varphi(x,z,t)$ between two consecutive A-lines is proportional to the axial displacement $u_z(x,z,t)$:

$$\Delta\boldsymbol{\varphi}(\boldsymbol{x},\boldsymbol{z},\boldsymbol{t}) = \boldsymbol{\varphi}(\boldsymbol{x},\boldsymbol{z},\boldsymbol{t}+\boldsymbol{dt}) - \boldsymbol{\varphi}(\boldsymbol{x},\boldsymbol{z},\boldsymbol{t}) = \boldsymbol{u_z}(\boldsymbol{x},\boldsymbol{z},\boldsymbol{t}).\boldsymbol{4\pi n/\lambda} \quad \textbf{(3.5)}$$

where (x,z,t) are respectively the lateral, axial and temporal coordinates, t is λ=1050 nm is the light source central wavelength and n is the sample refractive index.

In the sample arm, a galvo-mirror scans the light beam laterally across the sample. The system can be operated in two scanning modes – either a conventional low-frame rate B-mode (Figure 3.5 a) or an ultrafast M-mode (Figure 3.5 b) – as detailed in the following sections.

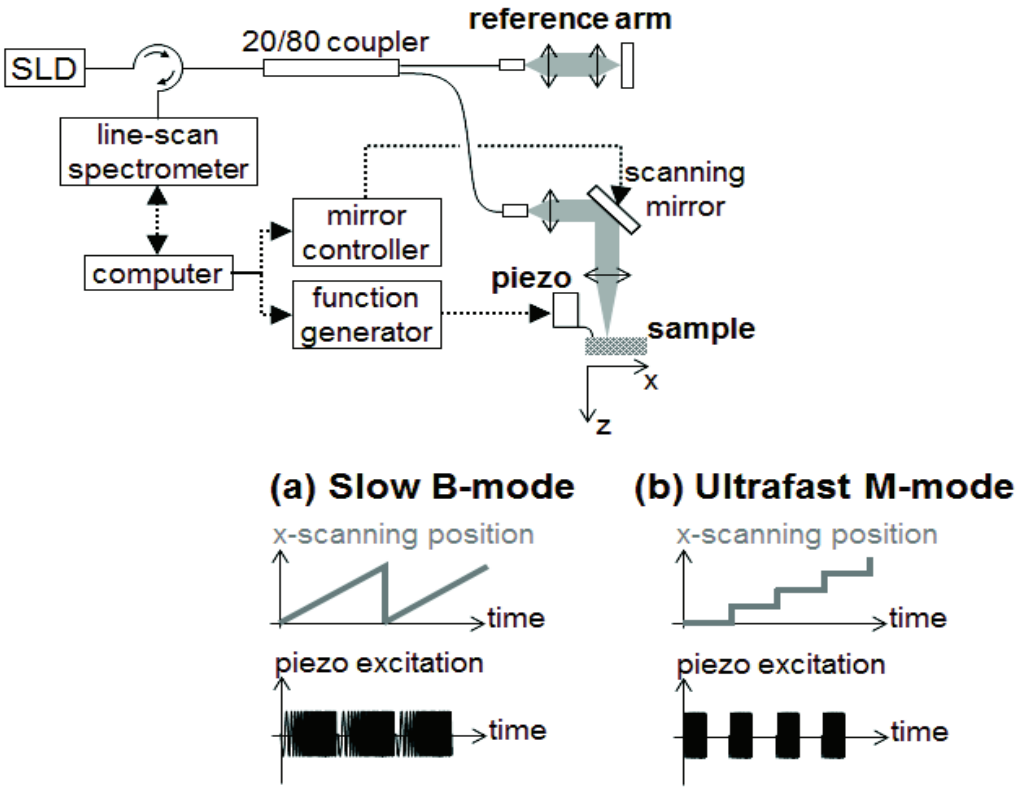

Figure 3.5 – Spectral-domain optical coherence tomography setup for elastography. The setup can be operated in two scanning modes: (a) "ultrafast" M-mode for displacement tracking at high temporal sampling rate (76 kHz), and (b) "slow" B-mode for displacement tracking at low temporal sampling rate (190 Hz). (x,z) denote respectively the lateral and axial coordinates.

3.2.4 Low-frame rate shear wave imaging

In the conventional B-mode (Figure 3.5 a), A-lines are successively acquired at 256 adjacent locations by scanning the light beam across a 2.5-mm lateral imaging range, forming a 2D image of the sample in the (x,z) plane. Time-series of images are then acquired by repeating the B-scan 256 times while the sample is continuously and randomly vibrating without any synchronization with the acquisition. The displacements are retrieved from the phase difference between A-lines corresponding to a given location. This results in a movie of the displacements $u_z(x,z,t)$ at 190 frames /second with a total recording time of 1.4 seconds.

At such a low frame rate, each frame corresponds to a different realization of a random shear wave field. In other words, the acquisition is temporally incoherent. The lateral coherence is also low since different lateral locations are imaged sequentially. Nevertheless, the axial coherence of the shear wave field is preserved since SD-OCT acquires depth profiles in a single shot, which allows determining the wavelength of the shear wave using a cross-correlation approach. Shear wavelength tomography is performed by measuring the wavelength at each depth location using equation 2.8 (cf. section 2.3).

3.2.5 Ultrafast active shear wave imaging

We performed ultrafast active shear wave imaging experiments as a control for comparison with the low-frame rate shear wave imaging experiments. The principle of ultrafast active shear wave imaging using SD-OCT has been detailed in previous studies (Song et al., 2013). In brief, in the ultrafast M-mode (Figure 3.5 a), a series of 256 consecutive A-lines are acquired at 76000 lines/sec at one given location of the sample. Time-series are then repeated at 256 adjacent lateral locations covering a 2.5-mm lateral imaging range. The shear wave is actively induced and triggered at the beginning of each time-series. The axial displacements are retrieved from the phase difference between consecutive A-lines within a time-series. The concatenation of all time-series results in a stroboscopic movie $u_z(x,z,t)$ of the shear wave propagation consisting of 256 x 256 A-lines with a sampling rate of 76 kHz. The total acquisition time is 1 second.

The local propagation speed of the shear wave is then computed by performing time-correlations of displacements recorded at adjacent positions: $c_{shear}(x, z) = \Delta x/\Delta t$ where Δt is the time needed for the shear wave to travel a distance Δx (Δx = 2 pixels = 20 µm in our case). We used the normalized correlation coefficient as a metric of the speed estimation reliability: all speed values resulting from correlation with a normalized coefficient ≤ 0.9 were ignored.

3.2.6 Ex-vivo experiments on a tissue-mimicking phantom

A tissue-mimicking phantom was made of aqueous solutions containing agarose (Sigma Aldrich, St Louis, MO, USA) for stiffness control and TiO_2 microbeads for optical scattering. The sample was made of two halves of different stiffness: the stiffer half contained 2-% agarose (w/v) while the softer half contained 1-% agarose (v/w). Both parts contained 1% (w/v) of TiO_2. Three experiments were performed:

1) An ultrafast shear wave imaging experiment with 76000 lines/sec imaging of high-frequency shear waves (500-6000 Hz). It served as control to characterize the stiffness contrast between both parts of the phantom by computing shear wave speed maps. The shear wave was induced by a single piezoelectric actuator placed at the sample surface and excited by a 2-ms chirp sweeping frequencies between 500 and 6000 Hz. The excitation was repeated synchronously with the acquisition. The resulting displacement field was processed using a pulse compression approach that provides broadband shear waves with high signal-to-noise ratio and high spatio-temporal resolution, as detailed in previous works (Nguyen et al., 2014b).

2) A low frame rate, diffuse shear wave imaging experiment with 190 frames/sec imaging of high-frequency shear waves (500-6000 Hz). A random shear wave field was induced using two piezoelectric actuators placed on the sample surface and asynchronously excited with continuously repeated chirps (2-ms repetition period, frequency sweeping between 500 and 6000 Hz). The resulting wavelength map was compared to the expected values determined from the ultrafast experiment.

3) A slow, diffuse shear wave imaging experiment with 190 frames/sec imaging of low-frequency shear waves (50-500 Hz) to reproduce the low frequency range expected for *in vivo* natural motions.

3.2.7 In vivo experiments on the eye of an anesthetized rat

A preliminary feasibility test was performed on the eye of an anesthetized rat (Long-Evans, Janiver Labs, Le-Genest-Saint-Isle, France). Animal manipulation was approved by the Quinze-Vingts National Ophthalmology Hospital and regional review board (CPP Ile-de-France V). The animal was anesthetized using injections of ketamine (40 mg/kg) and Domitor (0.14 mg/kg). In addition, the eye was locally anesthetized using oxybuprocaine chlorhydarate (1.6 mg/0.4 mL). The animal was positioned so that the eye faced the OCT light beam. Saline drops were periodically administered. Two experiments were performed:

1) An ultrafast active experiment, where the shear wave was induced by a piezoelectric actuator gently placed on the sclera surface and tracked at 76000 lines/sec.

2) A low frame rate, passive experiment, where natural vibrations of the eye (resulting from pulsatile motions) were imaged at 190 frames/sec. Additionally, an ultrafast time-series was acquired (at 76000 lines/sec) at one lateral location of the eye and its Fourier transform was computed in order to determine the spectral content of the natural vibrations.

3.2.8 Results

3.2.8.1 Ex-vivo experiments on a tissue-mimicking phantom

Figure 3.6 shows the shear wave field imaged in an agarose phantom at a sampling rate of either 76000 lines/sec using the ultrafast M-mode (Figure 3.6 a) or 190 frames/sec using the B-mode (Figure 3.6 b). In the ultrafast M-mode, the piezoelectric actuator is placed at the left edge of the imaging plane and the shear wave front can be followed as it propagates from the left to the right. In the low-frame rate B-mode, each frame shows a different realization of the random shear wave field generated by two actuators placed on the sample surface from either side of the imaging area. It should be noted that the measured displacements are differential displacements occurring between two consecutive frames. Thus, the longer the time lapse between two consecutive frames, the higher the displacements magnitude. This is the reason why displacements appear with a higher magnitude in the B-mode case, since the frame period is larger in the low-frame rate B-mode than in the ultrafast M-mode. The shear wave central frequency is 3500 Hz, as estimated by applying a Fourier transform to the displacements recorded in the ultrafast M-mode.

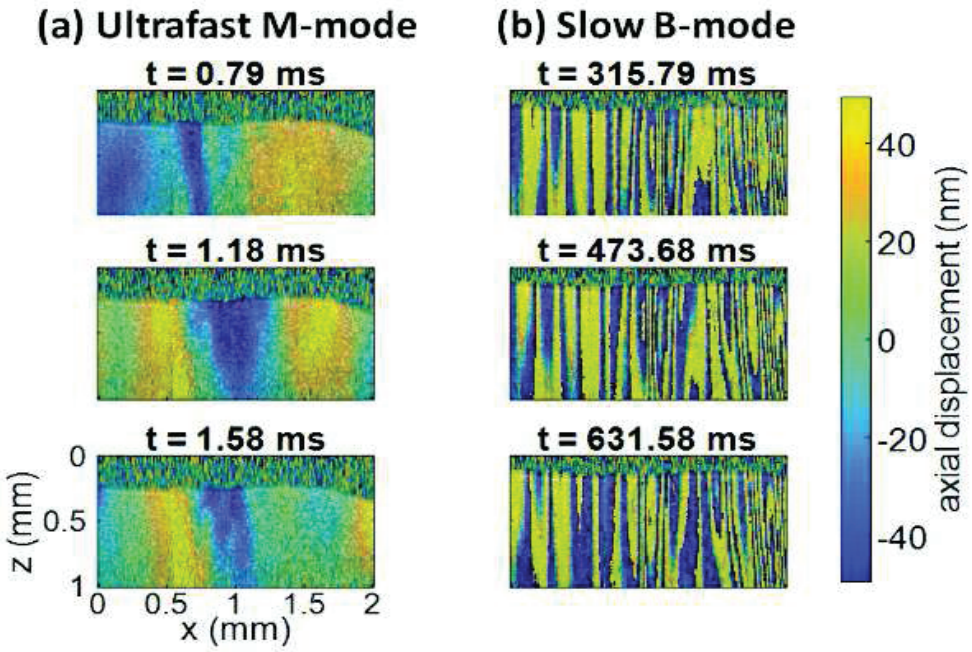

Figure 3.6 – Snapshots of the displacement field recorded in an agarose phantom using either (a) the ultrafast M-mode or (b) the low-frame rate B-mode. The amplitude of the axial displacements (color scale) is overlaid on the morphologic image of the sample (gray scale). In both case, the mechanical stimulation is a 2-ms chirp in the frequency range 500-6000 Hz, synchronized with the acquisition for the M-mode and asynchronously repeated for the B-mode.

3.2.8.2 Characterization of the phantom using ultrafast shear wave imaging

The results of the ultrafast shear wave imaging experiment are summarized in Figure 3.7. The two parts of the sample can hardly be distinguished on the morphologic OCT image. However, the shear wave speed map shows the stiffness contrast between both parts with a clear delineation at the interface. The shear wave speed is 7.5 ± 2.9 m/s in the stiff part and 4.4 ± 2.0 m/s in the soft part (median value ± standard deviation over regions of interest defined from the morphologic image). There is therefore a 1.7-ratio between the shear wave speeds in both parts. Such speed values corresponds to wavelengths values of 2.14 mm and 1.25 mm for respectively the stiff and the soft part, at the central frequency of 3500 Hz (wavelength = speed / frequency). The lateral resolution of the shear wave speed map, defined as the width of the transition zone between both parts, is about 40 µm.

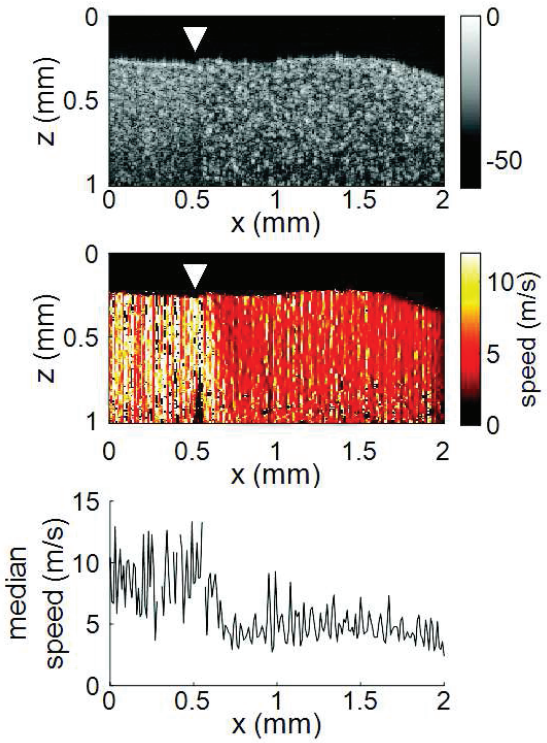

Figure 3.7 – Results of an ultrafast shear wave imaging experiment in an agarose phantom with a broadband, high-frequency shear wave (500-6000 Hz). Top: morphologic image of the phantom. The white arrow indicates the interface between the stiff (left) and the soft (right) parts of the phantom. Middle: shear wave speed map. Bottom: lateral profile of the shear wave speed computed by averaging the speed over a 200-µm depth range.

3.2.9 Shear wavelength tomography using low-frame rate shear wave imaging

Figure 3.8illustrates the concept of shear wave time-reversal using the cross-correlation approach. From the random displacement field presented in Figure 3.6 b, we computed the time-reversed field at two different points of the sample, chosen respectively in the stiff (x1 = 0.4 mm, z1 = 0.55 mm) and the soft (x2 = 1.26 mm, z2 = 0.55 mm) part of the phantom.

Figure 3.8 (a) and (b) show the spatial focusing obtained for each of the two locations at the time t=0 of the cross-correlation. The axial profile of these focal spots, displayed in Figure 3.8 (c), highlight the fact that the focal spot size is bigger in the stiff part than in the soft part.

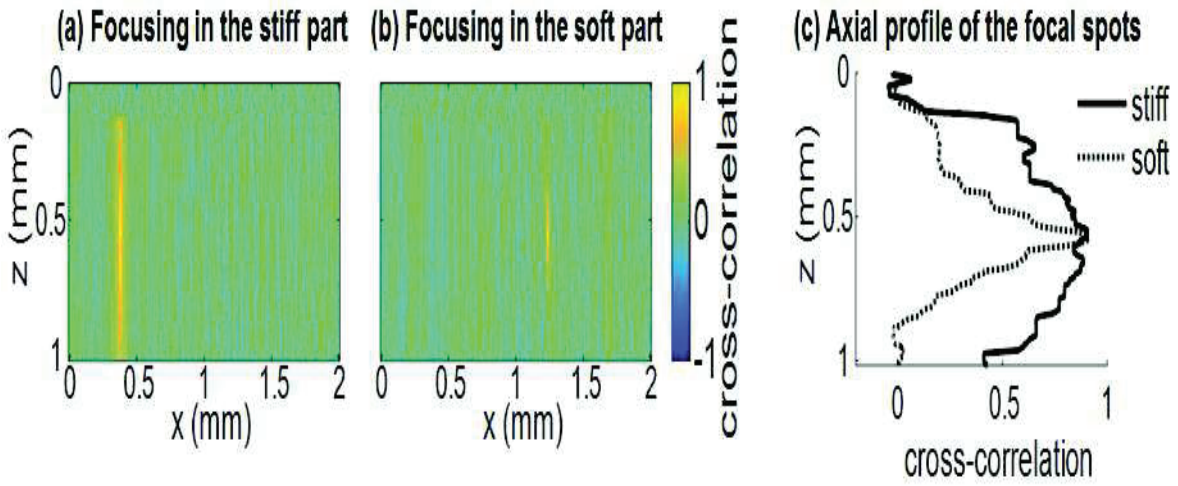

Figure 3.8 – Time-reversed displacement field computed using cross-correlation for two different locations in the phantom. (a) and (b) Focal spots obtained at the two different locations. (c) Depth profile of the focal spot at the two locations (solid line = in the stiff part, dotted line = in the soft part). As expected, the size of the focal spot is larger in the stiff part than in the soft part.

The shear wavelength can be computed at each location of the imaging plane, yielding the wavelength map shown in Figure 3.9. A significant contrast can be observed between the stiff and the soft parts of the phantom. An artifact due to the numerical spatial derivative of the wave field appears at the top of the shear wavelength map. The shear wavelength is 1.64 ± 0.29 mm in the stiff part and 0.98 ± 0.10 mm in the soft part (median value ± standard deviation over regions of interest defined from the morphologic image, excluding the artefact zone). There is therefore a 1.65-ratio between the shear wavelengths in both parts, which is consistent with the speed ratio measured in the ultrafast experiment. The measured wavelengths are of the same order of magnitude as the numbers obtained by converting the speed measurements to wavelengths values considering a central frequency of 3500 Hz for the shear wave field. The variance of the wavelength measurements is lower than the variance of speed measurements, mostly because of a higher signal-to-noise ratio of the recorded displacements due to a higher displacements magnitude. The lateral resolution of the wavelength map, defined as the width of the transition zone between both parts, is about 100 µm.

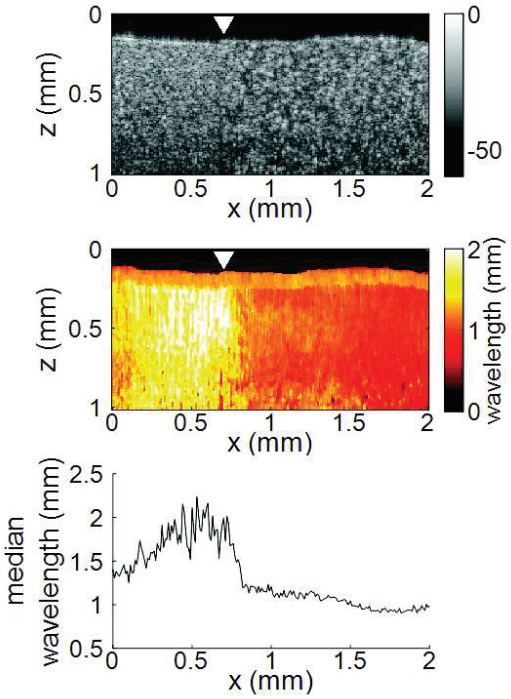

Figure 3.9 – Results of a low-frame rate shear wave imaging experiment in an agarose phantom with a broadband high-frequency shear wave (500-6000 Hz). Top: morphologic image of the phantom. The white arrow indicates the interface between the stiff (left) and the soft (right) parts of the phantom. Middle: shear wavelength map. Bottom: lateral profile of the shear wavelength computed by averaging the wavelength over a 200-µm depth range.

We also assessed the feasibility of the cross-correlation approach with lower shear wave frequencies, since *in vivo* passive elastography will rely on low frequency natural motions (generated by pulsatility). The results obtained with a diffuse shear wave field in the frequency range 50-500 Hz are shown in Figure 3.10. As expected, the shear wavelengths (2.09 ± 0.6 mm in the stiff part and 1.34 ± 0.14 mm in the soft part, median value ± standard deviation) are larger than that obtained with the high-frequency shear wave. The lateral resolution of the wavelength map (210 µm) is also lower than that obtained with the high-frequency shear wave, but both parts can still be clearly identified as having significantly different stiffnesses, with a wavelength ratio of 1.56.

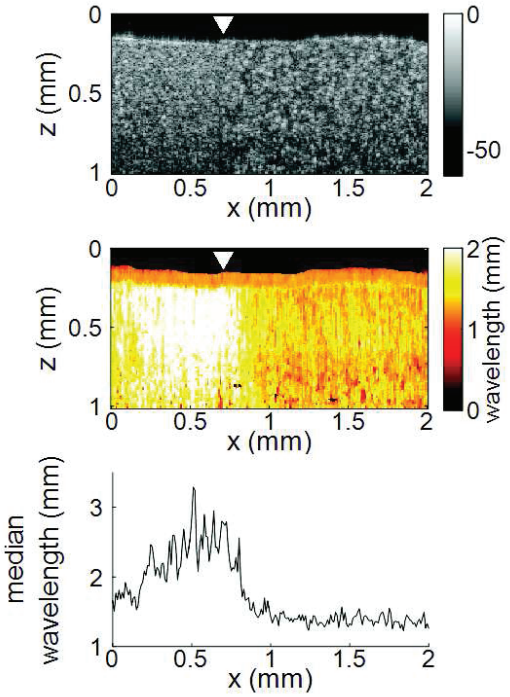

Figure 3.10 - Results of a low-frame rate shear wave imaging experiment in an agarose phantom with a broadband low-frequency shear wave (50-500 Hz). Top: morphologic image of the phantom. The white arrow indicates the interface between the stiff (left) and the soft (right) parts of the phantom. Middle: shear wavelength map. Bottom: lateral profile of the shear wavelength computed by averaging the wavelength over a 200-µm depth range.

3.2.10 In-vivo experiments on the eye of an anesthetized rat

We performed a preliminary *in-vivo* experiment on the eye of an anesthetized rat. On the morphologic OCT image of the anterior segment of the eye (Figure 3.12, left panel), the following ocular tissues can be identified: cornea (co), sclera (sc), iris (ir), crystalline lens surface (le) and choroid (ch). Natural motions in the anterior segment of the rat eye were observed using the low-frame rate B-mode (1.4 sec recording time at 190 frames/sec), as shown in Figure 3.11. These motions are induced by the animal heartbeat (pulsatile motions). The frequency range of the natural motions was estimated to 30 – 150 Hz in the different parts of the anterior segment.

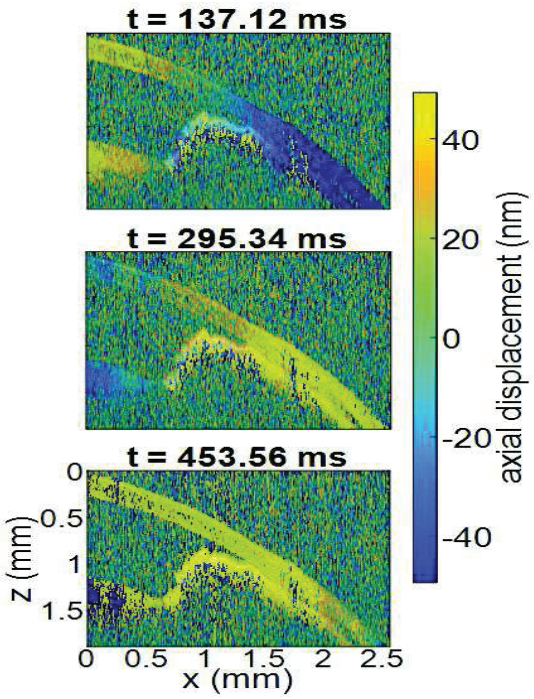

Figure 3.11 – Snapshots of the natural motions recorded in the eye of an anesthetized rat using either the low-frame rate B-mode. The amplitude of the axial displacements (color scale) is overlaid on the morphologic image of the eye (gray scale). The acquisition is completely passive: no active shear sources were used.

The cornea, the sclera, the iris and the choroid are less than 500-µm thick, they are therefore much thinner than the shear wavelength. In such a thin-layer configuration, shear waves are constrained by the layer boundaries and propagate in dispersive guided modes, called Lamb-like modes, which are sensitive to the layers thickness and the shear wave spectral content. Previous studies (Couade et al., 2010; Nguyen et al., 2011) have shown that Lamb-like modes are highly dispersive with a dependence of the Lamb-like wave speed to the wave frequency and the tissue thickness. The apparent speed (phase velocity) is lower than that in a bulk medium of equivalent stiffness (group velocity). In this case, studying the dispersion of the Lamb-like wave propagation is required to quantitatively retrieve the tissue stiffness.

Nonetheless, a wavelength map (Figure 3.12 b) can be reconstructed from the displacement field induced by natural pulsatile motions. On this map, the sclera appears stiffer than the cornea with a clear delineation between both tissues at the limbus; and the choroid appears softer than the cornea and the sclera. The cornea seems to exhibit a stiffer upper layer, which could correspond to the epithelium. Figure 3.12 a) shows a speed map of the Lamb-like waves, which was obtained

by performing an ultrafast active shear wave imaging experiment where a piezoelectric actuator was placed on the sclera (at the right edge of the imaging plane). As the ultrafast active and the passive experiments correspond to displacements with different spectral contents, the speed values obtained from the ultrafast active experiment cannot straightforwardly be compared to the wavelength values obtained from the passive experiments. As explained above, Lamb-like modes tend to propagate with lower apparent speeds (and thus smaller wavelengths) than bulk shear waves. However, the relative stiffnesses of the cornea, the sclera and the iris are consistent for both experiments.

A discrepancy between the ultrafast active and the low-frame rate passive experiments can be observed on the crystalline lens: the shear wavelength seems relatively high in the lens although it is expected to be much softer than other ocular tissues. This could be caused by particular boundary conditions related to the tissues geometry: the crystalline lens, unlike the other ocular structures, is not a thin-layered tissue. It will there not affect the shear wave propagation in the same manner, i.e. it will not generate Lamb-like modes.

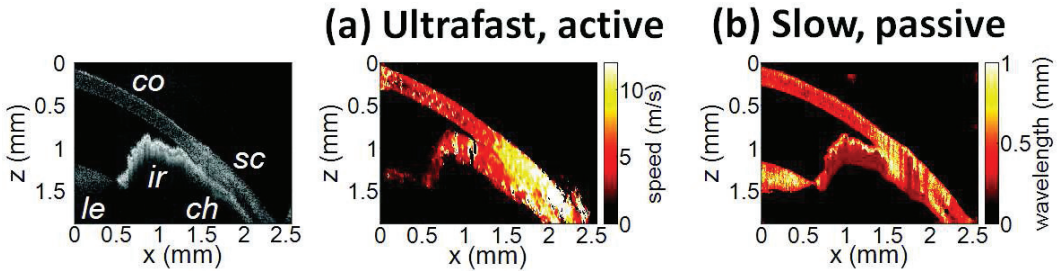

Figure 3.12 – Elastography performed on the eye of an anesthetized rat. Different ocular tissues can be identified on the grayscale morphologic image (left): co = cornea, sc = sclera, le = lens, ir = iris, ch = choroid. (a) Shear wave speed map resulting from an ultrafast active shear wave imaging experiment (ultrafast M-mode). (b) Shear wavelength map resulting from a passive, low-frame rate shear wave imaging experiment (conventional B-mode).

3.2.11 Discussion

Experiments performed on tissue-mimicking phantoms suggest that quantitative stiffness information can be retrieved by imaging a diffuse shear wave field using low-frame rate SD-OCT. We obtained wavelength maps showing a clear contrast between the stiff and the soft parts of a heterogeneous phantom, with a wavelength ratio consistent with the speed ratio measured in ultrafast SWE. For a fair comparison, we generated the same spectral content (500-6000 Hz) in the shear wave field for both the noise-correlation experiment and the ultrafast SWE. However, as natural motions are expected to generate a much lower frequency range, we also performed the noise-correlation with lower shear wave frequencies (50-500 Hz). Consequently, we obtained higher shear wavelengths but a similar wavelength ratio between the stiff and the soft parts of the phantom.

In SWE, the spatial resolution depends on multiple parameters, including the shear wave frequency, the signal-to-noise ratio of the recorded displacements, and the spatio-temporal sampling of the shear wave propagation. In the ultrafast active SWE experiments presented above, we reached a lateral resolution of 40 µm because both the lateral sampling (10-µm pixel size) and the temporal sampling (76000 lines / sec) are high enough to detect shear wave speed changes within 40 µm. In our noise-correlation approach, the spatial resolution is lower mainly because of the lower imaging rate (190 frames / sec). However, we still reach a resolution of hundreds of microns which is much smaller than the millimeter-size shear wavelength.

As a first proof-of-concept for *in-vivo* ophthalmic applications, we performed acquisitions on the eye of an anesthetized rat. Naturally-induced shear waves were observed in the cornea, the sclera, the iris and the lens. Such natural motions do not perturb ultrafast active shear wave imaging, because they occur on longer time scales (hundreds of milliseconds) than the ultrafast recording time (a few milliseconds). A shear wavelength map was reconstructed from the natural diffuse displacements and stiffness differences were observed between the cornea, the sclera and the iris. However, extracting quantitative information requires accounting for the geometry of ocular tissues. Some parts of the eye are thin (hundreds of microns) compared to the shear wavelength (several millimeters) and act as wave guides that constrain the shear wave into Lamb-like modes. In such a configuration, the shear wave propagation speed (and therefore the shear wavelength) depends not only on tissue stiffness but also on tissue thickness and shear wave frequency (Nguyen et al., 2011). For instance, for the first antisymmetric Lamb-wave mode in a layer of thickness h, the propagation speed is $c(f) = \sqrt{2\pi f * h * \sqrt{\mu/(3\rho)}}$, where f is the shear wave

frequency, μ the tissue stiffness and ρ the tissue density. The guidance effect being even stronger at low frequencies, it is essential to account for it for the case of passive elastography, which relies on natural motions (frequencies < 200 Hz). More detailed studies are planned to refine the reconstruction of quantitative elastic maps in such tissues from an analysis of the dispersion curve. Our preliminary results are however encouraging for the development of totally non-invasive stiffness mapping of the eye.

3.2.12 Conclusion

Stiffness information can be retrieved from imaging diffuse shear waves using low-frame rate SD-OCT using a noise-correlation approach. The proof-of-concept was established on tissue-mimicking phantoms and a preliminary *in-vivo* experiment was conducted on the eye of an anesthetized rat. The results open perspectives for *in-vivo* passive elastography using conventional OCT systems. The envisioned biomedical applications include biomechanics studies of ocular tissues and skin layers. For that purpose, further studies will focus on refining the stiffness quantification in thin layered tissue and to expand *in-vivo* measurements.

3.3 Conventional Ultrasound Scanner: HIFU Treatment Monitoring With on Porcine Pancreas with Passive Shear Wave Elastography

To be published in IEEE

3.4 Abstract

We present a passive elastography approach for monitoring the High Intensity Focused Ultrasound (HIFU) treatment. The method consists in retrieving a shear wavelength tomography from the natural vibrations of living tissue. An in-vivo study for characterization of HIFU induced lesions in thirteen healthy porcine pancreases will be presented. Shear wavelength maps are reconstructed before and after the HIFU treatment. The natural shear wave measurement uses a low-frame rate ultrasound scanner and a standard speckle tracking algorithm. Correlation methods first introduced in the field of seismology are the base of the reconstruction.

3.5 Thermal lesion visualization: sate of the art

Earlier studies show that HIFU lesions on porcine liver were visible on the sonogram as hyperechoic areas (Bush et al., 1993). However, the hyper-echogenicity aspect of the lesion is due to the gas bubbles created during the HIFU treatment, these bubbles are not representative of the lesion extent. Based on our experience, the HIFU lesion on porcine pancreatic tissue remains invisible on the sonograms after the dissipation of the bubbles cloud.

Magnetic Resonance Elastography (MRE) was also used to assess the thermal effect on the mechanical properties of the tissue (Wu et al., 2001), but the MRI experimental setup cost and complexity may restrict the establishment of this technique. In contrary, fully ultrasound based methods are easily integrated into a HIFU set-up with a relatively low coast and a high portability. The possibility to use the variation of the mechanical properties in order to monitor HIFU treatment was demonstrated using strain imaging Elastography (Shi et al., 1999; Souchon et al., 2003). In the other hand, transient Elastography techniques based on the measurement of the shear wave speed, provides quantitative measurement of the elastic properties changes (Benech and Negreira, 2010; Arnal et al., 2011).

The visualization of the HIFU lesion in pancreatic tissue is not possible with standard sonogram (B-mode echography). Unlike in the liver, the complexity of the pancreatic tissue prevents imaging of the induced lesion with B-mode. Thus, in this study passive shear wave elastography

using a low frame rate scanner will be used to monitor the High Intensity Focused Ultrasound (HIFU) induced lesions in porcine pancreatic tissue. But, first we will show the feasibility to passively asses shear wavelength tomography with a low frame rate ultrasound scanner in a calibrated tissue mimicking phantom.

3.6 Tissue mimicking phantom experiments

The feasibility experiment was conducted on a tissue mimicking phantom CIRS® (model 049) containing four spherical inclusions, 10 mm diameter with a Young modulus ranging from 8 to 80 KPa, and 25 KPa in the background. Compared to similar experiment presented by Catheline et al. (Catheline et al., 2013), the finger impacts were replaced by electromagnetic shakers to better control the frequency content of the elastic wave field. The shear wave field is created with three asynchronous electromagnetic shakers (RS 4 cm Slimline Speaker Driver 628-4658, 8Ω, 1w) (fig 3.13. Top), positioned randomly on the surface of the phantom and connected to a signal generator (Tektronix®, AFG 3022B). No synchronization between the shear wave sources and the scanner is needed. The excitation signal was a 1 second duration sweep with a frequency ranging from 50 to 500 Hz, repeated 12 times during 12 seconds.

A linear (192 channels) ultrasonic probe working at a central frequency of 12 MHz and 0.183 mm pitch was connected to a commercially available ultrasonic scanner (HAWK 2120 EXL, B&K Medical, Herlev, Denmark). The system was slightly modified in order to allow saving the output analogue radio-frequency (RF) echo signal in the memory of the host computer. The scanner provides 25 frames / second, with a penetration depth between 3 and 4.5 cm. A data set of three hundreds of RF frames acquired at frame rate of 25 frames / seconds was saved in the memory of the host computer.

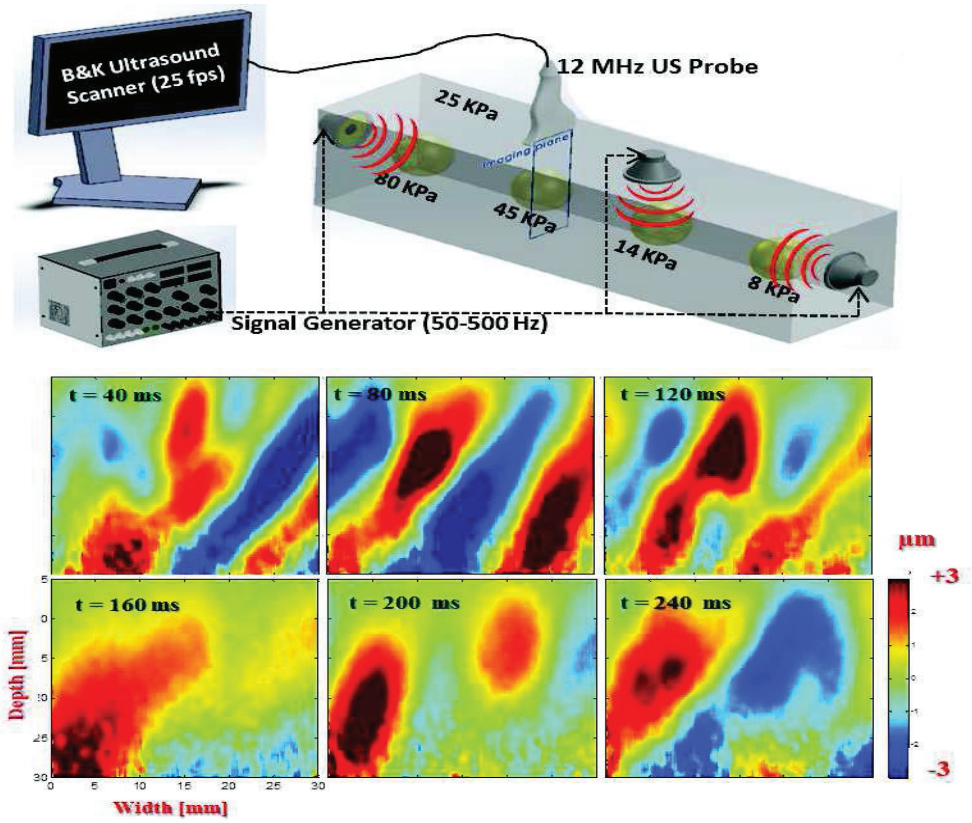

Figure 3.13 Top: Phantom Experimental Setup in calibrated CIRS® Elastography phantom. Multiple magnetic shakers are placed randomly on the surface of the phantom and acts as an asynchronous shear wave sources. The excitation signal is 1 second modulated sinusoid, with a frequency band ranging from 50 to 500 Hz. The 12 MHz imaging probe was connected to an ultrasound scanner working at a frame rate of 25 fps. Bottom: Axial displacement field measured inside the sample. The first six snapshots were extracted from a 300 frames movie. The amplitude of the displacement was $\pm 3\mu m$.

The 2D displacement field along the direction of propagation of the ultrasonic beam is measured inside the sample (fig 3.13. bottom) with a standard speckle tracking algorithm. Different wavelength can be observed in this snapshots, which correspond to the frequency band 50 – 500 Hz of the excitation signal. The amplitude of the particle displacement $\phi_z(x,z,t)$ is ranging between ± 3 µm.

The locale shear wavelength maps were computed according to Equation 2.8 (cf. section N°2.3). The spherical inclusions 80 KPa and 14 KPa are perfectly visible on (Fig 3.14), the measured mean shear wavelengths are respectively 6.1 cm and 2.6 for the inclusions and 3.2 cm in the background. In an elastic, homogenous and isotropic medium, the group (or mean) shear

wavelength can be computed theoretically as $\lambda_s = \sqrt{E/3\rho f_0^2}$. E is the Young's modulus, ρ the density of the phantom 1 Kg.L^{-1}, and f_0 = 80 Hz is the central frequency of the vibration measured inside the phantom. Based on this relation and the Young's modulus provided by the manufacturer, the expected shear wavelengths are 6.5 cm, 2.7 for the inclusions and 3.6 cm for the background. These theoretical values are in agreement with our measurement.

As mentioned before, this correlation based technique is more reliable in an ideal diffuse wave field. Except, in this experiment the shakers were placed on the surface of the phantom, therefore, the generated shear wave field is highly directional, and not equipartitioned. Thus, the non-ideal wave field happens to be the reason for the fluctuation in the shear wavelengths maps (Fig.3.14). A bias on the wavelength value can be observed on the top and the bottom, the low measured value on the top are due to the constraint applied by the imaging probe on the phantom that prevent displacement on the surface of the phantom. On the bottom the bias is due to a low signal to noise ratio.

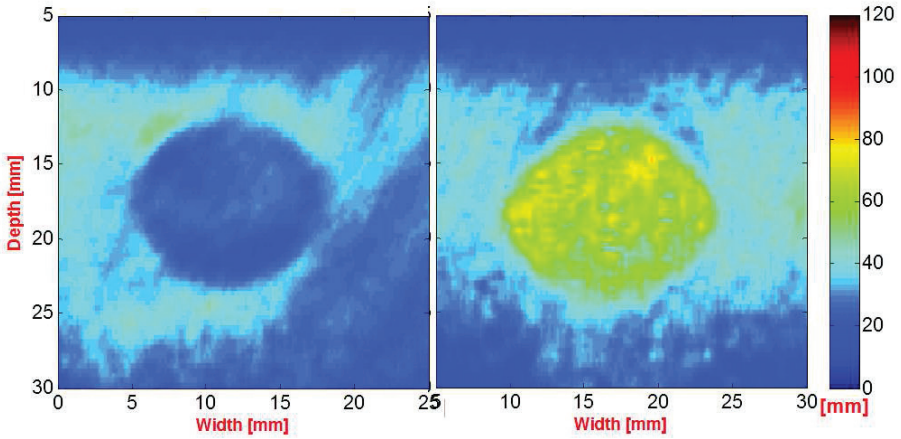

Figure 3.14 - Phantom Shear Wavelength Tomography; the measured shear wavelengths are 26 mm for the soft inclusion (left) and 61 mm for the stiff inclusion (right).

The phantom experiments demonstrate the feasibility of passive elastography to measure the local shear wavelength with a low frame rate scanner. The variation of the local shear wave length is proportional to the local elasticity. Now, this passive approach will be tested in-vivo to monitor elasticity changes induced by HIFU treatment on porcine pancreas.

3.7 HIFU experimental setup

High Intensity Focused Ultrasound (HIFU) is a well-developed technique to locally destroy cancerous tissue. The focused ultrasonic bean can increase the temperature of the tissue in the focal spot to 70-90° in a few seconds. This temperature elevation destroys irreversibly the cells by coagulative necrosis effect. The therapeutic efficacy of HIFU treatment have been approved in a wide range of clinical applications (Kinsey et al., 2008; Melodelima et al., 2008; Wu et al., 2007), especially for the treatment of prostate cancer (Crouzet et al., 2014; Poissonnier et al., 2007; Uchida et al., 2012).

In this study, the HIFU (High Intensity Focused Ultrasound) lesions were created by a toroidal transducer (Imasonic, Voray-sur-l'Ognon, France) developed for intra-operative treatment (Fig 3.15. a), with an operating frequency of 2.5 MHz. In order to localize the area to be treated (Fig 3.15 d), the center of the HIFU transducer (Fig 3.15 b) was equipped by a 7.5 MHz central frequency ultrasound imaging probe (Vermon, Tours, France) connected to a B&K HAWK 2120 EXL conventional ultrasound system (B&K Medical, Herlev, Denmark). Note that, because of the bad quality of the B-mode images provided by the imaging probe of the HIFU transducer, another probe was used to perform the Elastography measurement. As consequence a miss matching between the treated regions and elastography images was possible. This flaw will be corrected in future experiments, but unfortunately it impacts the results presented in this manuscript.

The HIFU parameters were designed to treat a 20 cm^3 of pancreatic tissues in 160 seconds with an acoustic power of 10W at a temperature between 80 and 120°C. The size of the lesion measured In-vitro 18.3 ± 1.1 mm in diameter and 17.0 ± 1.2 mm in depth (Fig 3.15 c) (Vincenot et al., 2016).

In this study, in-vivo experiments were conducted on thirteen healthy porcine pancreases. Experiments were carried out in agreement with the approved guidelines and approved by the ethical committee of Centre Léon Bérard (Ref: COM078v2B, N°10). Note that the experiments were optimized in order to: first, maximize the measurements (HIFU treatment, Elastography measurement, test of pancreatic secretion drainage probe, in-vitro lesions size measurement, histological measurements) and second to minimize the animals suffering.

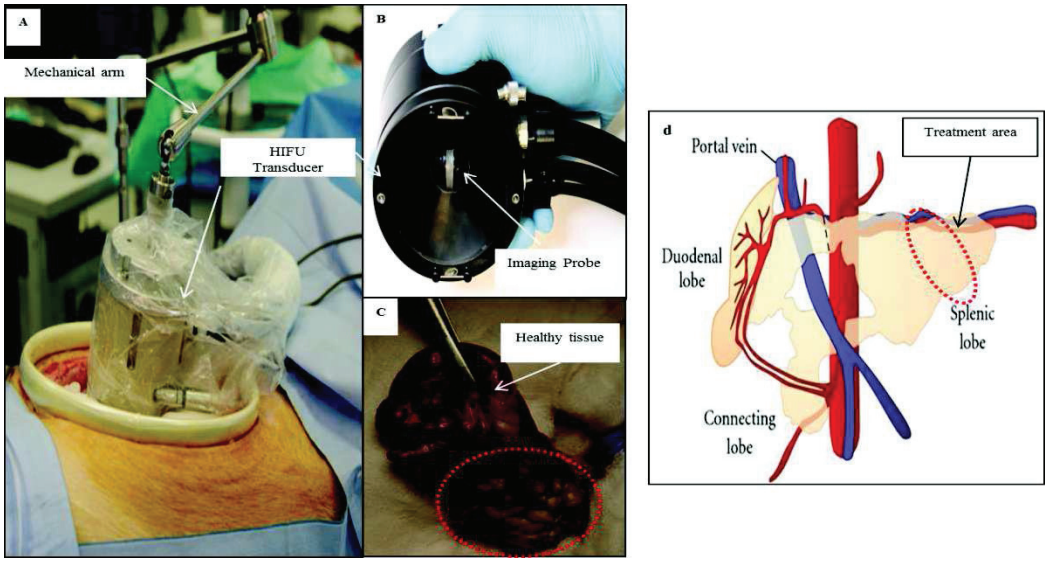

Figure 3.15 HIFU Setup; (a) The HIFU transducer sterilized and placed on the top of pig's pancreas and maintained by a mechanical arm. (b) Picture of the toroidal HIFU transducer equipped by an ultrasound imaging probe in the center. (c) Picture of treated pancreatic tissue (red dotted circle) and healthy tissue. (d) The anatomy of the porcine pancreas, the area to be treated is surrounded by red dotted lines.

The experiment took place in three steps:

Step 1, Pre-HIFU Elastography measurement: A representative area of the pancreas was chosen by the surgeon, and the ultrasonic probe was free hand positioned. To perform sonograms with a suitable quality, instead of using the imaging probe of the HIFU transducer, the same imaging system as in the phantom experiment was used. The time duration of the in-vivo experiment was 30 seconds at a frame rate of 25 frames / second, RF frames were stored in the host computer. Under the hypothesis that a healthy pancreas has a uniform elasticity, the chosen area to perform the Pre-HIFU Elastography measurement was not necessarily the area to be treated after.

Step 2, HIFU treatment: The ultrasonic probe was removed and the HIFU transducer was positioned on top of the pancreas (Fig 3.15 a). The positioning is guided by the integrated ultrasonic probe (Fig 3.15 b). Then, the transduced was handled by a mechanical arm to avoid any undesirable movement during the 160 seconds of treatment. The nearby organs were protected from the HIFU beams by sterile compress.

Step 3, Post-HIFU Elastography measurement: The HIFU transducer was removed, and the step 2 was repeated. As mentioned in the introduction, in the case of pancreatic tissue, the treated

area is not visible on the B-mode image (Fig 3.16). In order to perform Elastography measurement in the treated area, the surgeon feels the elasticity variation with his fingers, and then the ultrasonic probe was positioned in order to get in the same image, treated and healthy tissue. In a few cases (e.g. Pig N°2), the lesions were visible by eye inspection on the surface of the pancreas (Fig 3.15 c), therefore, the probe was directly positioned in this area.

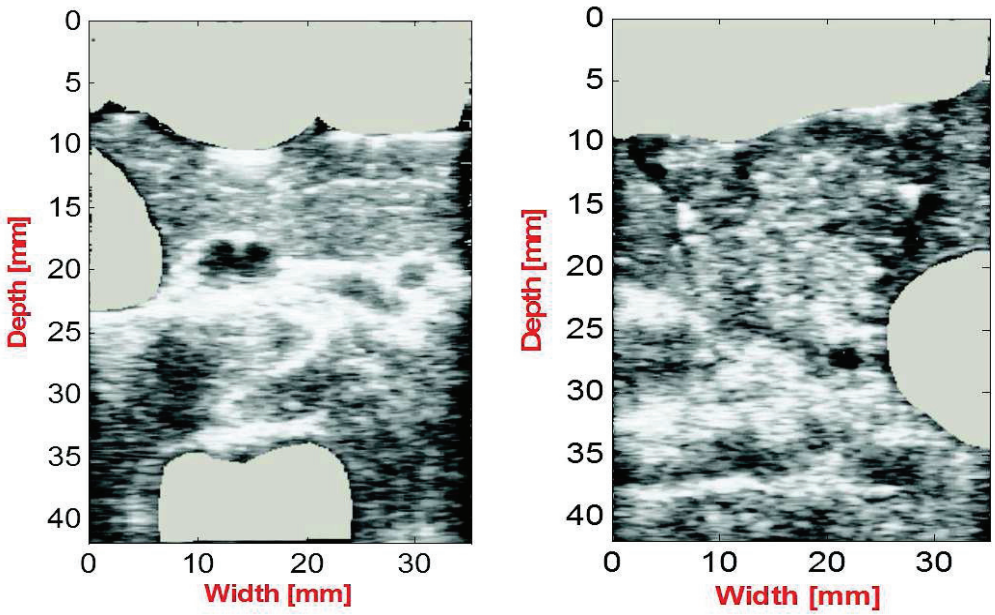

Figure 3.16. left) B-mode image before HIFU treatment. Right) B-mode image after HIFU treatment. The treated area is not visible on the standard B-mode image after the HIFU treatment.

Finally, 1D speckle tracking algorithm (cf. section 1.2.3.1) was used to compute the natural displacement field in the pancreas (Fig 3.17), the gray colored region are due to a bad signal to noise ratio (SNR), or the region of the veins and arteries for example. The amplitude of the natural displacement is about 40 µm, multiple wave fronts can be observed in different snapshots, which confirms of the presence of diffuse shear wave field.

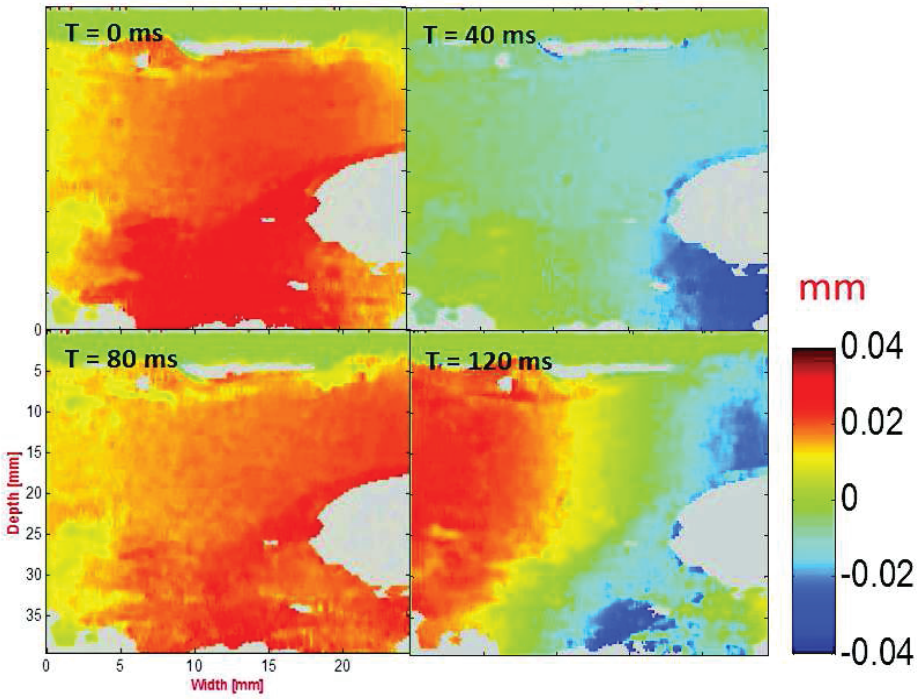

Figure 3.17. Naturally induced displacement field inside the pancreas. Four snapshots were extracted from à 800 frames movie. These in-vivo measurements were acquired with an ultrasound scanner at a frame rate of 25 fps. The areas with a low signal to noise ratio were colored in gray.

3.8 Results and Discussion

For each pig two wavelength maps were computed: Pre-HIFU treatment and Post-HIFU treatment respectively Fig 3.18. top and Figs 3.18. bottom. The measured mean wavelength value over all the treated pigs was respectively 31±3,2 mm and 51,6 ±4.8 mm. An elevation of the wavelength value was systematically observed in 80% of the treated pigs, which confirms the stiffening of the treated tissue as expected. The size of lesion measured on the wavelength maps was in agreement with the in-vitro measurement performed after the euthanasia of the pigs under the ethical considerations.

A mode systematic study could be realized when the quality of the B-mode images proved by the imaging probe of the HIFU transducer will be improved. Thus, it prevent from the miss matching between the treated region and elastography measurement.

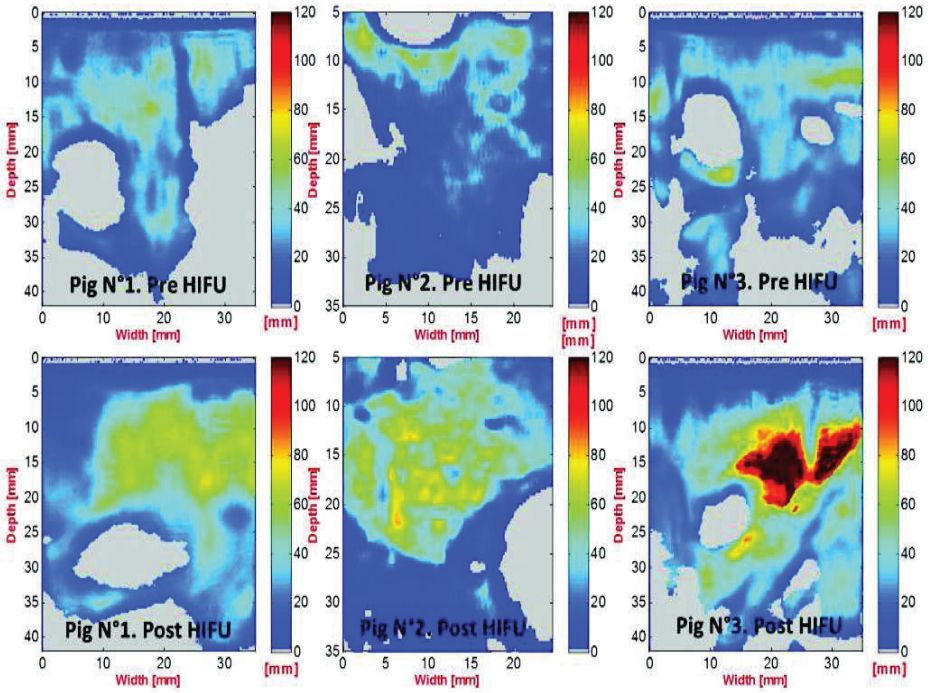

Figure 3.18. In-Vivo Shear Wavelength Tomography; Top: Pre-HIFU treatment for 3 pigs, the measured mean shear wavelength value is 31 ± 3.23 mm. Bottom: the corresponding Post-HIFU treatment, the he measured mean shear wavelength value is 51.6 ± 4.8 mm. The elevation of the shear wavelength is due to the stiffness variation after the HIFU treatment.

Nevertheless, in this study, it has been demonstrated for the first time the ability of passive Elastography to localize the HIFU lesions in pancreatic tissue. Because of experimental constraint, the elastographic measurements were not performed in real time, the improvement of the B-mode quality of the HIFU transducer probe should solve this problem. Passive Elastography approach might open a way to HIFU treatment monitoring with slow imaging scanners such as Magnetic Resonance Imaging (MRI) or conventionally ultrasound scanner. In addition to that, this passive approach is very easy to implement in such a study and does not change much the usual practices in surgery. In the other hand, reducing the experiment duration (i.e. 30 seconds in this study) will be very suitable in this kind of clinical applications. Ultrafast ultrasound scanner becomes to be widely used in clinical studies, its offers the possibility to measure quantitatively the shear wave speed and to give a quantitative elasticity map in real time.

4 Passive Elastography Using High Frame Rate Scanners

Shear wave speed Tomography

In the previous studies we have shown the possibility to conduct a passive shear wavelength tomography with a conventional (low frame rate) scanner. However, with an ultrafast scanner the temporal information is available in the recorded data. Thus, quantitative measurement of the shear wave speed can be performed. Therefore, under the hypothesis of homogenous, isotropic, infinite and linear propagation medium, the shear modulus and the Young's modulus can be deduced. Nowadays, ultrafast scanners are spreading all over the world and will, soon or later, replace conventional scanners. They, allows to reach a very high frame rate (more than 8000 frames / second) and offer an outstanding imaging quality. In this chapter two studies have been realized using two ultrafast imaging systems: the first one is an ultrasound scanner whereas the second one is an ultrafast optical camera. The aim of the first experiment is to test the quantitative shear wave speed measurements using a novel correlation-based inverse problem. The second sets of experiments are devoted to the proof of the concept of an optical tracking method for surface waves.

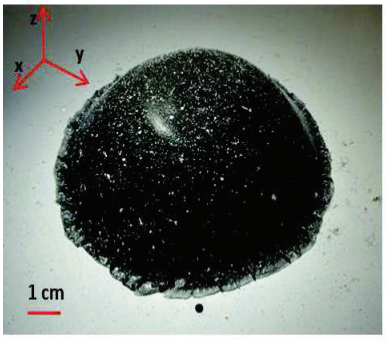

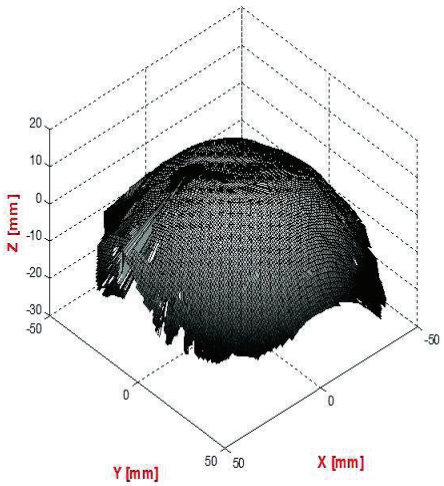

4.1 Passive Shear Wave Speed Tomography with an Ultrafast Ultrasound Scanner

As introduced in section chapter 2, the local shear wave speed can be estimated trough equation 2.7 from a simulated diffuse wave field. The feasibility of this approach has been experimentally demonstrated in the case of a low frame rate scanner. This part will be dedicated to demonstrate the relevance of this approach with an ultrafast ultrasound scanner. The first experiment was conducted on calibrated tissue mimicking phantom (CIRS® 049). The diffuse shear wave field was created with multiple asynchronous mechanical vibrators. The shear wave speed maps on the phantom show clearly the soft and the stiff inclusion. The measured shear wave speed values with the passive approach were compared with the Aixplorer® results as a gold standard method. Second, in-vivo experiment was conducted on a healthy volunteer liver. The aim of this experiment was to demonstrate the feasibility to passively reconstruct quantitative shear wave speed map from naturally induced shear (physiological) wave field.

4.1.1 Tissue Mimicking Phantom Experiment

The first experiments were conducted on a tissue mimicking phantom CIRS® (model 049) containing four spherical inclusions with 20 mm diameter. The manufacturer provides a Young's modulus for each inclusion: 80 kPa and 45 kPa for the stiff inclusions compared to the surrounding phantom 25 kPa, and 14 kPa, 8 kPa for the soft inclusions. In this experiment an ultrafast ultrasound scanner was used (Vantage® Verasonics Inc., Redmond, WA, USA). A 128 channels linear ultrasonic array (Philips® L7-4) operating at 5 MHz central frequency was connected to the scanner. The diffuse shear wave field was induced mechanically with a multiple non-synchronized shakers (RS 4 cm Slimline Speaker Driver 628-4658, 8Ω, 1w) randomly positioned at the surface of the phantom (Fig 4.1 top). The shakers were connected to a signal generator (Tektronix®, AFG 3022B).The generated source signal is a sweep with frequency band ranging from 50 to 500 Hz with 700ms duration, amplified by a two channels audio amplifier (Audiophonics T20 V2.2). In order to properly sample the induced displacement field, the frame rate was set at 1000 frames / second. The acquisition duration was one second.

The acquired radio-frequency (RF) images were saved in the memory of the host computer. The induced displacement field (Fig4.1 bottom) was computed with the speckle tracking technique. The amplitude of the displacement was ranging between $\pm$ 10µm. The red wave fronts (negative) are the displacement in the direction of the probe and the blue one (positive) are in the opposite

direction. The multiple small vibrators create a diffuse shear wave field that can be observed as a random fluctuation coming from different sides of the imaging plane (Fig4.1 bottom).

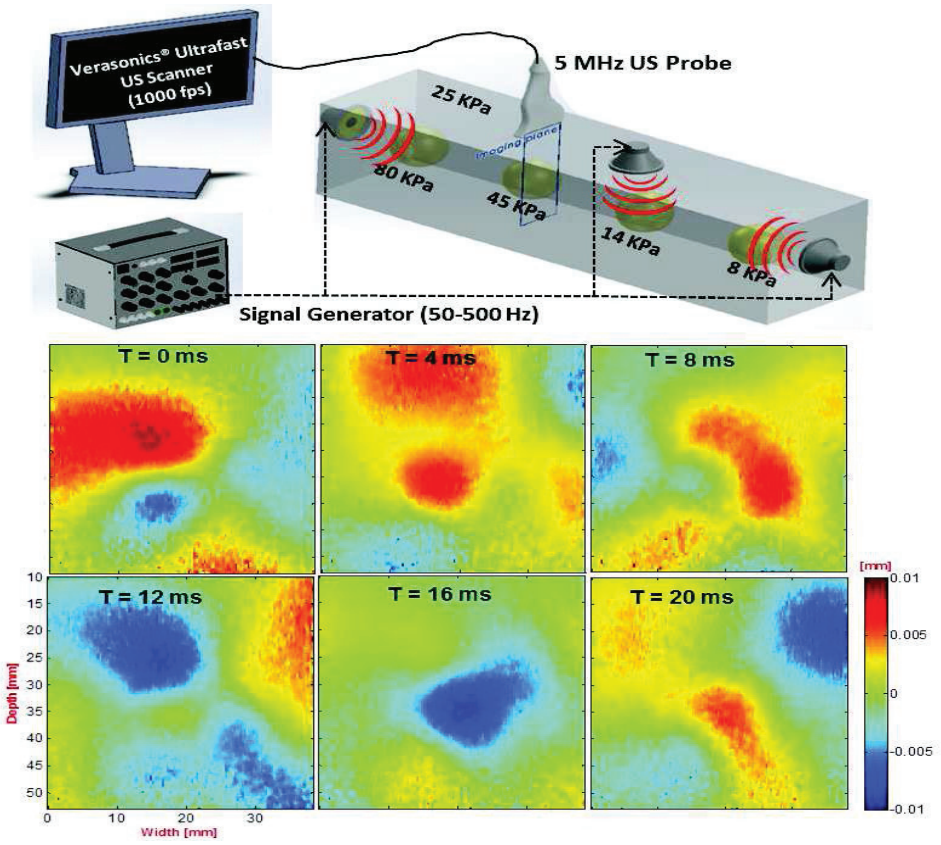

Figure 4.1. Top: A 5 MHz linear ultrasonic probe is connected to an ultrafast ultrasound scanner (Vantage, Verasonics®) that acquired 1000 frames/ second. Shear waves are generated by small vibrator inside a tissue mimicking phantom (CIRS® model 049). The source signal is a sweep with frequency ranging from 50 to 500 Hz. Bottom: six snapshots from a displacement movie of 1000 frames. In order to observe a significant changing in the displacement the snapshots are spaced by 4 ms. The amplitude of the displacement is ranging between ± 10 μm. Different wave fronts can be observed due to the diffuse aspect of the generated shear wave field.

The local shear wave C_s speed is measured through equation 2.7. The reconstructed passive shear wave speed maps of the soft inclusion (14 kPa) and stiff inclusion (80 kPa) are presented in (Figure 4.2). The average values of the measured shear wave speeds (median value ± standard deviation over regions of interest) are summarized in table 4.1. According to the relation between the Young's modulus and the shear wave speed $E = 3\rho C_s^2$, the theoretical shear wave speeds are supposed to be: 5.16 m/s, 2.16 m/s and 2.88 m/s for respectively the stiff inclusion, the soft inclusion and the background.

	Stiff Inclusion (m/s)	Soft Inclusion (m/s)	Background (m/s)
Manufacturer	5.16	2.16	2,88
Aixplorer®	5.27 ± 1.93	2.02 ± 0.44	2.63 ± 0.69
Passive Elastography	4.39 ± 0.98	2.76 ± 0.89	2.87 ± 0.83

Table 4.1. Summary of the shear wave speed values measured with passive elastography, Aixplorer and the theoretical value provided by the manufacturer of the calibrated phantom CIRS® 049.

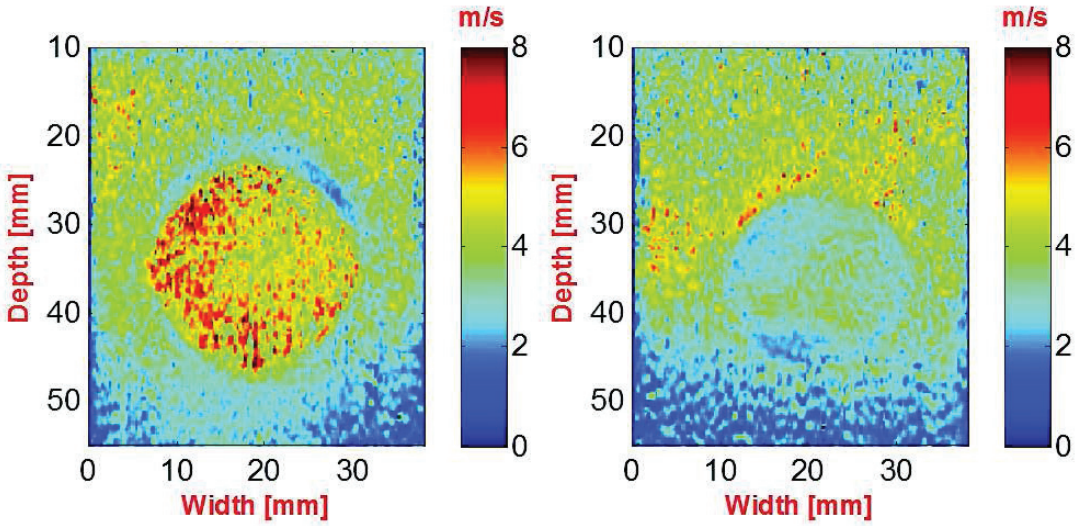

Figure 4.2. passive shear wave velocity map: left) stiff inclusion, the mean velocity value is 4.39 m/s ± 0.98. Right) soft inclusion, the mean velocity value is 2.87 m/s ± 0.38. The measured mean shear wave velocity value in the background is 2.76 m/s ± 0.89.

A comparative experiment was performed on the same phantom using the supersonic imaging (SSI) as a gold standard method. The aim of this comparative study is to validate the shear wave speed measurement obtained by the passive elastography approach. However, because of difference between the ultrasonics frequencies of the probes (i.e. 5 MHz for passive experiment and 10 MHz for the Aixplorer) the comparison in terms of the penetration depth of ultrasound is note possible in this case. The figure 4.3 shows the elasticity maps provider by the scanner in the stiff and the soft inclusion respectively left and right. The measured Young's modulus are converted to shear wave speed through the relation ($E = 3\rho C_s^2$) and summarized in table 4.1.

Table 4.1 shows that the shear wave speed values measured with passive elastography approach are in agreement with the measurement proved by the Aixplorer especially in the background where the error dos not exceed 9%. However, the difference between the mean values measured in the inclusions is higher between the two techniques, 27% and 17% for respectively the soft and the stiff inclusion. This is may be due to the ageing of the phantom. Indeed, the theoretical shear wave speed computed from the Young's modulus provided by the manufacturer is between the two measurements. Passive elastography is 15% below the theoretical value and the Aixplorer® is only 3% above the manufacturer value. Nevertheless, the standard deviation provided by each measurement is relatively high (i.e. ±0.93 m/s for passive elastography and ±1.93m/s for the Aixplorer®). Thus, the measurement still can be considered in agreement with the theoretical value.

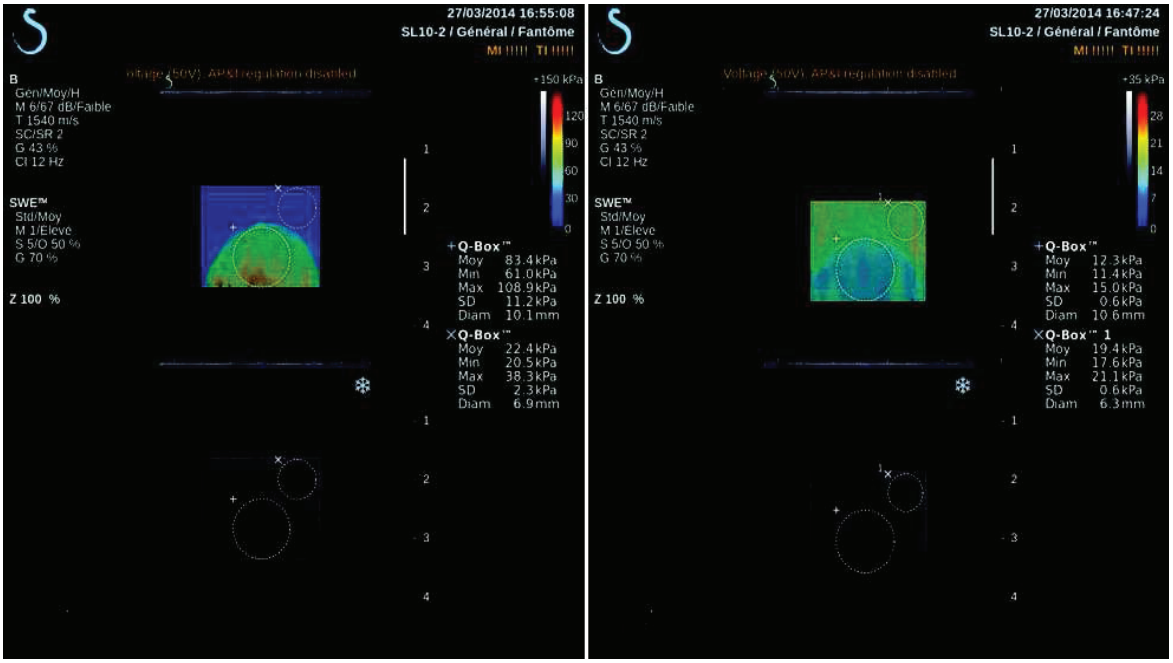

Figure 4.3. Elasticity maps provided by the Aixplorer® in the CIRS® phantom. Left) The elasticity map measured inside the stiff inclusion, the Young's modulus is 83.4 ± 11.2 Kpa. Right) the elasticity map measured for the soft inclusion, the Young's modulus is 12.3 ± 0.6 Kpa. The Young's modulus measured in the surrounding phantom is 19.4 ± 0.6 Kpa.

4.1.2 In-vivo Experiment on the Liver of a Healthy Volunteer

Actually two ultrasonic scanners that provides 2D elasticity maps in real time are commercially available (1) the Aixplorer® from Supersonic Imagin Inc (2) the Virtual Touch™ Quantification from Siemens Inc. Although efficient, their main limitation is the penetration depth of ultrasound to generate shear waves by the radiation pressure in deep organs. The mechanical index (MI) defined by the FDA (Food and Drug Administration) is also a limitation of radiation force based methods for the application in the sensitive organs such as the cornea. The objective of passive elastography is to tack advantage of the naturally induced shear wave in the human body. Thus, it is not limited by the penetration depth of ultrasound and the MI limitation is only for imaging. The only need is a sufficient back scattered signal from the deep organs. In other word, as far as it is possible to perform several images in the human body, it should be possible to reconstruct elasticity maps. In the first part we have shown the feasibility to passively retrieve quantitative shear wave velocity maps in a calibrated phantom. This part is then dedicated to the use of physiological noise in order to construct passive shear wave velocity map in the liver.

The liver has been chosen because it is easily accessible by ultrasonic scanner, and its elasticity is well documented in the literature. Previous clinical studies shows the possibility to detect the different stages of liver fibrosis as function of their elasticity (Sandrin et al., 2003; Bavu et al., 2011; Woo et al., 2015). Those studies show also that for a healthy volunteer the measured shear wave speed is around 1 m/s a 50 Hz. In our study, the experiments were conducted on the liver of a 26 year old healthy volunteer.

The liver is a big organ located in the upper right quadrant of the abdomen, below the diaphragm. It can be visualized by ultrasound by positioning the ultrasonic probe in the upped side of the diaphragm under the last rib (Fig 4.4 left). First the probe is positioned by displaying the B-mode image in real time. To avoid blurring the final shear wave speed reconstruction it is important to acquire the hundreds of images from the same region of interest within the organ. Therefore, once the probe positioned the subject has to stop breathing in order to avoid undesirable global breathing motion during the one second acquisition.

The experimental setup is the same as in the phantom experiment, except for the shear waves generation. The shear waves are naturally created, in the liver mainly due to the heart beating. However, the reverberation and the secondary sources along the arterial system increase the complexity of the shear wave field. Note that with passive elastography there is no need to synchronize the scanner with the heart beating. Since the frequency content in-vivo is lower than

in the phantom experiment (i.e. from 5 to 60 Hz), the imaging frame rate is set at 300 frames / second in order to maximize the sensitivity to the motion. The induced displacements on the direction of the ultrasonic beam are measured with the speckle tracking algorithm (Fig 4.4 right). The amplitude of the displacement is similar to the amplitude estimated from the phantom experiment ($\pm$ 10 µm).

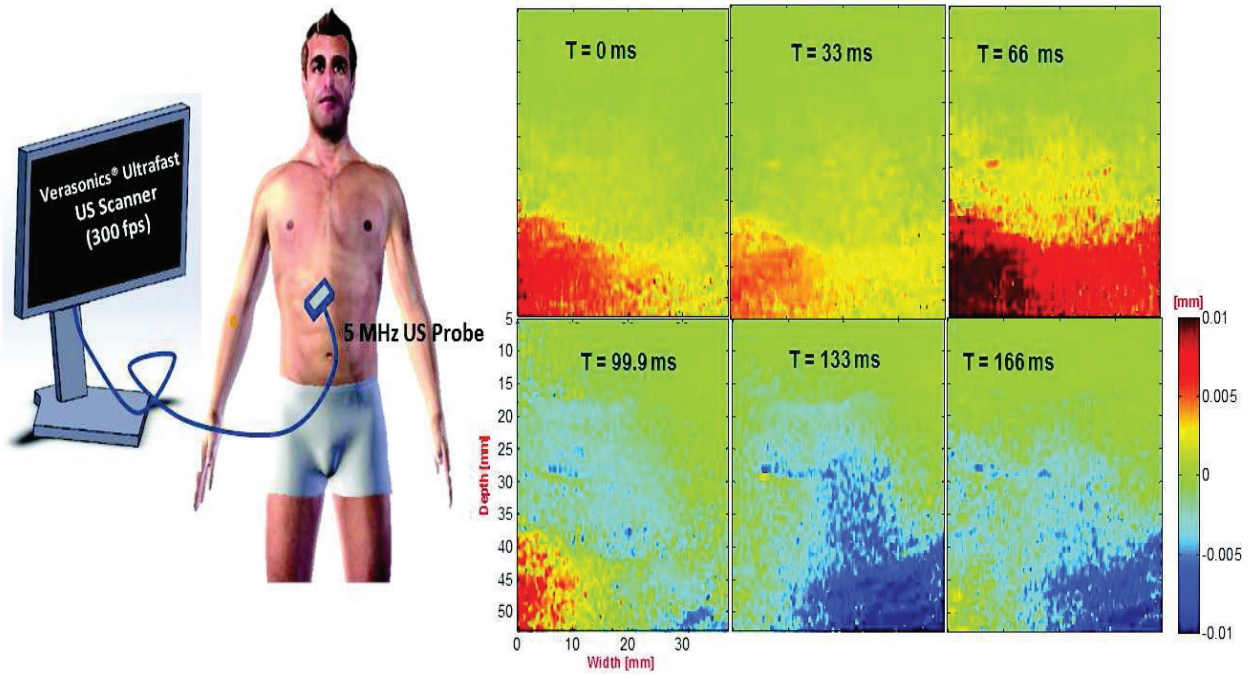

Figure 4.4. left) the ultrasonic 5 MHz probe is connected to an ultrafast scanner (Verasonics Vnatage ®) and positioned in order to image the liver. The frame rate is fixed to 300 frames / second, and the acquisition duration was 1 second. Right) six snapshots from a 300 frames displacement field are presented. The amplitude of the displacement is $\pm$ 10 μm, and the central frequency in rest state is around 25 Hz.

The B-mode image (Fig 4.5 left) shows the liver as a darker region (red dotted line), the abdominal muscle and the stomach wall. The measured mean value of the passive shear wave velocity is 0.98 $\pm$ 0.5 m/s is in agreemnt with the shear wave speed value found in the literature for a healthy volunteer. By magnetic resonance, Huwart and al. measured a shear wave speed of 0.86 $\pm$0.21 m/s for a frequency of 65 Hz (Huwart et al., 2006). The supersonic shear imaging technique gives a shear wave speed of 1.18 $\pm$ 0.18 ms at a frequency of 50 Hz (Muller et al., 2009). The Fibroscan® wich is the gold standard in the diagnostic of liver fibrosis gives a global shear wave speed value of 1.06 m/s at 50 Hz (Sandrin et al., 2003).

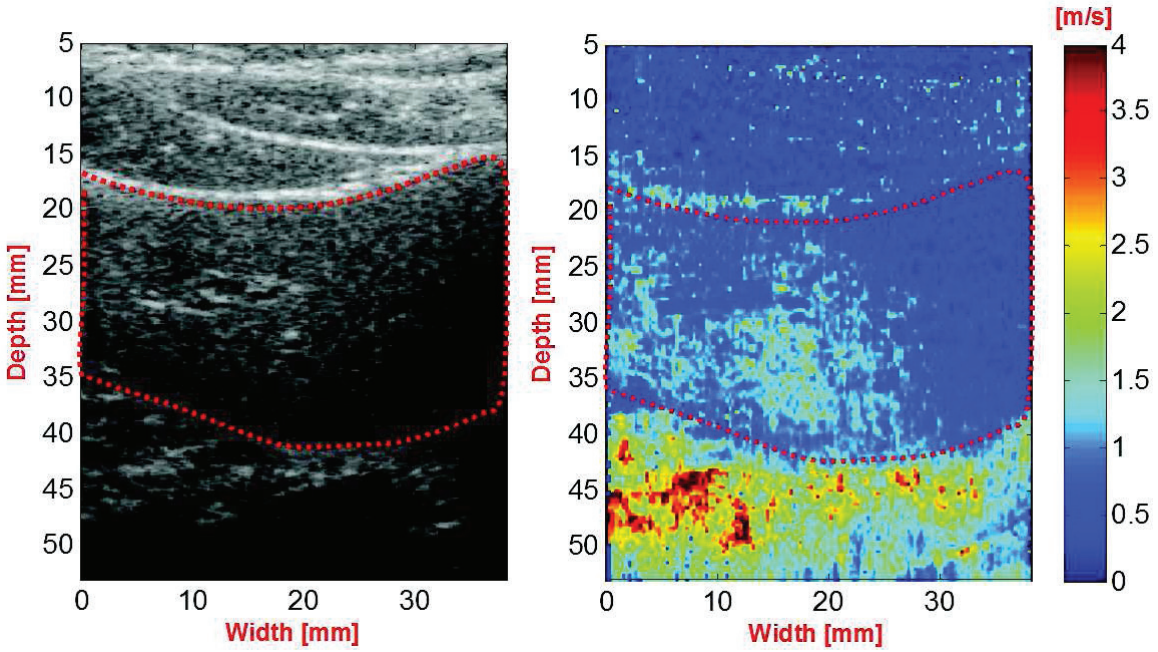

Figure 4.5. The B-mode image (left) shows: the abdominal muscle and fat (from 5 mm to 15 mm). The liver region (red dotted line from 15 mm to 35 mm) and the stomach wall (from 35 mm to 55 mm). Passive shear wave velocity map (right), the measured shear wave velocity is 0.98 m/s ± 0.5.

4.1.3 Discussion

This first experiment conducted in a calibrated tissue mimicking phantom, shows the ability of our algorithm the retrieve quantitative shear wave speed maps from a diffuse wave field. The obtained maps show a clear contrast between the surrounding phantom and both the stiff and the soft inclusions. The measured shear wave speed values are in agreement with the measurements provided by the Aixplorer® as a gold standard method. The passive shear wave speed map shows a lower value in the bottom. This is due to the low signal to noise ration that affects the value of the time reversed field a time zero.

In-vivo study shows the feasibility of passive elastography to retrieve shear wave velocity maps that are in agreement with the value given in the literature. In the other hand, in the passive shear wave velocity map (Fig 4.5) the abdominal muscle appears to be softer than the liver where it was expected to be stiffer. The measurement of the muscle elasticity is highly variable and depends on the muscle contraction (Nordez et al., 2008) and on the anisotropy . The shear wave speed measurement varies between 0.5 and 2 m/s respectively of a transversal and longitudinal polarization (Deffieux, 2008). Furthermore, Gennisson et al. shows that the shear wave speed is

2.5 times higher for a biceps in rest state than in a muscular contraction. In our case it is difficult to identify the polarization of muscular fibers and during the acquisition the abdominal muscle was not contracted. The means passive shear wave velocity value is 0.45 ± 0.35 m/s.

Indeed, a bias on the shear wave speed measurement at the boundary of a cavity has been observed. This value is in agreement with the literature, but still need more investigation to identify the origin of the low shear wave speed value in the muscles. This is due to the fact that the low frequencies feels the boundaries of the cavity and become guided by these boundaries. We have verified this hypothesis experimentally. The result shows that when the boundaries conditions are rigid on the top and the bottom of the phantom, a gradient effect is observed on the reconstructed shear wave speed map. The accurate measurement of the shear wave speed is in the center of the cavity, how is a few shear wavelengths away from the boundaries. This effect disappears when the boundaries condition is set to free. This kind of boundaries condition effect could be observed due to the stress applied by the probe on the surface of the phantom or an organ. And also in the case of thin layers such as the cornea that could play the role of wave guide.

The results presented in this chapter show the possibility to use the physiological noise in order to passively reconstruct quantitative shear wave speed map of biological tissue. Again by passive, it is meant with no shear wave sources other than natural muscle activities. The quantitative shear wave speed maps in the CIRS® phantom are in agreement with the elasticity maps provided by the active methods, namely the Aixplorer®, considered as a gold standard. `

However, an exhaustive study gathering more subjects should be realized in order to perform more accurate statistics. Thus to begin with, a clinical study that gathers patients with different fibrosis stages need to be realized. This will allows to shows the feasibility of passive elastography to diagnostic liver fibrosis and allows a significant comparison with other clinical studies.

Finally, the question about the contribution and the input of passive elastography approach compared to shear wave imaging techniques can be asked. Passive elastography approach could be used where the Aixplorer® is not capable to generate shear wave with radiation pressure. For example, in the case of the prostate, despite the fact that a ultrasound image can be performed at more than 4 cm. Studies show that the acoustic radiation force impulse is attenuated in large prostate and often can generate shear wave only in the first 3 – 4 cm (Barr et al., 2012; Correas et al., 2014). A study realized by the world federation of ultrasound in medicine and biology

(WFUMB) on the liver shows that obesity is a common limitation of transient elastography methods due to the difficulty to generate and track the shear waves in the liver obese patient. As well on patient with narrow intercostal space and cannot technically be performed in patients with ascites due to the rapid attenuation of the induced shear waves (Ferraioli et al., 2015). These are typical clinical situations where passive elastography can provide elasticity measurement since no shear waves are needed to be actively generated. The Food and Drug Administration (FDA) limitations are also an obstacle for radiation pressure based elastography. In sensitive organs such as the cornea, the thermal and the mechanical index are very low. It thus prevents from generating efficient shear waves.. Nonetheless, the feasibility of passive elastography to conduct shear wavelength tomography from naturally induced shear wave in the cornea has been demonstrated with an OCT system.

As a conclusion passive elastography could well be a complimentary technique that would allow estimation of elasticity where active methods fail.

4.2 Toward Elastography of Surface Waves with an Optical Ultrafast Camera

Optical Coherence Elastography (OCE) is an optical based methods for the characterization of soft tissue (Razani et al., 2012b; Wang et al., 2012b). This method has a medical application in the field of ophthalmology and dermatology, and provides elasticity maps with a micro-scale resolution. However, the complexity of the experimental setup, the invasive aspect of the shear wave source (e.g. radiation pressure, air puff) and the small visualized are (in the order of few millimeters) are the major limitations for in-vivo applications OCE.

In this study we present a fully optical system that allows imaging the propagation of the surface waves, and could be a lighter version of OCT systems. The advantages of this system are: the simplicity of the setup, a larger field of view (in the order of few centimeters) and ultrafast acquisition. In the other hand, only surface waves can are visualized compered to OCE systems that provide measurement inside the sample.

Depending on the surface of the sample is plane or curved, respectively one or two ultrafast optical cameras are need. This technique allows the measurement of the displacement and the resulting strain on the surface of the sample. Optical systems are usually used to study the failure process of materials under a static or quasi-static mechanical stress. Different studies were realized with this kind of optical systems in biomedical engineering such as: study of the mechanical properties of beef cornea (Boyce et al., 2008) and measure the anisotropy on a mouse carotid (Sutton et al., 2009).

In this study we will show the feasibility to use this optical based method to visualize a dynamic stress. This consists on imaging the propagation of an actively induced surface wave (Rayleigh wave) at the surface of a homemade gelatin phantom. Three experiments will be resented: (1) the feasibility to visualize small vibration due to surface wave propagation on a plane isotropic phantom. (2) Will we test the ability to characterize the anisotropy of a plane anisotropic tissue mimicking phantom through the measurement of the surface wave speed flow two direction of propagation. (3) A last experiment will be conducted on dome-like phantom (curved surface).

Surface wave imaging using a single camera: *experimental setup*

The first question investigated in this study was the ability of an optical system to detect small amplitudes of surface waves. Thus, the first experiments were performed on a homemade gelatin phantom. An ultrafast digital camera (Phantom® v710) was positioned vertically above the

phantom (Fig 4.6). The camera is connected to a host computer in order to save the digital images. The frame rate was set at 4000 frames / second. The surface of the phantom is illuminated by a white light (LED) in order to allow a good coupling between the camera and the phantom. The surface waves are created with a point-like source mounted on a mechanical vibrator (Fig 4.6). To avoid the source to be present within the imaging field, a metal rod (1 mm diameter) was inserted in the bulk of the phantom until it reaches the surface under examination (Fig 4.6 left). A 1000 Hz impulse was generated by a function generator (Tektronix®, AFG 3022B).

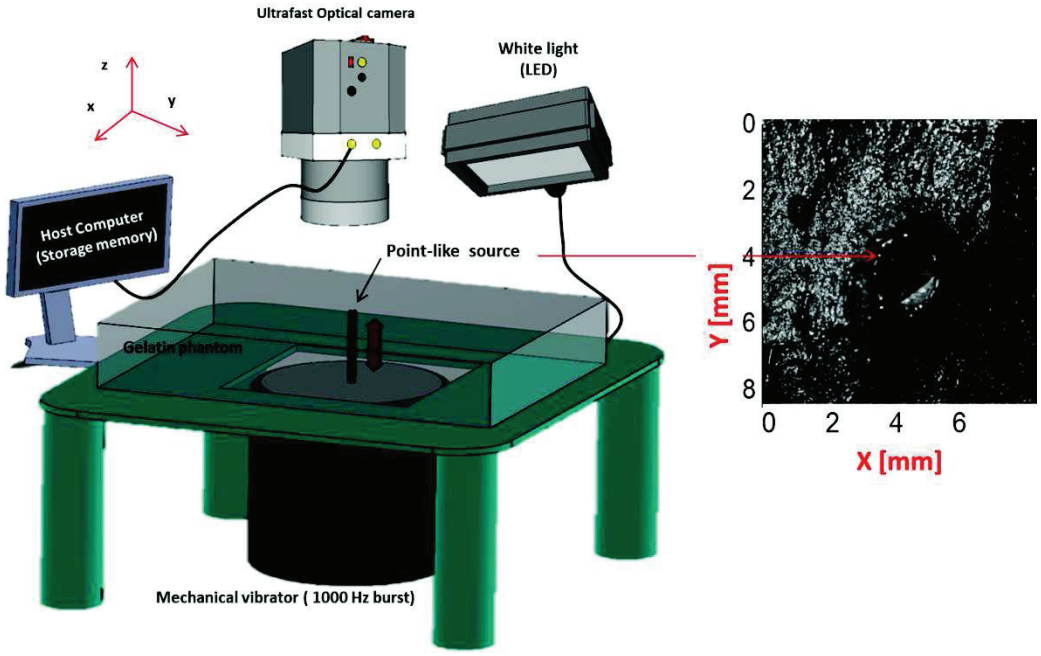

Figure 4.6. Left) experimental setup for imaging the surface wave propagation with 2D correlation method. Right) 8 mm^2 image of the phantom surface obtained by the digital camera where the point-like source is visible.

Note that the generator was synchronized with the ultrafast camera in order to trigger the acquisition. The presence of an optical random pattern equivalent to the ultrasonic speckle at the surface of the phantom is necessary in order to track the induced displacement. Usually a paint spray is used to covers the surface with speckle. But with this phantom, the presence of graphite was sufficient to create this speckle ("Le moucheté" in French) (Fig 4.6 Right). One hundred images were saved in the memory of the host computer.

The induced displacement field is computed with software Vic® 2D. It uses tracking algorithm know under the name of "Digital Image Correlation" (DIC). This technic is very similar to the speckle tracking algorithm used in ultrasound elastography. It is based on the correlation of consecutives images that represent the surface of the sample at different solicitation (Sutton et al., 2009). Vic® 2D provides the two components (U and V) of the displacement field parallel to the surface.

4.2.1 Wave speed measurement on a isotropic phantom: feasibility study

An approximation of the divergence is computed from the two component of the displacement field using: $Div = dU/dx + dV/dy$. The resulting field is presented on six snapshots (Figure 4.7 left) from a one hundred frames movie. The induced displacements are clearly visible as a spherical wave front propagating from the position of the point-like source toward the boundaries. The amplitude of this displacement is ranging between $\pm$ 500 µm. The speed of the surface wave can be measured from the seismogram-like representation (Figure 4.7 left). The slops (red dotted lines) are representative of the propagation of the waves in the x direction from the both side of the source. Thus, the shear wave speed can be computed as $C_x = \frac{\Delta x}{\Delta t} = 2.53 \pm 0.32\ m/s$. The wave speed measured in the y direction $C_y = \frac{\Delta y}{\Delta t} = 2.2 \pm 0.41\ m/s$, which is in the same order of magnitude as C_x. This means that the phantom is isotropic as expected.

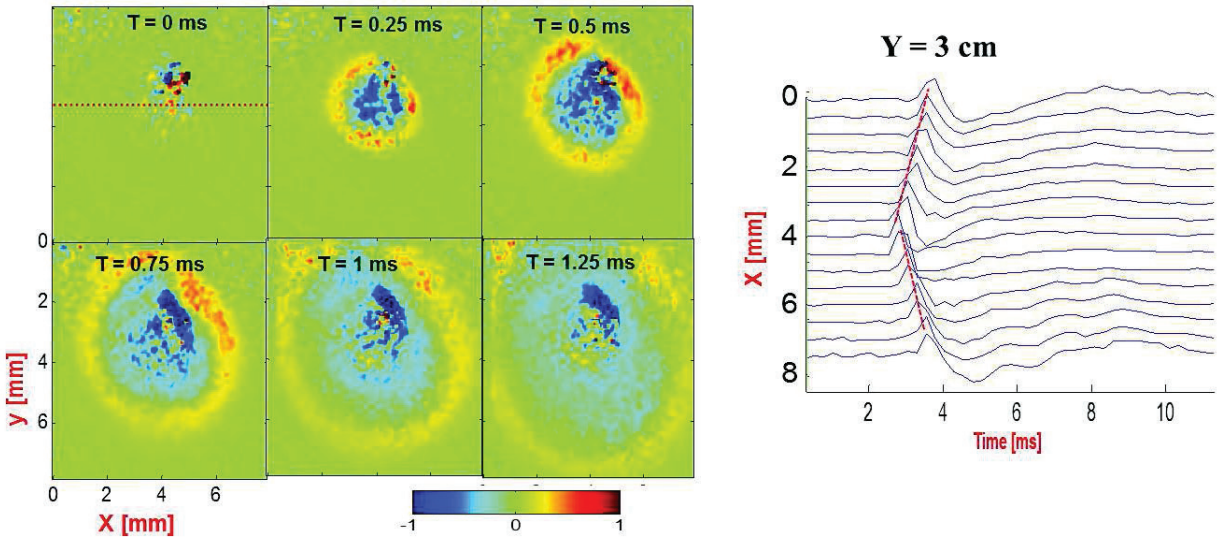

Figure 4.7. Left) Six snapshots from a 100 frame displacement movie are presented. The amplitude of the induced displacement is between ± 1 mm. Right) a seismogram-like representation for the measurement of the wave speed in the x direction (C = 2.53 ± 0.32 m/s).

4.2.2 Wave speed measurement on a transversally isotropic phantom

The same experimental setup as in the isotropic phantom was used, except for the tissue mimicking phantom. An anisotropic phantom has been made from a Polyvinyl Alcohol (PVA) solution) (Chatelin et al., 2014). The six first snapshots (Fig 4.8 top left) show the U component of the displacement field. This is visible as a dipole in the x direction. Likewise, for the V component of the displacement field which appears as a dipole in the y direction of space.

As mentioned before, the aim of this experiment was to demonstrate the ability of this method to characterize anisotropy through speed measurement. Thus, the wave speed in the transversal direction (Fig 4.8 top right) $C_x = 3.08 \pm 0.24$ m/s is compared to the shear wave computed from the longitudinal direction (Fig 4.8 bottom right) $C_y = 4.02 \pm 0.48$ m/s. The difference between the two speeds C_x and C_y is about 25%. This results is in agreement with what expected in terms of the anisotropic properties of the homemade phantom.

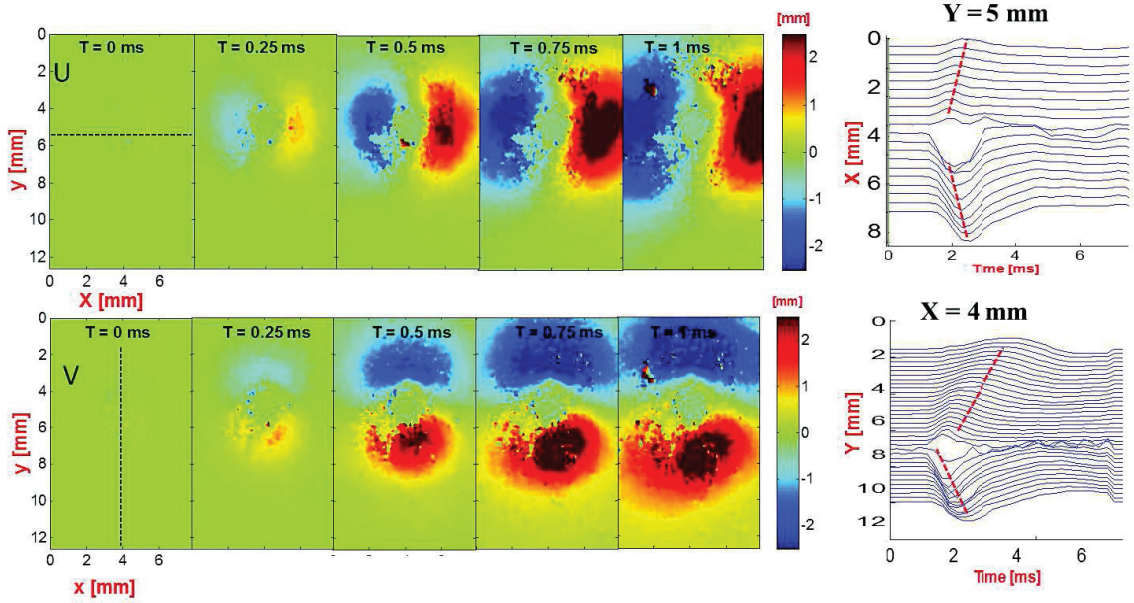

Figure 4.8. Snapshot of the transversal component U (top left) and the longitudinal component V (bottom left) of the displacement field. Seismogram-like representation for the measurement of the transversal speed (Top right) Cx = 3.08 ± 0.24 m/s and le longitudinal wave speed Cy = 4.02 ± 0.48 m/s

4.2.3 Surface wave imaging using a stereo-vision system on a curved surface

Usually in elastography application we deal with curved surfaces such as the cornea. As mentioned above for this kind of surface a stereo-vision system is needed in order to perform an accurate measurement of the wave speed.

Thus, to mimic the case of surface wave propagation a curved surface. The experiment was conducted on a homemade dome-like gelatin phantom (Fig 4.9 b). In this experiment we had to use the white paint spray in order to create the speckle at the surface of the phantom. For the rest of the setup the same parameters as in the 2D experiment was used. As mentioned above, in the case of a curved surface a stereo-vision systems composed of two synchronized cameras is need. This experiment required a calibration step. This allows to the software (Vic® 3D) to defined the exact spatial position of the two cameras. Then, the surface of the dome is reconstructed from the combination of both images obtained from each camera (Fig 4.9 c). Thus, it is possible to track the propagation of the wave trough the curvature of the sample, and to perform an accurate measurement of the surface wave speed.

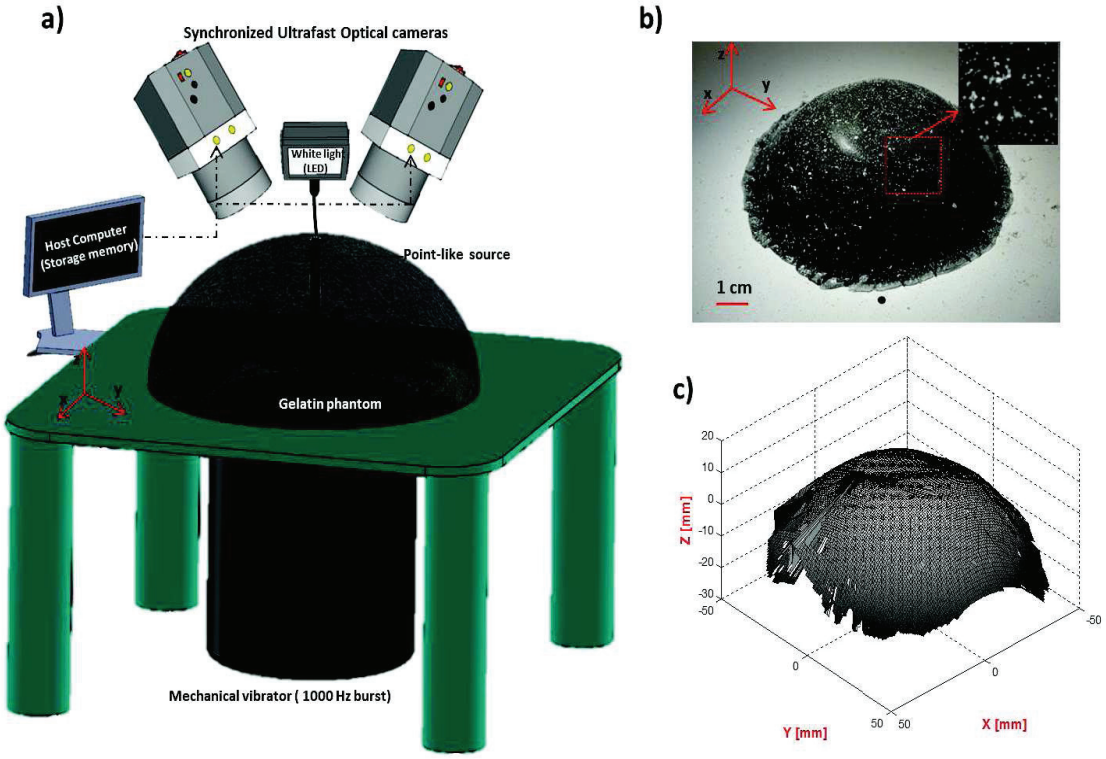

Figure 4.9. a) Experimental setup for imaging the surface wave propagation with stereo-correlation method. b) a picture of the dome-like homemade gelatin phantom. c) the surface of the phantom reconstructed from the combination of two images from the digital cameras.

In addition to the U and V, the stereo-vision system allows measuring the out of plan component of the displacement field W (Fig 4.10). In our case the two first components (U and V) are sufficient to measure the surface wave speed. However, the out of plane component shows a perfect spherical wave front. Thus, the measurement of the wave speed is easier, especially in the case of a heterogeneous phantom (e.g. the presence of a soft or a stiff inclusion). The measured shear wave speed is 2.27 ± 0.24 m/s. This is in the same order of magnitude as what is usually measured in this kind of tissue mimicking phantoms. The measured amplitude in this experiment is ten times lower ($\pm$50 µm as in the first two experiments).

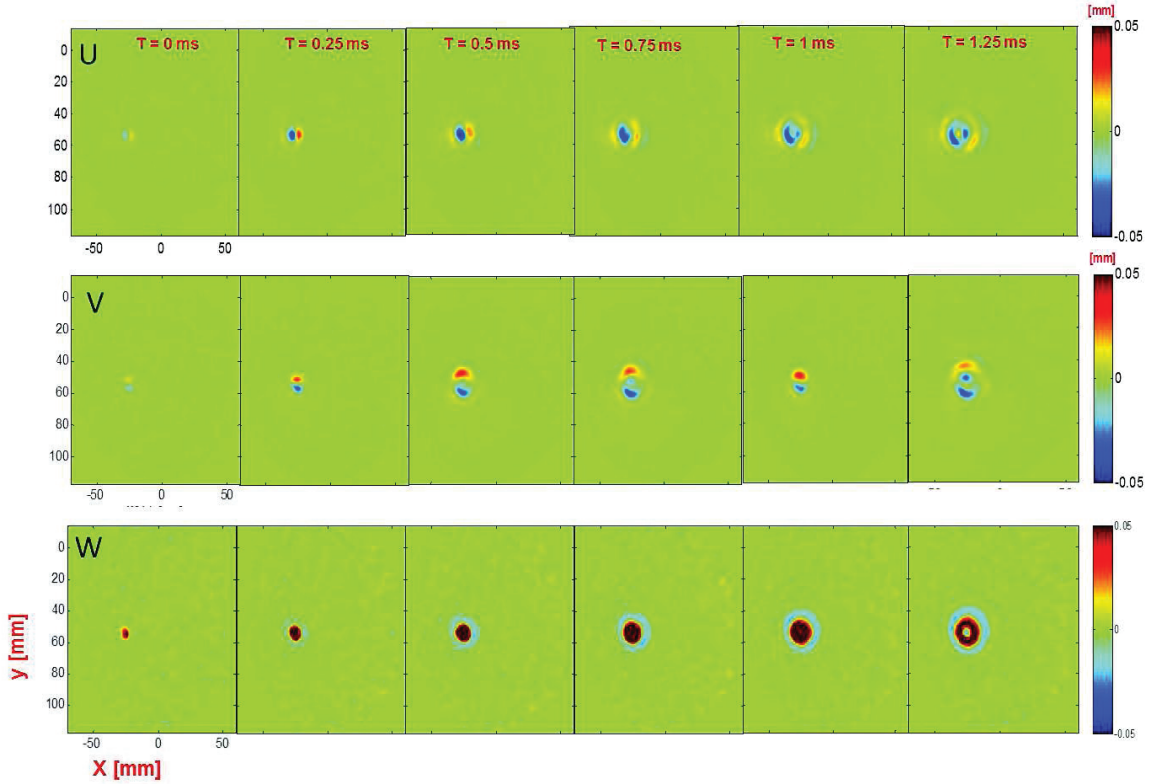

Figure 4.10. Snapshot of the transversal component U (top) and the longitudinal component V (middle) and the out of plane component W (bottom) of the displacement field. The amplitude of the displacement is ranging between ±50μm.

4.2.4 Discussion

For this proof of concept experiments, we made the choice to go back to the origin of transient elastography. Thus, a controlled source was used. The compatibility with our passive approach is now evident once the feasibility to detect actively induced surface waves was demonstrated. This opens offers the possibility to use an optical system for elastography applications.

The accuracy of this measurement was demonstrated through the characterization of anisotropic phantom. In other word, we have shown the possibility to measure two different wave speeds (C_X and C_Y) that was in agreement with the expected results. In practice, the soft tissue in the human body cannot be considered as perfectly plane surface, especially in the case of the cornea. Therefore, the establishment of a stereo-vision system that allows the visualization of wave propagation on curved surfaces was necessary. The main difficulty of this last one remains in the calibration of the two cameras and the sharpness of the obtained images with the lighting.

Always in the perspective of clinical applications, the straight forward application of this method could be the diagnosis of glaucoma. Glaucoma occurs due to pressure elevation in the cornea, and this could lead to a globe stiffening of the cornea that can be measured from the surface. However, the white paint spray cannot be used in order to create the speckle in the cornea for example. Therefore, another kind of speckle has to be investigated such as optical speckle. Regarding our background, the next step of this study is to use noise correlation methods in order to retrieve mechanical properties, first in a phantom then in-vivo. Either in a passive mode, in this case we have to be able to measure the natural vibration with this new system. But we keep in mind the possibility to use an active source to create a diffuse wave field at the surface of the soft tissue (e.g. an air puff (Wang et al., 2012b)). This system can also be integrated to endoscopic camera for the diagnosis of colorectal cancer. From a tomography point of view, this technic should be tested for imaging an elastic heterogeneity at the sallow surface. Thus, we can show the feasibility to measure subsurface elastic properties.

5 Beyond the Diffraction Limit: The Super Resolution in Passive Elastography

An experimental study was performed in this chapter to evaluate the resolution limit of passive elastography approach. The experiments were conducted on a homemade gelatin phantom containing two stiff inclusions. In this study we demonstrate that the resolution of the final reconstruction is in the same order of magnitude of the ultrasonics wavelength. Thus, it is possible to image millimetric elastic heterogeneities with centimetric shear wavelength. In other word, with our approach we are not limited by the diffraction limit in the far field.

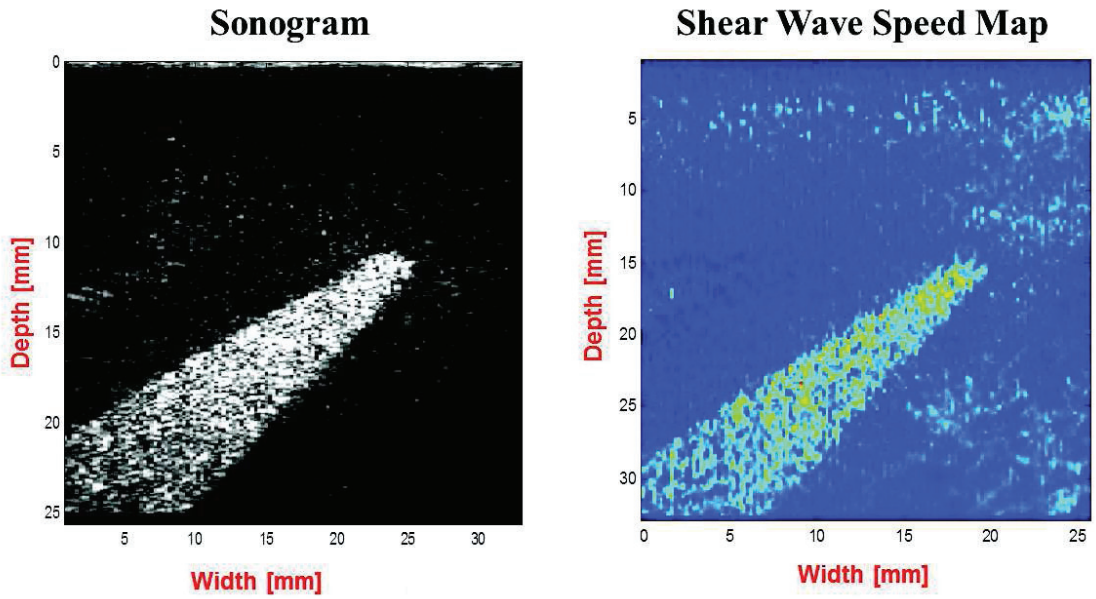

5.1 Introduction

In 1873, Ernst Abbe (Abbe, 1873) shows that smallest distance that can be resolved between two point-like targets with an optical system has a physical and not just technical limit. This distance equal to the half of the wavelength is well known under the name of *Diffraction Limit*. Only far field imaging systems are concerned by this limitation. This is due to the fact that the subwavelength details are carried by the evanescent waves. This waves decrease exponentially with the distance of propagation and usually do not reach the far field imaging plane. Since then, this limit was considered as the resolving power of any far field imaging systems (optic, acoustics, etc). This theoretical limit is also known under the name of *Rayleigh Criterion* (Rayleigh, 1896). The small difference between the two limits is reflected in the definition of this distance that separate the targets being visualized (cf. 5.3.2). Nevertheless, Rayleigh criterion terminology is the most used in the literature. Several studies were performed in order to overcome this theoretical limit. Near-field microscopy technique aims to convert evanescent waves into propagative wave. The basic principal is to place a subwavelength scatters in the near field of the object to be imaged. The scatters convert the evanescent waves to propagative waves that can be detected in the far field (Betzig and Trautman, 1992).

This approach was also tested for sub-wavelength focusing of microwaves (Lerosey et al., 2007). In 2014, Eric Betzig, Stefan W. Hell and William E. Moerner received the Nobel Prize of chemistry for their studies on the super resolution. They achieved optical microscopy images with a resolution beyond the diffraction limit (Betzig et al., 2006; Hell and Wichmann, 1994). Time reversal mirror techniques was also used in order to beat the diffraction limit (Blomgren et al., 2002; de Rosny and Fink, 2002, 2007). This, method requests a prior knowledge of the original source of the evanescent waves in the near field. Nevertheless, in an experimental study with a time reversal mirror, Conti et al shows the possibility to achieve sub-wavelength refocusing using a near field time reversal mirror without a prior knowledge of the probe source (Conti et al., 2007).

Ultrasonic waves are also affected by the diffraction limit. The trade-off between the resolution and the penetration of ultrasonic waves prevents the ultrasonic scanner from achieving images at sub-millimeter scale in deep organs. Inspired from optical localization microscopy, Errico et al developed a new technique for deep super-resolution vascular imaging (Errico et al., 2015). Ultrafast ultrasound localization microscopy allows performing sub-wavelength structural

imaging (less than ten micrometers in diameter) at more than ten millimeters below the tissue surface. The high resolution of elastography techniques is crucial for earlier diagnosis of small cancer nodules. This leads as to a question about the resolution of elastography techniques that uses ultrasound scanners. The elastographic resolution was widely studied for strain imaging elastography technique (Cohn et al., 1997; Cook et al., 2000; Alam et al., 2000; Righetti et al., 2002).

In this study we propose to experimentally evaluate the resolution of the passive elastography technique. Our hypothesis is that the resolution of passive elastography is only limited by the ultrasonic wavelength. Therefore, three ultrasonic probes have been used (i.e. 5 MHz, 9.5 MHz and 15 MHz central frequency) to visualize the same induced shear wave field in a homemade gelatin phantom. We expect that the resolution of the final reconstruction should be improved by only increasing the ultrasonic wavelength. Thus, we can visualize elastic heterogeneities at the millimitric scale with centimetric shear wavelength.

5.2 Experimental Setup

5.2.1 Tissue-mimicking Phantom

The experiments were conducted on a homemade aqueous solution. It contain gelatin (Sigma Aldrich, St Louis, MO, USA) for stiffness control and graphite (Sigma Aldrich, St Louis, MO, USA) for ultrasonic scattering. Two stiff cylindrical inclusions were embedded in a softer homogenous surrounding phantom (Fig 5.1). The gelatin concentration in the inclusion was 9% (w/v) while it was 3% (w/v) in surrounding phantom. The graphite concentration was the same in both solutions, 0.5% (w/v). The preparation was realized in two steps. First, the solution for the surrounding phantom was prepared. Then it was poured into a mold for cooling. The mold was shaped like a truncated cavity in order to break the symmetry of the reverberation from the boundaries. Two full cylinders were fixed on the bottom of the mold in order to create a vacuum for the inclusion. After one hour of cooling, the inclusion solution was poured in the vacuum created by the cylinders and kept in the fridge for two more hours.

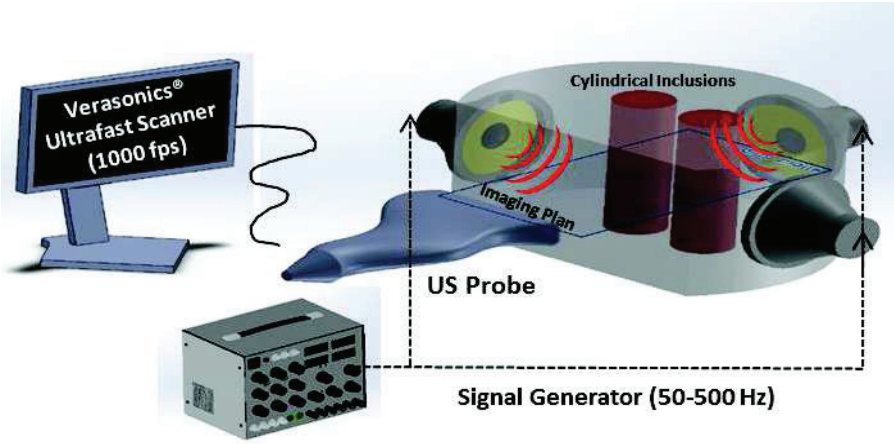

Figure. 5.1. The imaging system is a Verasonics® vantage ultrasound scanner. Three electromagnetic shakers connected to a signal generator create shear waves inside the tissue mimmicking phantom. The input signal is a 500 ms sweep, with frequency ranging from 50 to 500 Hz. The homemade gelatin phantom contains two stiff cylindrical inclusions.

5.2.2 Shear Wave Field Generation

A random shear wave field is generated in the phantom with multiple non-synchronized electromagnetic shakers (RS 4 cm Slimline Speaker Driver 628-4658, 8Ω, 1w) (Fig 5.1), positioned randomly on the boundary of the phantom and connected to a signal generator (Tektronix®, AFG 3022B). No synchronization between the shear wave sources and the ultrasound scanner is needed. The excitation signal was a 500 ms duration sweep with a frequency ranging from 50 to 500 Hz, repeated during two seconds.

5.2.3 Ultrafast Imaging of Diffuse Shear Wave Field

As stated above, the aim of this study is to measure the resolution of the reconstructed shear wave speed map with different ultrasonic wavelength. Therefore, three ultrasonic arrays have been used. They operate at three different central frequencies i.e. 5 MHz, 9.5 MHz and 15 MHz. The imaging probes were connected to Verasonics® Vantage ultrafast ultrasound scanner (Verasonics Inc., Redmond, WA, USA). A plane wave imaging sequence without compounding was used to acquire 1000 frame at a frame rate of 1000 frames / second. The imaging plan was chosen to be perpendicular to the cylindrical inclusions (Fig 5.1).

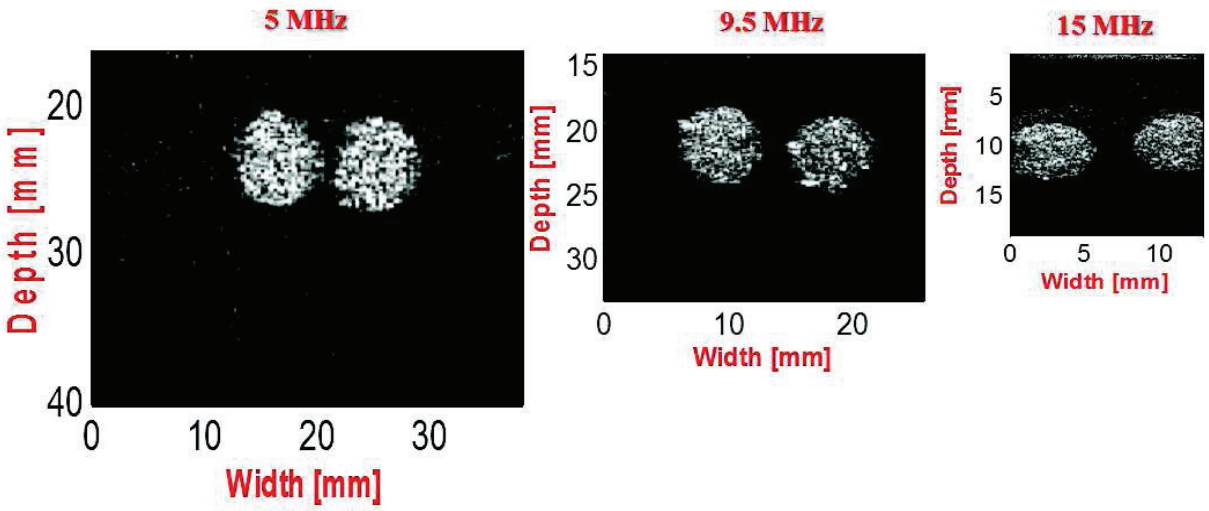

Figure. 5.2. Sonograms (B-mode images) of the three experiments, the inclusions are visible in the center. 1000 images are saved in the host computer. Only a single snapshot from each experiment is presented in this figure.

The final beamformed images acquired with a 2D B-mode (Fig 5.2) were saved in the memory of the host computer. We can already observe the improvement of the resolution of the B-mode image due to the reducing of the ultrasonic wave length.

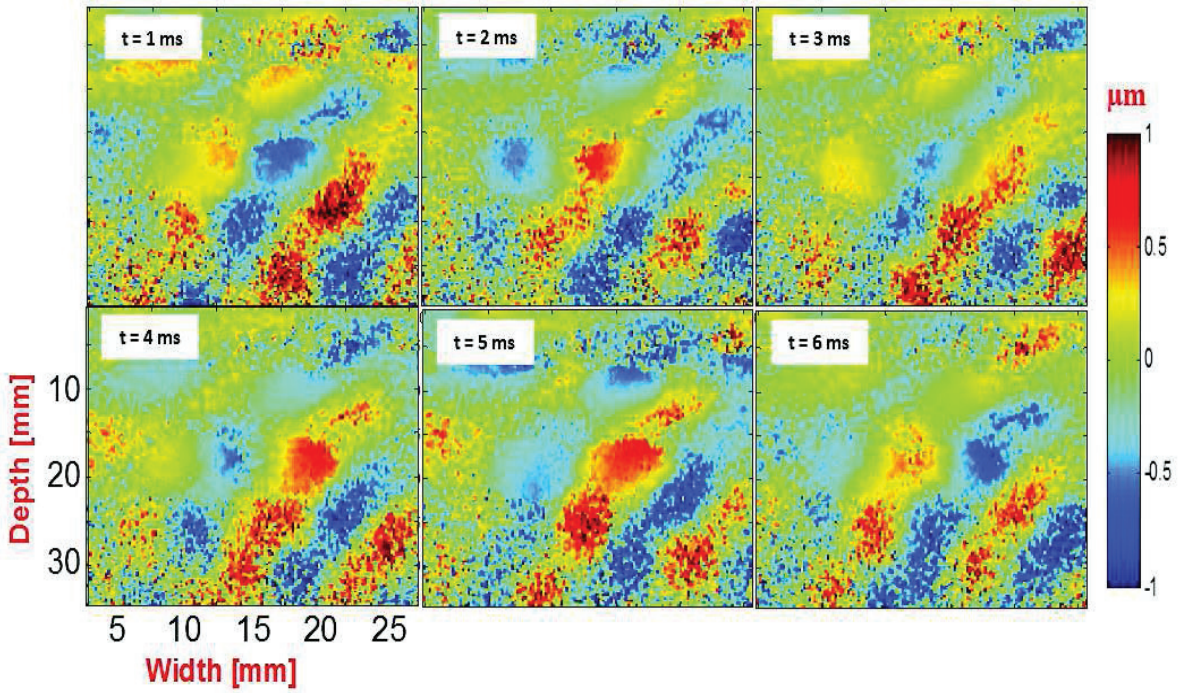

Figure.5.3. Six consecutive snapshots of the 2D axial displacement field measured with the 9.5 MHz probe are presented. The frame rate was 1000 frames/second. The amplitude of displacement is ranging ± 1µm.

The induced displacements were computed by the speckle tracking algorithm from the acquired B-mode images. Six consecutive snapshots from a movie of 1000 images of the measured displacement field are presented in Fig 5.3. The amplitude of the displacement is ± 1µm. The measured displacement central frequency is f~100 Hz, unchanged during the three experiments.

5.3 Results

5.3.1 Shear Wave Speed Map

As mentioned above, three acquisitions were performed with three different ultrasonic arrays i.e. 5 MHz, 9.5 MHz and 15 MHz, respectively Figure 5.4 .a, b and c. The measured shear wave speed is C_{Inc} = 3 ± 0.7 m/s and C_{bakg} = 1 ± 0.8 m/s respectively in inclusion and in the background, for both the 5 MHz and 9.5 MHz experiment. The size of the reconstructed inclusion with passive elastography is about 2 mm, and the main shear wavelength *($\lambda = C/f$)* is 3.5 cm in the inclusions and 1.8 cm in the background.

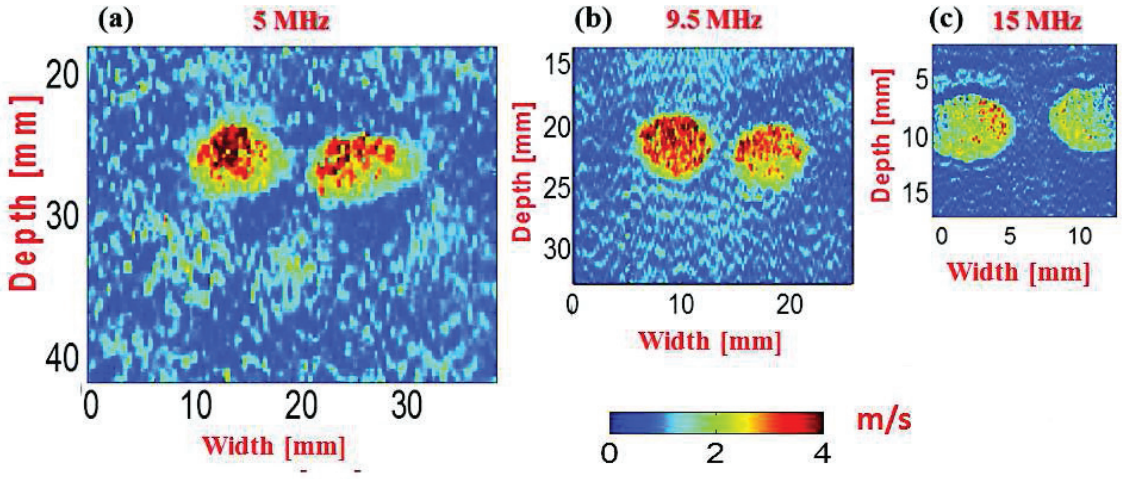

Figure 5.4. The constructed passive shear wave speed maps. The mean value of the shear wave speed in the inclusions is 3.5 m/s and 1.8 m/s in the surrounding background.

It is very important to keep in mind that the created shear wave field remains unchanged for the three experiments. There is a high correlation between the B-mode images (Fig 5.2) and the shear wave speed maps (Fig 5.6) in terms of: the size, the shape, and the spacing between two inclusions. In following we will measure the resolution on the passive shear wave speed maps and compare it to the resolution measured in the B-mode images. Nevertheless, we can observe qualitatively that the resolution of the final reconstruction is improved by reducing the ultrasonic wavelength without changing the frequency contents of the shear wave field.

5.3.2 The Resolving Power

This difference between Abbe's limit and Rayleigh's limit resides in the definition of what is meant by two objects being resolvable from each other. This consists in the definition of the distance *"a"* (Fig 5.5) that separates the two objects being imaged. For Abbe criterion "a $\approx$ *0.5* λ*"*, while Rayleigh criterion stats that "$a \approx 0.61\lambda$*"*, with λ the light wavelength. If we consider two point-like objects (Fig 5.5. top), each target has a point spread function (PSF) (Fig 5.5. bottom). The distance "*a"* is measured from the distance that separates the two pics of both PSFs. The objects are resolved if "*a"* is larger than $\lambda/2$ (Fig 5.5 (a)). The Rayleigh limit is reached for "*a"* equal to $0.61\ x\ \lambda$ (Fig 5.5 (b)). The objects cannot be resolved if *"a"* is smaller than the half of light wavelength $0.61\ x\ \lambda$ (Fig 5.5 (c)).

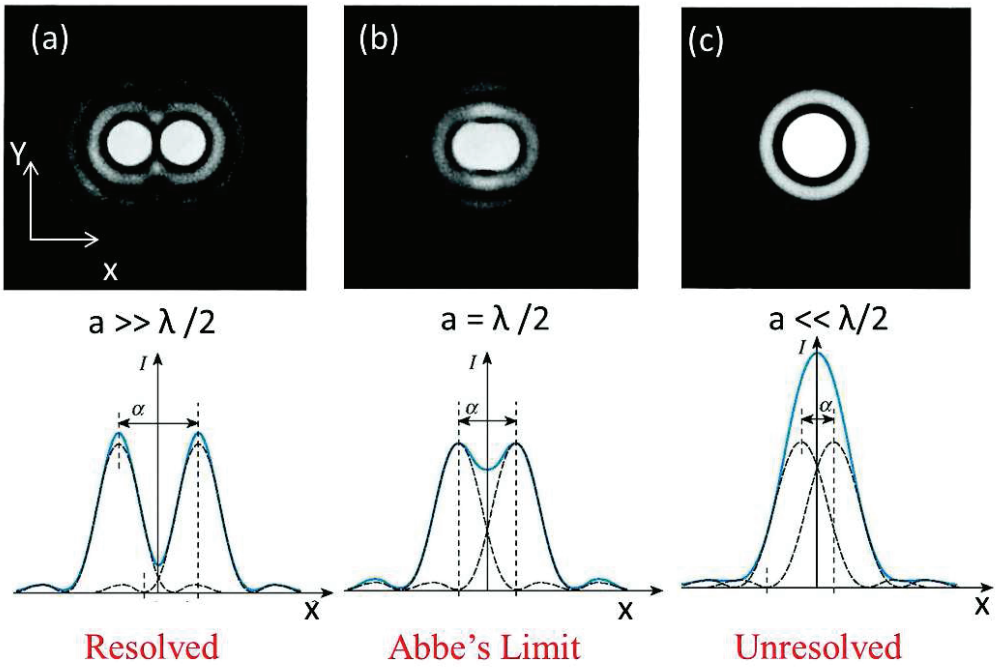

Figure. 5.5. Top: intensity profile of two points –like targets. Bottom: Profile along the x direction. (a) the object are resolved since the distance a between the pics is higher than the half of wave length. (b) the Abbe limit is reached, the targets are barely resolved. (c) the targets are not resolved, even if the pics are still separated but the diffraction limit has been reached. source Juste Lelong. Google Image

5.3.3 Resolution Measurement: in optic *vs* in elastography

In optic the resolution "R" of an imaging system is measured as the full width at half maximum of the PSF intensity *"I"* (Fig 5.6 a). This is valid when the imaged target is point-like object, with a diameter "d ~ λ". However, in elastography the visualized objects have usually a diameter "D" ranging from few millimeters to few centimeters. In this case the optic's method can be extrapolated to elastography application. Thus, the resolution "R" is measured from both side of an axial or lateral profile (Fig 5.6. b). From each side only the half of the resolution (R/2) according to optic method is measured as the width at half maximum. For a fair comparison, the axial resolution is measured on both the shear wave speed maps and the B-mode images.

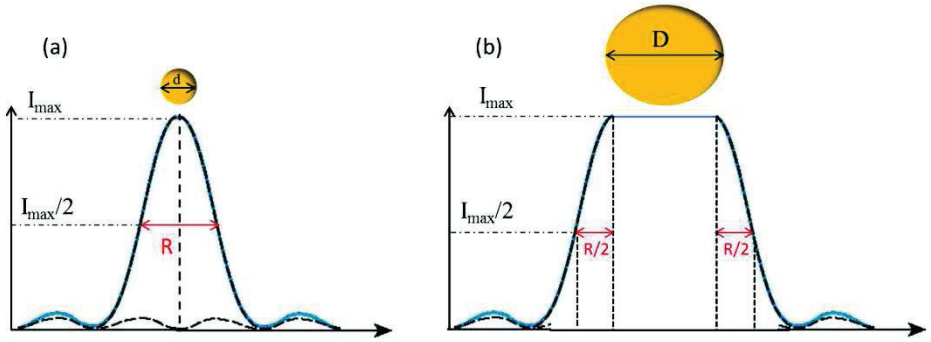

Figure 5.6. (a) in optics the resolution "R" of an imaging system is measured from the PSF as the width at half maximum (WHM). (b) Extrapolation of (a) for elastography application. The half of resolution is measured from each side of the axial or lateral profile.

For an accurate measurement on the experimental data, the final resolution is measured flowing two steps as presented on **figure 5.7**. First, the mean shear wave speed value "Cmax = 3 m/s" is computed in the inclusion from the Region Of Interest 1 (ROI_1) and in the surrounding phantom from ROI_2 "Cmin = 1 m/s" (Fig 5.7 a). Second, the two values are represented on the axial profile (Fig. 5.7 b) and used as references to compute the half maximum (Fig. 5.7 c). The half maximum is computed between the min and the max shear wave speed value. Thus, the half of the resolution is equal to the abscissa of the maximum shear wave speed value minus the abscissa of the shear wave speed value at half maximum. Same procedure is flowed to compute the resolution from the other side on the axial profile, from the second inclusion, and also for the B-mode images.

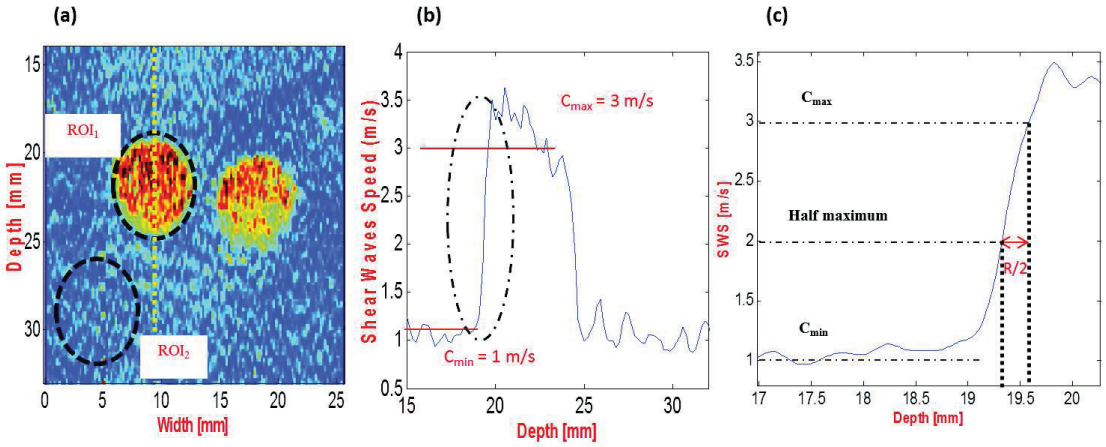

Figure 5.7. (a) Shear wave speed map (9MHz experiment), the mean shear wave speed value (C_{max} = 3 m/s) is computed in the inclusion from ROI_1 and in the surrounding phantom from ROI_2 (C_{min} = 1 m/s). (b) Axial profile along the yellow dashed line (see (a)). The plateaus (red horizontal line) correspond to the min and max shear wave speed value. (c) Zoom on the black dashed line (see (b)), the half maximum is computed between the min and the max shear wave speed value. The half of resolution is equal to the abscissa of the max value minus the abscissa of the value at half maximum.

5.3.4 Quantification of the B-mode images and shear wave speed maps resolution

The method described before was applied on both the shear wave speed maps and the B-mode images resulting from the three experiments (5, 9.5 and 15 MHz). The resolution is measured form the axil profiles (Fig 5.8), top B-mode profiles and bottom shear wave speed maps profiles. The amplitudes were normalized in order to facilitate the comparison between the B-mode and shear wave speed maps. Small fluctuation of the shear wave speed value and the B-mode signal can be observed. To overcome this random fluctuation, the axial profiles are retrieved from a lateral average window of five lines.

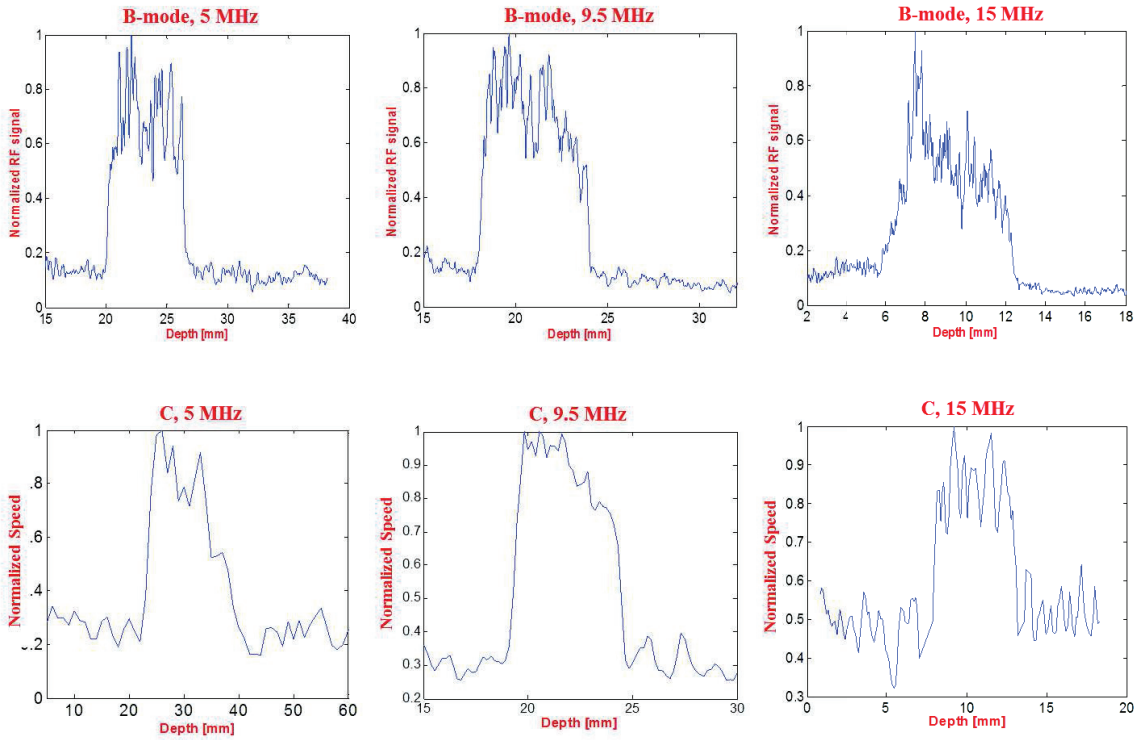

Figure 5.8. B-mode axial profiles on top and the corresponding shear wave speed axial profiles bottom, computed from an average a lateral window of five RF lines to reduce the fluctuation due to the noise.

The measured half resolution (R/2) values are summarized in Figure 5.9. As expected, the resolution of B-mode images is (blue stars Fig. 5.9) are in agreement with theoretical ultrasonic half wavelength (black circles Fig. 5.9). The measured R/2 of the shear wave speed map is five times higher than the resolution of the B-mode.

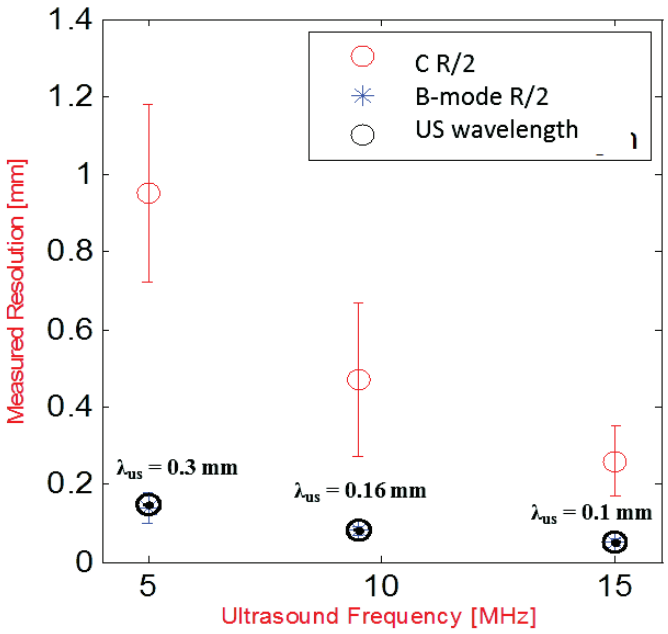

Figure 5.9. The measured half resolution of the passive shear wave speed maps corresponding to 5, 9.5 and 15 MHz are respectively 0.95 ±0.23 mm, 0.47 ± 0.22 and 0.26 ± 0.09 (red circles). The half resolution measured from the B-mode images are respectively 0.14 ± 0.04, 0.08 ± 0.01 and 0.05 ± 0.01 (bleu stars). The resolutions of B-mode images are compared to the theoretical ultrasonic half wavelength (black circles).

Finally, a last experiment was conducted on a homemade gelatin phantom with a stiff inclusion shaped like a triangle. The inclusion was visualized with a 9.5 MHz ultrasonic probe (Figure 5.10 left) connected to an ultrafast ultrasound scanner (Vantage®). The frame rate was fixed to 1000 frames / second. A shear wave field was created inside the phantom with three mechanical shakers. The size of the triangle edge is about 2 mm. The reconstructed shear wave speed map (Figure 5.10 right) shows a good agreement with the B-mode image. More precisely the edge of the triangle is very well retrieved. Once again, these results show that the resolution of passive elastography is very close to the resolution of ultrasound images.

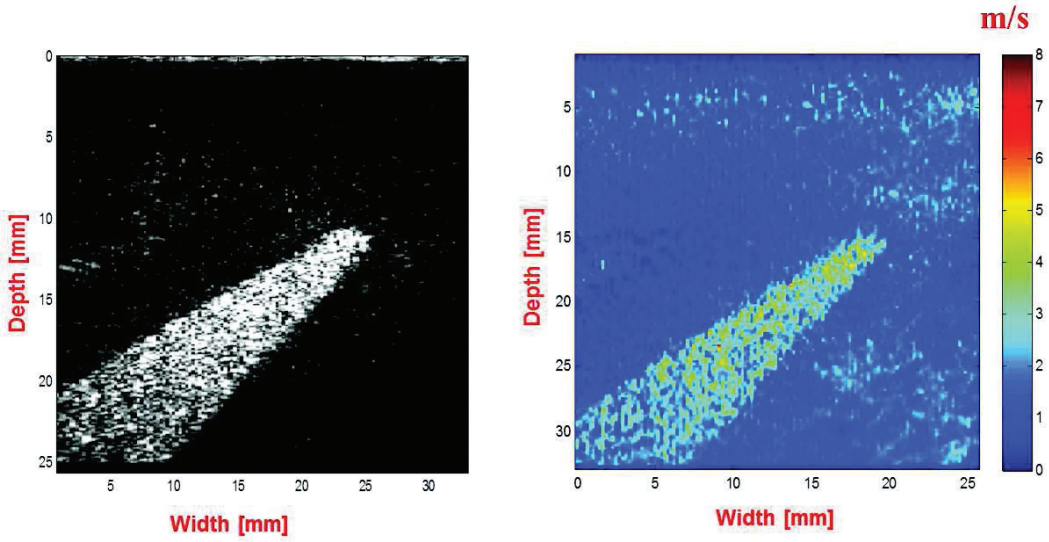

Figure 5.10. ***Left)*** *B-mode image where a triangular inclusion is visible.* ***Right)*** *The reconstructed shear wave speed map.*

5.4 Discussion

Experiments were conducted on a homemade gelatin phantom, with two stiff cylindrical inclusions. The results suggested that the resolution of the constructed passive shear wave speed maps is improved by only reducing the ultrasonic wavelength. Compared to the ultrasonic images (B-mode) the resolution of passive elastography images is five times below. This is due to the two steps of signal processing performed on the raw data: First, the measurement of the induced displacement from the RF data. As shown before (cf. 1.2.4), with the speckle tracking algorithm the displacement are measured inside a typical cross-correlation window. In our experiments the size of this cross correlation window is three times the ultrasonic wavelength. The overlapping window is equal to the third of the initial window. This means that the resolution of the displacement maps is two times below than the resolution of the B-mode.

The second processing that affects the resolution of the final reconstruction is the strain field measurement. Indeed, a strain field along the axial direction has to be measured in order to compute the shear wave speed map (Equation 2.8). To compute the strain a sliding axial window with four pixels length is used, the shift window is equal to one pixel. This causes a second degradation compared to the initial B-mode images. This question have already been treated by Righetti et al (Righetti et al., 2002) in a fully numerical study. It has been shown that the

resolution of static elastography is affected by the processing parameters chosen to compute the strain maps. Nevertheless, our approach is fully experimental and base on a quantitative measurement of the shear wave speed, which is not the case of static elastography.

5.5 Conclusion

In this study we have shown that the resolution of passive elastography is only limited by the ultrasonic wavelength and not by the shear wavelength. This is due to the fact that the shear waves are measured in the near field. Thus, we are not limited by the diffraction limit. However, our actual processing steps performed on the raw data allows to retrieve shear wave speed maps five times less resolved compared to B-mode images. In our opinion these results are not exclusively true for passive elastography. Such resolution could be achieved with the other shear waves imaging techniques. But, because of technical limitation, such as the computational time, and the signal to noise ratio, this resolution became hardly achievable.

General Conclusion and Perspectives

Works presented in this manuscript respond to the problematic of understanding and interpreting wave propagation in complex media, through the study of acoustic and elastic waves. This thesis was also an opportunity to test passive elastography in several applications. Through these applications, our novel time reversal based algorithm has been subjected to severe ordeal. Two major axes have been investigated: low frame rate imaging systems and high frame rate shear wave imaging.

Shear wavelength tomography have been tested through three different studies. First, naturally induced shear wave were observed in the brain of two healthy volunteers using magnetic resonance elastography. Usually a controlled shear wave source is needed to induced shear waves in the brain, and synchronization between the source and the scanner is essential to measure the shear wave speed. The experimental setup is standard magnetic resonance elastography is often very cumbersome for clinical application. With the passive approach there is no need to active shear wave source, which makes the setup very easy to implement in-vivo and does not change the usual practices of radiologist. In the other hand, only shear wavelength map can be reconstructed. Since passive elastography is the only approach that compute shear wavelength instead of shear wave speed with MRI scanners. It suffers from a lake of comparative studies about brain stiffness in the literature. Nevertheless, some laboratories start being interested by this approach. Future works will confirm the accuracy of this approach.

Second, Optical Coherence Tomography system has been used to conduct shear wavelength tomography in the eye of an anesthetized rat. The eye is composed of different thin layers. It is well known that Lamb-like waves that propagate in these thin layers is highly dispersive. Nevertheless, the shear wavelength map obtained with OCT is in agreement with the shear wave speed map obtained with ultrafast OCT sequence. These results are very encouraging and could be the solution for clinical application that suffers from the weakness of active sources to create shear waves without damaging the tissues.

High Intensity Focused Ultrasound applications are the principal research activities ot the LabTAU. The feasibility of passive elastography to monitor HIFU treatment has also been taken studied. Thus, preliminary study was conducted on porcine pancreas treated by HIFU. Through this study, the efficiency of passive elastography to characterize HIFU lesions was demonstrated using a low frame rate ultrasound scanner. We also intend to use MRI scanner to monitor HIFU treatment in the brain with interstitial HIFU probe.

Shear wave speed elastography methods such as the Fibroscan® and the Aixplorer® start being widely used in clinic for several pathologies. However, as mentioned above there is some situation were the generation of the shear waves is difficult. This could be the application field of passive elastography approach. Tissue mimicking phantom and in-vivo study realized with a high frame rate ultrasound scanner, shows efficiency our noise correlation based algorithm to perform quantitative measurement of the local shear wave speed from a diffuse shear wave field. This study should be followed by a further study that groups a statistically significant number of volunteers and patient. Nevertheless, the results described in the fourth chapter are very satisfying results in agreement with studies in the literature. Always with the objective to perform quantitative measurement of the shear wave speed, a proof of concept for surface wave imaging system with optical camera has been proposed. Actively induced surface have been observed with an ultrafast optical camera. The accuracy of wave speed measurement was validated on a anisotropic gelatin phantom.

The resolution of passive elastography has been evaluated via a fully experimental study. The results show that the resolution of shear wave speed technique is not limited by the shear wavelength, and it is in the same order of magnitude as the ultrasonics wavelength. This means that small cancer nodules could be detected before advanced stages, and allows provide appropriate treatment for the patient.

Finally, to finish this manuscript we would like to mention the fact that one of the objectives of this thesis was to extend the characterization of biological tissue by the measurement of the viscosity, the anisotropy and the nonlinearity. However, we made the choice to take advantage of opportunities that was presented to us to test passive elastography in several preclinical applications. Nevertheless, we keep in mind the importance of the viscoelastic parameter mentioned above that could be additional tools for an accurate soft tissue characterization.

6 Résumé Détaillé en Français

La modalité d'imagerie développée dans ce manuscrit repose sur deux concepts majeurs. En premier lieu, l'imagerie multimodale - ou multi-ondes - permet de tirer profit de la présence de deux types d'ondes vues par un seul système d'imagerie. Si l'on considère par exemple l'élastographie ultrasonore, les ondes de cisaillement dites lentes - se propageant à une vitesse comprise entre 1 et 10 m/s dans le corps humain - sont imagées grâce à des ondes ultrasonores dites rapides qui se propagent à une vitesse de l'ordre de 1540 m/s. La résolution des ultrasons et la sensibilité des ondes de cisaillement aux changements d'élasticité sont combinées pour construire une carte d'élasticité, permettant ainsi de distinguer de manière quantitative et précise les nodules cancéreux des tissus sains.

La deuxième idée est basée sur les méthodes de corrélation du bruit. Elle tire avantage du bruit physiologique naturellement présent dans le corps humain, afin d'éviter l'utilisation de sources actives et contrôlées d'ondes de cisaillement, souvent difficiles à mettre en place. C'est pourquoi cette approche est appelée Elastographie Passive : passive du point de vue de la source des ondes de cisaillement. Les méthodes de tomographie passive sont largement développées dans le domaine de la sismologie et la géophysique, où l'implémentation des sources d'ondes contrôlées est très difficile.

L'approche élastographie passive a été introduite par Thomas Gallot au cours de sa thèse à l'Institut des Sciences de la Terre (ISTerre), à Grenoble. Son objectif était d'utiliser les méthodes de corrélation de bruit développées en sismologie pour réaliser des cartes d'élasticité dans le corps humain.

Un nouveau problème inverse, basé sur la physique du retournement temporel et sur les méthodes de corrélation du bruit, est présenté dans le second chapitre. Cet algorithme combine le retourné temporel du champ de déplacement, du gradient spatial et de sa dérivée temporelle. Une simulation numérique en différences finies dans une cavité élastique bidimensionnelle est présentée afin d'expliquer le principe du champ diffus, ainsi que les méthodes de corrélation du bruit étudiées.

Le troisième chapitre est consacré à l'imagerie avec des imageurs lents. Trois applications sont présentées : dans le pancréas, dans le cerveau et dans la cornée, en utilisant respectivement un échographe standard, un scanner à résonnance magnétique (IRM) et un dispositif de tomographie par cohérence optique (OCT). L'utilisation d'un imageur lent occasionnant une perte d'informations temporelles, il est seulement possible de reconstruire des cartes quantitatives de longueurs d'ondes de cisaillement. Néanmoins, la longueur d'onde locale reste proportionnelle à l'élasticité locale. Dans ce chapitre, il sera démontré que la mesure quantitative des longueurs d'ondes permet la détection d'éventuelles hétérogénéités d'élasticité dans les tissus mous.

Par ailleurs, avec un scanner à cadence ultra-rapide, on dispose des informations temporelles. Ainsi, il est possible de reconstruire des cartes quantitatives des vitesses d'ondes de cisaillement. Cette configuration sera présentée dans le quatrième chapitre. Premièrement, avec un échographe ultra-rapide, des cartes quantitatives de vitesses seront reconstruites dans un gel calibré contenant des inclusions avec des élasticités connues. Ensuite, une tomographie passive de vitesses d'ondes de cisaillement sera réalisée in vivo dans un foie de volontaire sain. Finalement, une étude de faisabilité avec une caméra optique ultra-rapide sera étudiée pour imager les ondes induites à la surface d'un gel mou.

Enfin, une étude de la résolution spatiale de l'élastographie sera présentée dans le cinquième et dernier chapitre de ce manuscrit.

Les résultats présentés dans ce manuscrit répondent en partie aux problématiques de la compréhension et de l'interprétation des ondes élastiques se propageant dans les milieux complexes, à travers l'étude des ondes acoustiques et élastiques. Cette thèse a également été l'opportunité de tester l'élastographie passive dans diverses configurations, à travers deux axes majeurs : les imageurs lents et les imageurs à cadences ultra-rapides.

La tomographie des longueurs d'ondes a été testée dans trois études. Premièrement, des ondes de cisaillement naturellement présentes dans le cerveau d'un volontaire sain ont été observées avec un scanner IRM. Habituellement, une source contrôlée d'ondes de cisaillement est utilisée afin de générer les ondes dans le cerveau. Dans ce cas, la synchronisation entre la source et l'imageur est indispensable pour pouvoir suivre la propagation des ondes et mesurer leurs vitesses. Le dispositif expérimental utilisé en élastographie conventionnelle est souvent très encombrant pour

des applications cliniques. Cependant, dans le cas de l'élastographie passive, le dispositif est considérablement allégé. En contrepartie, seules des cartes de longueurs d'ondes peuvent être reconstruites. Le manque d'études comparatives pour la mesure de l'élasticité du cerveau reste aujourd'hui un des plus grands obstacles de cette étude. Néanmoins, d'autres laboratoires spécialisés en IRM commencent à porter de l'intérêt à cette approche.

Les résultats obtenus avec un système de tomographie par cohérence optique (OCT) dans la cornée d'un rat anesthésié sont très encourageants. Cette approche sans sources d'ondes pourrait être la solution pour amener l'élastographie par tomographie optique en phase d'études cliniques. Il est tout de même indispensable de comprendre plus en détails la propagation d'ondes dans des milieux guidés tels que la cornée. En effet, ces ondes, dites ondes de Lamb, sont connues pour leur forte dispersion, et sont susceptibles de fausser la mesure de l'élasticité locale.

Les Ultrasons Focalisés de Haute Intensité (HIFU) sont la spécialité du laboratoire d'accueil de cette thèse, le LabTAU (Laboratory of Therapeutic Applications of Ultrasound). C'est donc tout naturellement que l'élastographie passive a été testée pour le monitoring du traitement par HIFU des tissus biologiques. Les résultats très encourageants obtenus sur le pancréas du porc sain démontrent un réel intérêt à l'utilisation de l'élastographie passive dans la caractérisation des lésions HIFU. Par ailleurs, il est également prévu d'implémenter l'élastographie passive dans une séquence de traitement par HIFU avec un scanner IRM.

Le Fibroscan® et l'Aixplorer® sont deux échographes ultra-rapides aujourd'hui largement utilisés en routine clinique pour le diagnostic de diverses pathologies cancéreuses. Hors, comme mentionné précédemment, la génération d'ondes de cisaillement est parfois difficile. L'élastographie passive avec un scanner ultra-rapide pourrait être la solution à ce type de problèmes. Son efficacité a été démontrée à travers les résultats obtenus dans un gel calibré et dans le foie d'un volontaire sain.

La résolution de l'élastographie passive a été évaluée via une étude expérimentale. Les résultats montrent que la résolution des images obtenues par une méthode d'élastographie par ondes de cisaillement en général - et plus spécifiquement par élastographie passive - n'est pas limitée par la longueur d'ondes de cisaillement. Celle-ci est du même ordre de grandeur que la résolution des images ultrasonores.

Pour finir ce manuscrit, il convient de préciser que, bien que les objectifs fixés au début de cette thèse incluaient également la caractérisation des tissus biologiques par la mesure de leurs viscosité, anisotropie et non-linéarité, il a plutôt été choisi de saisir les opportunités qui se sont présentées, pour tester l'élastographie passive dans des applications précliniques diverses. Il est néanmoins important de garder en tête que les paramètres viscoélastiques pourraient constituer des outils supplémentaires pour un diagnostic complet.

7 Bibliographic references

Abbe, E. (1873). Beiträge zur Theorie des Mikroskops und der mikroskopischen Wahrnehmung. Arch. Für Mikrosk. Anat. *9*, 413–418.

Alam, S.K., Ophir, J., and Varghese, T. (2000). Elastographic axial resolution criteria: An experimental study. IEEE Trans. Ultrason. Ferroelectr. Freq. Control *47*, 304–309.

Arani, A., Murphy, M.C., Glaser, K.J., Manduca, A., Lake, D.S., Kruse, S.A., Jack, C.R., Ehman, R.L., and Huston, J. (2015). Measuring the effects of aging and sex on regional brain stiffness with MR elastography in healthy older adults. Neuroimage *111*, 59–64.

Arnal, B., Pernot, M., and Tanter, M. (2011). Monitoring of thermal therapy based on shear modulus changes: I. shear wave thermometry. IEEE Trans. Ultrason. Ferroelectr. Freq. Control *58*, 369–378.

Barr, R.G., Memo, R., and Schaub, C.R. (2012). Shear wave ultrasound elastography of the prostate: initial results. Ultrasound Q. *28*, 13–20.

Bavu, É., Gennisson, J.-L., Couade, M., Bercoff, J., Mallet, V., Fink, M., Badel, A., Vallet-Pichard, A., Nalpas, B., Tanter, M., et al. (2011). Noninvasive in vivo liver fibrosis evaluation using supersonic shear imaging: a clinical study on 113 hepatitis C virus patients. Ultrasound Med. Biol. *37*, 1361–1373.

Benech, N., and Negreira, C.A. (2010). Monitoring heat-induced changes in soft tissues with 1D transient elastography. Phys. Med. Biol. *55*, 1753.

Benech, N., Brum, J., Catheline, S., Gallot, T., and Negreira, C. (2013). Near-field effects in Green's function retrieval from cross-correlation of elastic fields: Experimental study with application to elastography. J. Acoust. Soc. Am. *133*, 2755–2766.

Bercoff, J., Tanter, M., and Fink, M. (2004a). Supersonic shear imaging: a new technique for soft tissue elasticity mapping. IEEE Trans. Ultrason. Ferroelectr. Freq. Control *51*, 396–409.

Bercoff, J., Tanter, M., and Fink, M. (2004b). Supersonic Shear Imaging : A New Technique for Soft Tissue Elasticity Mapping. IEEE Trans. Ultrason. Ferroelectr. Freq. Control *51*, 396–409.

Betzig, E., and Trautman, J.K. (1992). Near-field optics: microscopy, spectroscopy, and surface modification beyond the diffraction limit. Science *257*, 189–195.

Betzig, E., Patterson, G.H., Sougrat, R., Lindwasser, O.W., Olenych, S., Bonifacino, J.S., Davidson, M.W., Lippincott-Schwartz, J., and Hess, H.F. (2006). Imaging intracellular fluorescent proteins at nanometer resolution. Science *313*, 1642–1645.

Blomgren, P., Papanicolaou, G., and Zhao, H. (2002). Super-resolution in time-reversal acoustics. J. Acoust. Soc. Am. *111*, 230–248.

Boyce, B.L., Grazier, J.M., Jones, R.E., and Nguyen, T.D. (2008). Full-field deformation of bovine cornea under constrained inflation conditions. Biomaterials *29*, 3896–3904.

Buckingham, M.J., Berkhouse, B.V., and Glegg, S.A.L. (1992). 'Passive imaging of targets with ambient noise. Nat. Lond. *365*, 327–329.

Bush, N.L., Rivens, I., ter Haar, G.R., and Bamber, J.C. (1993). Acoustic properties of lesions generated with an ultrasound therapy system. Ultrasound Med. Biol. *19*, 789–801.

Campillo, M., and Paul, A. (2003). Long-range correlations in the diffuse seismic coda. Science *299*, 547–549.

Catheline, S. (1998). Interférométrie-Speckle ultrasonore: Application à la mesure d'élasticité. Université Paris-Diderot-Paris VII.

Catheline, S., Wu, F., and Fink, M. (1999). A solution to diffraction biases in sonoelasticity: The acoustic impulse technique. J. Acoust. Soc. Am. *105*, 2941–2950.

Catheline, S., Benech, N., Brum, J., and Negreira, C. (2008). Time Reversal of Elastic Waves in Soft Solids. Phys. Rev. Lett. *100*, 64301.

Catheline, S., Souchon, R., Rupin, M., Brum, J., Dinh, A.H., and Chapelon, J.-Y. (2013). Tomography from diffuse waves: Passive shear wave imaging using low frame rate scanners. Appl. Phys. Lett. *103*, 14101.

Chatelin, S., Bernal, M., Deffieux, T., Papadacci, C., Flaud, P., Nahas, A., Boccara, C., Gennisson, J.-L., Tanter, M., and Pernot, M. (2014). Anisotropic polyvinyl alcohol hydrogel phantom for shear wave elastography in fibrous biological soft tissue: a multimodality characterization. Phys. Med. Biol. *59*, 6923.

Cohn, N.A., Emelianov, S.Y., and O'Donnell, M. (1997). An elasticity microscope. Part II: Experimental results. IEEE Trans. Ultrason. Ferroelectr. Freq. Control *44*, 1320–1331.

Conti, S.G., Roux, P., and Kuperman, W.A. (2007). Near-field time-reversal amplification. J. Acoust. Soc. Am. *121*, 3602–3606.

Cook, L.T., Zhu, Y., Hall, T.J., and Insana, M.F. (2000). Bioelasticity imaging: II. Spatial resolution. In Medical Imaging 2000, (International Society for Optics and Photonics), pp. 315–324.

Correas, J.-M., Tissier, A.-M., Khairoune, A., Vassiliu, V., Méjean, A., Hélénon, O., Memo, R., and Barr, R.G. (2014). Prostate cancer: diagnostic performance of real-time shear-wave elastography. Radiology *275*, 280–289.

Couade, M., Pernot, M., Prada, C., Messas, E., Emmerich, J., Bruneval, P., Criton, A., Fink, M., and Tanter, M. (2010). Quantitative Assessment of Arterial Wall Biomechanical Properties Using Shear Wave Imaging. Ultrasound Med. Biol. *36*, 1662–1676.

Crouzet, S., Chapelon, J.Y., Rouviere, O., Mege-Lechevallier, F., Colombel, M., Tonoli-Catez, H., Martin, X., and Gelet, A. (2014). Whole-gland ablation of localized prostate cancer with high-intensity focused ultrasound: oncologic outcomes and morbidity in 1002 patients. Eur. Urol. *65*, 907–914.

Deffieux, T. (2008). Palpation par force de radiation ultrasonore et échographie ultrarapide: Applications à la caractérisation tissulaire in vivo. Université Paris-Diderot-Paris VII.

Derode, A., Tourin, A., de Rosny, J., Tanter, M., Yon, S., and Fink, M. (2003a). Taking Advantage of Multiple Scattering to Communicate with Time-Reversal Antennas. Phys. Rev. Lett. *90*, 14301.

Derode, A., Larose, E., Tanter, M., De Rosny, J., Tourin, A., Campillo, M., and Fink, M. (2003b). Recovering the Green's function from field-field correlations in an open scattering medium (L). J. Acoust. Soc. Am. *113*, 2973–2976.

Derode, A., Larose, E., Campillo, M., and Fink, M. (2003c). How to estimate the Green's function of a heterogeneous medium between two passive sensors? Application to acoustic waves. Appl. Phys. Lett. *83*, 3054–3056.

Dickinson, R.J., and Hill, C.R. (1982). Measurement of soft tissue motion using correlation between A-scans. Ultrasound Med. Biol. *8*, 263–271.

Draeger, C., and Fink, M. (1997). One-Channel Time Reversal of Elastic Waves in a Chaotic 2D-Silicon Cavity. Phys. Rev. Lett. *79*, 407–410.

Duvall Jr, T.L., Jefferies, S.M., Harvey, J.W., and Pomerantz, M.A. (1993). Time-distance helioseismology. Nature *362*, 430–432.

Eisensher, A., Schweg-Toffler, E., Pelletier, G., and Jacquemard, P. (1983). La palpation échographique rythmée : Echosismographie. Une nouvelle technique de différenciation des tumeurs bénignes et malignes par l'étude ultrasonore de l'élasticité tissulaire. J Radiol *64*, 255–261.

Emelianov, S.Y., Aglyamov, S.R., Shah, J., Sethuraman, S., Scott, W.G., Schmitt, R., Motamedi, M., Karpiouk, A., and Oraevsky, A.A. (2004). Combined ultrasound, optoacoustic, and elasticity imaging. In Biomedical Optics 2004, (International Society for Optics and Photonics), pp. 101–112.

Errico, C., Pierre, J., Pezet, S., Desailly, Y., Lenkei, Z., Couture, O., and Tanter, M. (2015). Ultrafast ultrasound localization microscopy for deep super-resolution vascular imaging. Nature *527*, 499–502.

Ferraioli, G., Filice, C., Castera, L., Choi, B.I., Sporea, I., Wilson, S.R., Cosgrove, D., Dietrich, C.F., Amy, D., Bamber, J.C., et al. (2015). WFUMB guidelines and recommendations for clinical use of ultrasound elastography: Part 3: liver. Ultrasound Med. Biol. *41*, 1161–1179.

Fink, M. (1997). Time Reversed Acoustics. Phys. Today *50*, 34–40.

Gallot, T. (2010). Imagerie acoustique en milieux reverberants. Université de Grenoble.

Gallot, T., Catheline, S., Roux, P., Brum, J., Benech, N., and Negreira, C. (2011). Passive elastography: shear-wave tomography from physiological-noise correlation in soft tissues. IEEE Trans. Ultrason. Ferroelectr. Freq. Control *58*, 1122–1126.

Gallot, T., Catheline, S., Roux, P., and Campillo, M. (2012). A passive inverse filter for Green's function retrieval. J. Acoust. Soc. Am. *131*, EL21–EL27.

Giles, P.M., Duvall, T.L., Scherrer, P.H., and Bogart, R.S. (1997). A subsurface flow of material from the Sun's equator to its poles. Nature *390*, 52–54.

Gouédard, P., Stehly, L., Brenguier, F., Campillo, M., Colin de Verdière, Y., Larose, E., Margerin, L., Roux, P., Sánchez-Sesma, F.J., Shapiro, N.M., et al. (2008). Cross-correlation of random fields: mathematical approach and applications. Geophys. Prospect. *56*, 375–393.

Hell, S.W., and Wichmann, J. (1994). Breaking the diffraction resolution limit by stimulated emission: stimulated-emission-depletion fluorescence microscopy. Opt. Lett. *19*, 780–782.

Huang, S.-R., Lerner, R.M., and Parker, K.J. (1992). Time domain Doppler estimators of the amplitude of vibrating targets. J. Acoust. Soc. Am. *91*, 965–974.

Huwart, L., Peeters, F., Sinkus, R., Annet, L., Salameh, N., ter Beek, L.C., Horsmans, Y., and Van Beers, B.E. (2006). Liver fibrosis: non-invasive assessment with MR elastography. NMR Biomed. *19*, 173–179.

Ing, R.K., Quieffin, N., Catheline, S., and Fink, M. (2005). In solid localization of finger impacts using acoustic time-reversal process. Appl. Phys. Lett. *87*, 204104.

Kanai, H., Sato, M., Koiwa, Y., and Chubachi, N. (1996). Transcutaneous measurement and spectrum analysis of heart wall vibrations. IEEE Trans. Ultrason. Ferroelectr. Freq. Control *43*, 791–810.

Kinsey, A.M., Diederich, C.J., Rieke, V., Nau, W.H., Pauly, K.B., Bouley, D., and Sommer, G. (2008). Transurethral ultrasound applicators with dynamic multi-sector control for prostate thermal therapy: In vivo evaluation under MR guidance. Med. Phys. *35*, 2081–2093.

Konofagou, E.E., D'hooge, J., and Ophir, J. (2002). Myocardial elastography—A feasibility study in vivo. Ultrasound Med. Biol. *28*, 475–482.

Krouskop, T.A., Dougherty, D.R., Vinson, F.S., and others (1987). A pulsed Doppler ultrasonic system for making noninvasive measurements of the mechanical properties of soft tissue. J Rehabil Res Dev *24*, 1–8.

Kruse, S.A., Rose, G.H., Glaser, K.J., Manduca, A., Felmlee, J.P., Jack, C.R., and Ehman, R.L. (2008). Magnetic resonance elastography of the brain. Neuroimage *39*, 231–237.

Kuperman, W.A., Hodgkiss, W.S., Song, H.C., Akal, T., Ferla, C., and Jackson, D.R. (1998). Phase conjugation in the ocean: Experimental demonstration of an acoustic time-reversal mirror. J. Acoust. Soc. Am. *103*, 25–40.

Larose, E., Margerin, L., Derode, A., van Tiggelen, B., Campillo, M., Shapiro, N., Paul, A., Stehly, L., and Tanter, M. (2006). Correlation of random wavefields: An interdisciplinary review. GEOPHYSICS *71*, SI11-SI21.

Lerner, R.M., Parker, K.J., Holen, J., Gramiak, R., and Waag, R.C. (1988). Sono-elasticity: medical elasticity images derived from ultrasound signals in mechanically vibrated targets. In Acoustical Imaging, (Springer), pp. 317–327.

Lerosey, G., De Rosny, J., Tourin, A., and Fink, M. (2007). Focusing beyond the diffraction limit with far-field time reversal. Science *315*, 1120–1122.

Levinson, S.F., Shinagawa, M., and Sato, T. (1995). Sonoelastic determination of human skeletal muscle elasticity. J. Biomech. *28*, 1145–1154.

Li, C., Guan, G., Zhang, F., Nabi, G., Wang, R.K., and Huang, Z. (2014). Laser induced surface acoustic wave combined with phase sensitive optical coherence tomography for superficial tissue characterization: a solution for practical application. Biomed. Opt. Express *5*, 1403.

Manduca, A., Oliphant, T.E., Dresner, M.A., Mahowald, J.L., Kruse, S.A., Amromin, E., Felmlee, J.P., Greenleaf, J.F., and Ehman, R.L. (2001). Magnetic resonance elastography: non-invasive mapping of tissue elasticity. Med. Image Anal. *5*, 237–254.

McGarry, M.D.J., Johnson, C.L., Sutton, B.P., Georgiadis, J.G., Van Houten, E.E.W., Pattison, A.J., Weaver, J.B., and Paulsen, K.D. (2015). Suitability of poroelastic and viscoelastic mechanical models for high and low frequency MR elastography. Med. Phys. *42*, 947–957.

Melodelima, D., Prat, F., Fritsch, J., Theillere, Y., and Cathignol, D. (2008). Treatment of esophageal tumors using high intensity intraluminal ultrasound: first clinical results. J Transl Med *6*, b59.

Muller, M., Gennisson, J.-L., Deffieux, T., Tanter, M., and Fink, M. (2009). Quantitative viscoelasticity mapping of human liver using supersonic shear imaging: preliminary in vivo feasability study. Ultrasound Med. Biol. *35*, 219–229.

Muthupillai, R., Lomas, D.J., Rossman, P.J., Greenleaf, J.F., and others (1995). Magnetic resonance elastography by direct visualization of propagating acoustic strain waves. Science *269*, 1854.

Nguyen, T., Couade, M., Bercoff, J., and Tanter, M. (2011). Assessment of viscous and elastic properties of sub-wavelength layered soft tissues using shear wave spectroscopy: Theoretical framework and in vitro experimental validation. IEEE Trans. Ultrason. Ferroelectr. Freq. Control *58*, 2305–2315.

Nguyen, T., Arnal, B., Song, S., Huang, Z., Wang, R.K., and O'Donnell, M. (2015). Shear wave elastography using amplitude-modulated acoustic radiation force and phase-sensitive optical coherence tomography. J. Biomed. Opt. *20*, 16001.

Nguyen, T.-M., Song, S., Arnal, B., Huang, Z., O'Donnell, M., and Wang, R.K. (2014a). Visualizing ultrasonically induced shear wave propagation using phase-sensitive optical coherence tomography for dynamic elastography. Opt. Lett. *39*, 838–841.

Nguyen, T.-M., Song, S., Arnal, B., Wong, E.Y., Huang, Z., Wang, R.K., and O'Donnell, M. (2014b). Shear wave pulse compression for dynamic elastography using phase-sensitive optical coherence tomography. J. Biomed. Opt. *19*, 016013/1-6.

Nightingale, K., Soo, M.S., Nightingale, R., and Trahey, G. (2002a). Acoustic radiation force impulse imaging: in vivo demonstration of clinical feasibility. Ultrasound Med. Biol. *28*, 227–235.

Nightingale, K., Soo, M.S., Nightingale, R., and Trahey, G. (2002b). Acoustic radiation force impulse imaging: in vivo demonstration of clinical feasibility. Ultrasound Med. Biol. *28*, 227–235.

Nock, L., Trahey, G.E., and Smith, S.W. (1989). Phase aberration correction in medical ultrasound using speckle brightness as a quality factor. J. Acoust. Soc. Am. *85*, 1819–1833.

Nordez, A., Gennisson, J.L., Casari, P., Catheline, S., and Cornu, C. (2008). Characterization of muscle belly elastic properties during passive stretching using transient elastography. J. Biomech. *41*, 2305–2311.

Ophir, J., Cespedes, I., Ponnekanti, H., Yazdi, Y., and Li, X. (1991). Elastography: a quantitative method for imaging the elasticity of biological tissues. Ultrason. Imaging *13*, 111–134.

Parker, K.J., and Lerner, R.M. (1992). Sonoelasticity of organs: shear waves ring a bell. J. Ultrasound Med. *11*, 387–392.

Paul, A., Campillo, M., Margerin, L., Larose, E., and Derode, A. (2005). Empirical synthesis of time-asymmetrical Green functions from the correlation of coda waves. J. Geophys. Res. Solid Earth *110*, B08302.

Pernot, M., Montaldo, G., Tanter, M., and Fink, M. (2006). "Ultrasonic stars" for time-reversal focusing using induced cavitation bubbles. Appl. Phys. Lett. *88*, 34102.

Plewes, D.B., Betty, I., Urchuk, S.N., and Soutar, I. (1995). Visualizing tissue compliance with MR imaging. J. Magn. Reson. Imaging *5*, 733–738.

Poissonnier, L., Chapelon, J.-Y., Rouviere, O., Curiel, L., Bouvier, R., Martin, X., Dubernard, J.M., and Gelet, A. (2007). Control of prostate cancer by transrectal HIFU in 227 patients. Eur. Urol. *51*, 381–387.

Rayleigh, Lord (1896). XV. On the theory of optical images, with special reference to the microscope. Lond. Edinb. Dublin Philos. Mag. J. Sci. *42*, 167–195.

Razani, M., Mariampillai, A., Sun, C., Luk, T.W.H., Yang, V.X.D., and Kolios, M.C. (2012a). Feasibility of optical coherence elastography measurements of shear wave propagation in homogeneous tissue equivalent phantoms. Biomed. Opt. Express *3*, 972–980.

Razani, M., Mariampillai, A., Sun, C., Luk, T.W., Yang, V.X., and Kolios, M.C. (2012b). Feasibility of optical coherence elastography measurements of shear wave propagation in homogeneous tissue equivalent phantoms. Biomed. Opt. Express *3*, 972–980.

Righetti, R., Ophir, J., and Ktonas, P. (2002). Axial resolution in elastography. Ultrasound Med. Biol. *28*, 101–113.

de Rosny, J., and Fink, M. (2002). Overcoming the diffraction limit in wave physics using a time-reversal mirror and a novel acoustic sink. Phys. Rev. Lett. *89*, 124301.

de Rosny, J., and Fink, M. (2007). Focusing properties of near-field time reversal. Phys. Rev. A *76*, 65801.

Roux, P., Kuperman, W.A., and Group, the N. (2004). Extracting coherent wave fronts from acoustic ambient noise in the ocean. J. Acoust. Soc. Am. *116*, 1995–2003.

Roux, P., Sabra, K.G., Kuperman, W.A., and Roux, A. (2005). Ambient noise cross correlation in free space: Theoretical approach. J. Acoust. Soc. Am. *117*, 79–84.

Royer, D., and Dieulesaint, E. (2000). Elastic Waves in Solids I : Free and Guided Propagation.

Sabra, K.G., Conti, S., Roux, P., and Kuperman, W.A. (2007). Passive in vivo elastography from skeletal muscle noise. Appl. Phys. Lett. *90*, 194101.

Sack, I., Beierbach, B., Hamhaber, U., Klatt, D., and Braun, J. (2008). Non-invasive measurement of brain viscoelasticity using magnetic resonance elastography. NMR Biomed. *21*, 265–271.

Sandrin, L., Catheline, S., Tanter, M., Hennequin, X., and Fink, M. (1999). Time-resolved pulsed elastography with ultrafast ultrasonic imaging. Ultrason. Imaging *21*, 259–272.

Sandrin, L., Tanter, M., Gennisson, J.L., Catheline, S., and Fink, M. (2002). Shear elasticity probe for soft tissues with 1-D transient elastography. IEEE Trans. Ultrason. Ferroelectr. Freq. Control *49*, 436–446.

Sandrin, L., Fourquet, B., Hasquenoph, J.-M., Yon, S., Fournier, C., Mal, F., Christidis, C., Ziol, M., Poulet, B., Kazemi, F., et al. (2003). Transient elastography: a new noninvasive method for assessment of hepatic fibrosis. Ultrasound Med. Biol. *29*, 1705–1713.

Sarvazyan, A.P., Rudenko, O.V., Swanson, S.D., Fowlkes, J.B., and Emelianov, S.Y. (1998a). Shear wave elasticity imaging: a new ultrasonic technology of medical diagnostics. Ultrasound Med. Biol. *24*, 1419–1435.

Sarvazyan, A.P., Rudenko, O. V., Swanson, S.D., Fowlkes, J.B., and Emelianov, S.Y. (1998b). Shear Wave Elasticity Imaging: A New Ultrasonic Technology of Medical Diagnosis. Ultrasound Med. Biol. *24*, 1419–1435.

Shapiro, N.M., Campillo, M., Stehly, L., and Ritzwoller, M.H. (2005). High-resolution surface-wave tomography from ambient seismic noise. Science *307*, 1615–1618.

Shi, X., Martin, R.W., Rouseff, D., Vaezy, S., and Crum, L.A. (1999). Detection of High-Intensity Focused Ultrasound Liver Lesions Using Dynamic Elastometry. Ultrason. Imaging *21*, 107–126.

Sinkus, R., Tanter, M., Catheline, S., Lorenzen, J., Kuhl, C., Sondermann, E., and Fink, M. (2005). Imaging anisotropic and viscous properties of breast tissue by magnetic resonance-elastography. Magn. Reson. Med. *53*, 372–387.

Snieder, R., Wapenaar, K., and Wegler, U. (2007). Unified Green's function retrieval by cross-correlation; connection with energy principles. Phys. Rev. E *75*, 36103.

Song, S., Huang, Z., Nguyen, T.M., Wong, E.Y., Arnal, B., O'Donnell, M., and Wang, R.K. (2013). Shear modulus imaging by direct visualization of propagating shear waves with phase-sensitive optical coherence tomography. J. Biomed. Opt. *18*, 121509/1-7.

Song, S., Wei, W., Hsieh, B., Pelivanov, I., Shen, T.T., Donnell, M.O., Ruikang, K., Song, S., Wei, W., Hsieh, B., et al. (2016). Strategies to improve phase-stability of ultrafast swept source optical coherence tomography for single shot imaging of transient mechanical waves at 16 kHz frame rate Strategies to improve phase-stability of ultrafast swept source optical coherence tomography for single shot imaging of transient mechanical waves at 16 kHz frame rate. *191104*.

Souchon, R., Rouvière, O., Gelet, A., Detti, V., Srinivasan, S., Ophir, J., and Chapelon, J.Y. (2003). Visualisation of HIFU lesions using elastography of the human prostate in vivo: preliminary results. Ultrasound Med. Biol. *29*, 1007–1015.

Souchon, R., Salomir, R., Beuf, O., Milot, L., Grenier, D., Lyonnet, D., Chapelon, J.-Y., and Rouvière, O. (2008). Transient MR elastography (t-MRE) using ultrasound radiation force: Theory, safety, and initial experiments in vitro. Magn. Reson. Med. *60*, 871–881.

Sugimoto, T., Ueha, S., and Itoh, K. (1990). Tissue hardness measurement using the radiation force of focused ultrasound. In Ultrasonics Symposium, 1990. Proceedings., IEEE 1990, (IEEE), pp. 1377–1380.

Sutton, M.A., Orteu, J.J., and Schreier, H. (2009). Image correlation for shape, motion and deformation measurements: basic concepts, theory and applications (Springer Science & Business Media).

Thomas, J.-L., Wu, F., and Fink, M. (1996). Time Reversal Focusing Applied to Lithotripsy. Ultrason. Imaging *18*, 106–121.

Thompson, L.A., and Gardner, C.S. (1987). Experiments on laser guide stars at Mauna Kea Observatory for adaptive imaging in astronomy. Nature *328*, 229–231.

Uchida, T., Nakano, M., Hongo, S., Shoji, S., Nagata, Y., Satoh, T., Baba, S., Usui, Y., and Terachi, T. (2012). High-intensity focused ultrasound therapy for prostate cancer. Int. J. Urol. *19*, 187–201.

Ulrich, T.J., Johnson, P.A., and Guyer, R.A. (2007). Interaction dynamics of elastic waves with a complex nonlinear scatterer through the use of a time reversal mirror. Phys. Rev. Lett. *98*, 104301.

Vincenot, J., Kocot, A., Vignot, A., Chavrier, F., Blanc, E., Dupré, A., Rivoire, M., Chapelon, J.Y., and Melodelima, D. (2016). Toroidal Transducer for Intraoperative Thermal Ablation of Pancreatic Tumours by High-Intensity Focused Ultrasound. First In Vitro Experiments. IRBM *37*, 152–157.

Wagshul, M.E., Eide, P.K., and Madsen, J.R. (2011). The pulsating brain: a review of experimental and clinical studies of intracranial pulsatility. Fluids Barriers CNS *8*, 1.

Wang, S., and Larin, K. V (2014). Shear wave imaging optical coherence tomography (SWI-OCT) for ocular tissue biomechanics. Opt. Lett. *39*, 1–4.

Wang, R.K., Ma, Z., and Kirkpatrick, S.J. (2006). Tissue Doppler optical coherence elastography for real time strain rate and strain mapping of soft tissue. Appl. Phys. Lett. *89*, 144103/1-3.

Wang, R.K., Kirkpatrick, S., and Hinds, M. (2007). Phase-sensitive optical coherence elastography for mapping tissue microstrains in real time. Appl. Phys. Lett. *90*, 164105/1-3.

Wang, S., Li, J., Manapuram, R.K., Menodiado, F.M., Ingram, D.R., Twa, M.D., Lazar, A.J., Lev, D.C., Pollock, R.E., and Larin, K. V (2012a). Noncontact measurement of elasticity for the detection of soft-tissue tumors using phase-sensitive optical coherence tomography combined with a focused air-puff system. Opt. Lett. *37*, 5184–5186.

Wang, S., Li, J., Manapuram, R.K., Menodiado, F.M., Ingram, D.R., Twa, M.D., Lazar, A.J., Lev, D.C., Pollock, R.E., and Larin, K.V. (2012b). Noncontact measurement of elasticity for the detection of soft-tissue tumors using phase-sensitive optical coherence tomography combined with a focused air-puff system. Opt. Lett. *37*, 5184–5186.

Weaver, R.L. (1982). On diffuse waves in solid media. J. Acoust. Soc. Am. *71*, 1608–1609.

Weaver, R., and Lobkis, O. (2002). On the emergence of the Green's function in the correlations of a diffuse field: pulse-echo using thermal phonons. Ultrasonics *40*, 435–439.

Weaver, R.L., and Lobkis, O.I. (2001). Ultrasonics without a source: Thermal fluctuation correlations at MHz frequencies. Phys. Rev. Lett. *87*, 134301.

Weaver, J.B., Pattison, A.J., McGarry, M.D., Perreard, I.M., Swienckowski, J.G., Eskey, C.J., Lollis, S.S., and Paulsen, K.D. (2012). Brain mechanical property measurement using MRE with intrinsic activation. Phys. Med. Biol. *57*, 7275.

Woo, H., Lee, J.Y., Yoon, J.H., Kim, W., Cho, B., and Choi, B.I. (2015). Comparison of the reliability of acoustic radiation force impulse imaging and supersonic shear imaging in measurement of liver stiffness. Radiology *277*, 881–886.

Wu, F., Wang, Z.-B., Cao, Y.-D., Zhu, X.-Q., Zhu, H., Chen, W.-Z., and Zou, J.-Z. (2007). "Wide local ablation" of localized breast cancer using high intensity focused ultrasound. J. Surg. Oncol. *96*, 130–136.

Wu, T., Felmlee, J.P., Greenleaf, J.F., Riederer, S.J., and Ehman, R.L. (2001). Assessment of thermal tissue ablation with MR elastography. Magn. Reson. Med. *45*, 80–87.

Yamakoshi, Y., Sato, J., and Sato, T. (1990). Ultrasonic imaging of internal vibration of soft tissue under forced vibration. IEEE Trans. Ultrason. Ferroelectr. Freq. Control *37*, 45–53.

Résumé : *Les travaux menés lors de cette thèse portent sur le développement d'une approche passive d'elastographie, l'imagerie de l'élasticité des tissus mous. Inspirée des techniques de corrélation de bruits sismiques développées en sismologie, et du retournement temporel en acoustique. L'elastographie passive utilise des ondes de cisaillement naturellement présentent dans le corps humain pour extraire les propriétés mécaniques des tissues biologiques. La faisabilité de cette approche passive est démontrée dans divers applications. En ultrason, des d'échographes à cadence lente ont été utilisés pour le guidage du traitement par ultrason à haut intensité dans une étude préclinique. Puis l'utilisation d'un échographe ultra-rapide pour la reconstruction des cartes de vitesses dans des gels calibrés ainsi que in-vivo. L'elastographie passive par résonnance magnétique a été également mise en place pour imager les mouvements naturels dans le cerveau d'un volontaire sain et la réalisation d'une tomographie de longueurs d'ondes. En optique, pour des applications en ophtalmologie ou en dermatologie, la faisabilité de l'elastographie passive par cohérence optique a été démontrée dans un gel puis in-vivo dans l'œil d'une souris. Puis une preuve du concept d'un dispositif d'imagerie d'ondes de surfaces complètement optique été testé dans des gels plan, courbé, isotrope ou anisotrope. Finalement, la limite de la résolution de l'Elastographie passive par ultrason est évaluée.*

Summary: *The aim of this thesis was the development of a new approach called passive elastography. This approach is inspired from noise correlation methods well developed in seismology and time reversal technics in acoustics. Passive elastography uses shear waves naturally induced in the human body to extract the mechanical properties of soft tissue. The feasibility of this method was tested in several applications. First in ultrasound, slow frame rate ultrasound scanner was used to monitor high intensity focused ultrasound treatment on porcine pancreas. Then, an ultrafast ultrasound scanner was used to retrieve shear wave speed map in a calibrated phantom and in-vivo. Second, Magnetic resonance elastography was implemented to image natural motion in the brain of healthy volunteers and conduct shear wavelength tomography. Third, for ophthalmological and dermatological applications, optical coherence passive elastography was tested in a phantom and a cornea of healthy mouse. Also, a fully optical setup was established to image surface wave for elastography applications. Finally, the resolution limit of elastography was measured using an ultrasound ultrafast scanner.*